Optical detection of magneto-acoustic dynamics

Piotr Kuszewski

Sorbonne Université

École doctorale 397: Physique et Chimie des Matériaux

Thèse de DOCTORAT

Spécialité Physique

présentée par

Piotr Kuszewski

Pour obtenir le grade de Docteur de: Sorbonne Université

Sujet de la thèse

Optical detection of magneto-acoustic dynamics

soutenue le 9 Novembre 2018

Devant le jury composé de:

Rapporteur	Olivier Klein	CEA
Rapporteur	Thomas Pezeril	Université du Maine
Examinatrice	Sarah Benchabane Gaiffe	FEMTO-ST
Examinatrice	Karine Dumesnil	Institut Jean Lamour
Examinatrice	Massimiliano Marangolo	Institut des NanoSciences de Paris
Directrice de thèse	Catherine Gourdon	Institut des NanoSciences de Paris
Co-directrice de thèse	Laura Thevenard	Institut des NanoSciences de Paris

Acknowledgments

First, I want to thank my supervisors Catherine Gourdon and Laura Thevenard for their support, guidance, patience and door always open for a discussion.

I owe my deepest gratitude to many collaborators without whom this work would have been impossible, I would like to highly acknowledge Jean-Yves Duquesne and Laurent Belliard who helped me understand the physics and experimentally excite acoustic waves. I benefited a lot from our collaboration. I also would like to thank all my laboratory colleagues and personnel at INSP for sharing their knowledge and experience with me.

Finally, I want to thank my mom and dad for unfailing support and encouragement throughout my life. I would like to thank my whole family: my brother Paweł and his wife with their newly born child Jan, my aunt and uncle. I must also acknowledge Karolina for being with me for the whole time, with her everything has been much easier.

Abstract

In the developing field of spin wave-based information technology, this work investigates the possibility to use surface acoustic waves (SAW) to excite spin-waves in ferromagnetic thin layers relying on the magnetoelastic coupling. This would provide a non-inductive, efficient, and remote addressing of spin waves.

In the first project we develop an experimental setup to generate electrically excited SAWs phase-locked to probe laser pulses. The magnetization dynamics is detected by an optical bridge using magneto-optical effects (Kerr and Voigt). We investigate the resonant magneto-elastic coupling in a thin film of the ferromagnetic semiconductor (Ga,Mn)As. To reach resonant coupling, the spin-wave frequency is scanned across the SAW frequency using a magnetic field. We disentangle the photoelastic contribution from the magneto-optical one, from which we obtain the amplitude of magnetization precession. We show that it is driven solely by the acoustic wave. Its field dependence is shown to agree well with theoretical calculations. Its amplitude resonates at the same field as the resonant attenuation of the acoustic wave, clearly evidencing the magnetoacoustic resonance with high sensitivity. The influence of temperature, SAW frequency and power on the coupling efficiency are studied.

In the second project we use SAWs thermoelastically excited by a tightly focused laser beam on ferromagnetic metals (Ni, FeGa, Co) on a transparent substrate (glass, sapphire). Spatio-temporal maps of the surface displacement and magneto-optical signal are obtained. A high-frequency shift of the frequency spectrum of the latter gives a hint for spin-wave excitation by SAWs.

Résumé

Ce travail se situe dans le contexte de l'utilisation des ondes de spin comme vecteur d'information. Il explore la possibilité d'exciter l'aimantation dans de fines couches ferromagnétiques grâce au couplage magnéto-élastique. Cela permettrait un adressage non-inductif, efficace, et distant des ondes de spin.

Dans un premier volet, nous avons développé un dispositif expérimental générant des ondes acoustiques de surface (ODS) électriquement, verrouillées en phase à des impulsions de laser sonde. La dynamique d'aimantation est détectée grâce aux effets magnéto-optiques (Kerr et Voigt). Nous étudions le couplage magnétoélastique résonant dans une couche mince du semiconducteur magnétique (Ga,Mn)As. Afin d'atteindre la résonance, la fréquence des ondes de spin est ajustée à celle des ODS par un champ magnétique. Nous isolons les contributions photo-élastique et magnéto-optique du signal, pour quantifier l'amplitude de la précession d'aimantation. Nous montrons que la précession observée est exclusivement déclenchée par l'ODS. La variation en champ de son amplitude correspond très bien à celle calculée, et elle est maximum au champ pour laquelle l'absorption de l'ODS est maximale, démontrant clairement la résonance magnétoacoustique. L'influence de la fréquence et de la puissance de l'ODS, ainsi que de la température sur l'efficacité du couplage est également explorée.

Dans un deuxième volet, nous avons excité des ODS par effet thermoélastique grâce à un faisceau laser focalisé, et cela sur des couches magnétiques métalliques cette fois-ci (Ni, FeGa, Co), déposées sur un substrat transparent (verre, sapphire). Des cartes spatio-temporelles du déplacement de la surface et du signal magnéto-optique ont été obtenues. Un décalage du spectre magnéto-optique vers les hautes fréquences semble indiquer une excitation des ondes de spin par les ODS.

Contents

Introduction

The first commercially available computer with a magnetic hard drive disk was the IBM 305 RAMAC (Random Access Memory Accounting) developed in 1956 [1]. Its size was extremely large, only the disk storage unit covered the space equivalent to one taken by three refrigerators (Fig. 0.1 (a)). The monthly cost of the data storage was $ 3 200 which is over $ 28 000 nowadays and $ 7 500 per MB. Nevertheless, over 1000 of these computers were built in 4 years, because of their high capacity, 3.75 MB (5 million alphanumeric characters), and a fast access time to any bit (average 0.6 s). This changed once and for all the perception of magnetism as a technologically attractive solution for data computing.

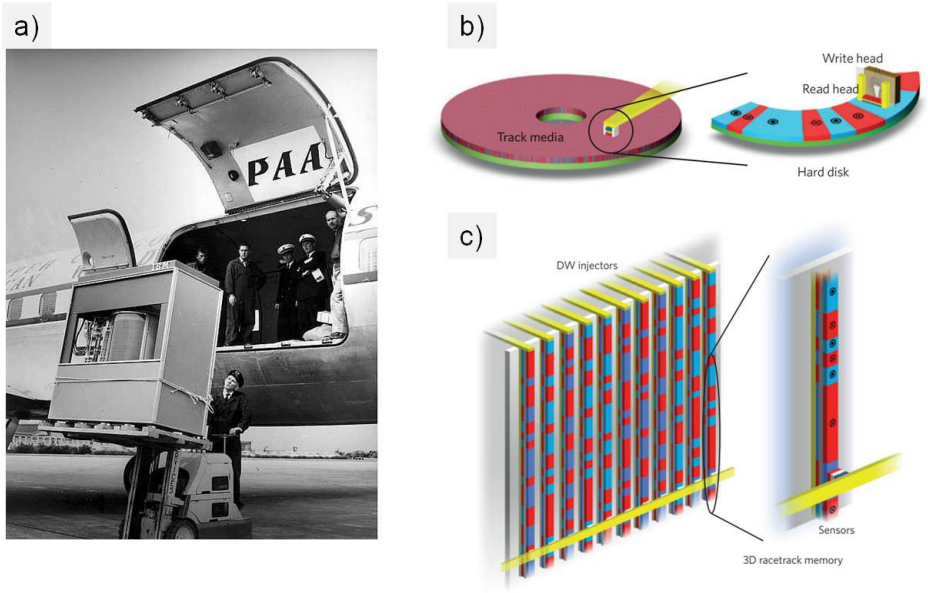

Figure 0.1.: (a) Picture of the IBM 350 data storage unit taken at the Amsterdam Schiphol airport in 1957 [2]. In this model, data was saved on one of 50 spinning Aluminium discs coated with Iron oxide. (b) The general concept of the HDD: the recording head is used to write and read the bits in a thin ferromagnetic film. It is mounted on a movable arm which moves across the rotating disc. The red and blue colors indicate opposite directions of magnetization. (c) The racetrack memory concept proposed in 2008 by Stuart Parkin [3].

The magnetic recording revolution has been lasting for the last 60 years and allowed us to forget for instance about punched cards. The capacity of a magnetic hard

disk drive (HDD) reached above 10 TB in 2018 with an areal density of around 1.4 Tbit/in^2. However, this is a 2D technology which is very close to the physical limit, therefore to increase the storage density, the world demands new solutions. One of the concepts of the 3D data storage is the racetrack memory, where the data will be saved in domains separated by domain walls in thin magnetic wires arranged in a high density array (Fig. 0.10.1 (c)) [3]. The domain walls could be moved along the wire with a spin polarized current to shift the bits (magnetic domains) to read and write sections. This device will not require any mechanically movable parts. Thus, the read and write time can be lowered by million times compared to the standard HDD discs. Of course, magnetism is not only used for data storage but also in data transport [4, 5], logic gates[6] and in the widest sense, in signal processing[7] including non-boolean, wave-based computing [8, 9] (Fig. 0.2). Magnetization dynamics, can be described in terms of spin waves, where the spin excitations can propagate in a coherent way. The quanta of magnetization dynamics are called magnons in analogy with phonons or photons. Similarly to photonics, magnonics aim to design new architectures to built new functionalities using magnons.

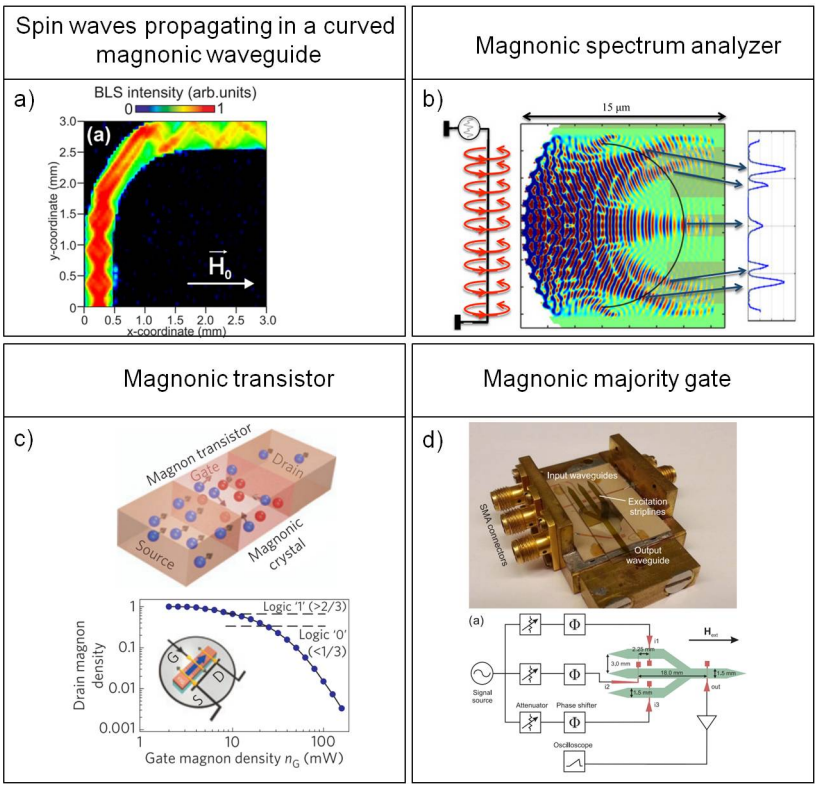

Figure 0.2.: A few chosen experiments that illustrate the possible usage of magnonics in signal processing. (a) Image of a spin wave intensity propagating in a geometrically curved YIG waveguide [5]. (b) One example of a non boolean signal device: schematics of the spin wave based spectrum analyzer. Spin waves are excited with the antenna and then they are diffracted on a curved diffraction grating. If the spin waves are generated with a current carring multiple frequencies, the diffrent wavelengths will be focused at different places on the right side [10]. (c) Scheme of the magnonic transistor, based on a magnonic crystal. The magnons injected in the source propagate to the drain in the case when there is no gate-magnons. Gate-magnons are at the frequency of the magnonic crystal bandgap, thus they do not propagate to the drain. Therefore, the high density of the gate-magnons scatters nonlinearly the source magnons and lowers the ones transmitted to the drain [11]. (d) Picture of the magnonic majority gate realized in 2017 [12]. The spin waves injected to the three inputs interfere with each other and the information is decoded at the output from the phase of the signal.

Indeed, magnonics and photonics are often linked and where they come together it makes the project far-reaching. The power of magnonics lies in its elemental properties, such as the μm-nm spin wave wavelength (GHz-THz frequency regime) and the absence of Joule heating: in magnon transport there is no charge transfer, only angular momentum transfer. Moreover, magnon properties can be tuned in a variety of ways e.g. by changing the magnetic material and its geometry, temperature, mag-

netic field and direction of the field [8]. So far, the most common excitation of spin waves was an inductive antenna. This is a solution, that is easy to implement and which can be also used to detect the spin waves. However, antenna excitation is the weakest point of spin wave-based computing systems due to its low energy efficiency and limitation to long wavelengths because of the impedance mismatch (the width of the antenna needs to be smaller than the spin wave wavelength) [9]. Moreover in most ferromagnetic materials spin waves are damped over short distances (tens of µm). Some of these limitations can be overcome by using magneto-elastic coupling. This field has witnessed a renewed interest in recent years with the extensive work of a few groups that brought very promising achievements *e.g.* acoustically driven ferromagnetic resonance [13, 14] and switching [15, 16] or acoustically assisted, efficient domain wall motion for the above-mentioned racetrack memories [17, 18]. It is expected that magneto-acoustic wave could propagate on larger distances than spin waves. Furthermore, using the low damping property of acoustic waves means that they can be excited remotely in the desired point on the magnetostrictive material. The research field that combines magnonics and strain (dynamic or static) has recently been referred to as straintronics [19].

Our research group started working with straintronics in 2010 by using optically excited strain pulses for the magnetization precession excitation in thin GaMnAs films [20]. These picosecond strain pulses were excited on the rear face of the sample and traveled through the substrate to arrive to the magnetic layer. This excitation was found not to be very efficient due to the weak coupling between the excited strain components and the magnetization, and the frequency and the wavevector mismatch between strain waves and spin waves. That is why in 2013 the group headed towards electrically excited surface acoustic waves. This type of acoustic waves, as they are named, propagate at the surface of the sample, where they are weakly damped, and their amplitude decreases exponentially in the depth of the material. It makes them ideal candidates for working with thin magnetic films. Heretofore, the group has reported magnetization switching and ferromagnetic resonance driven by surface acoustic waves [21, 14, 16]. In these experiments, changes in static magnetization were probed optically by static Kerr microscopy and magnetization dynamics was detected indirectly as the changes of surface acoustic wave amplitude and phase. A direct evidence of strain-wave induced magnetization dynamics was still missing. In 2015, the group decided to launch two new projects that became the subject of my PhD work: in the first one, surface acoustic waves were excited electrically and the *dynamic* magnetization was detected optically which had never been reported before (Chapter 6). In the second project surface acoustic waves were excited optically and magnetization/strain dynamics were also detected optically (Chapter 7). In between 2015 and 2018 many articles came out concerning similar physics. They have explored different geometries that will be detailed in Chapter 4. For the first project we worked with ferromagnetic semiconductor GaMnAs, a low Curie temperature ferromagnet but with adjustable magnetic properties. For a second one we turned to ferromagnetic metals with Curie temperature above room temperature.

We believe that the results presented in this work may contribute to improve the already existing concepts of magnon based signal processing or help to develop new ones.

The manuscript is organized as follows. In Chapter 1 the theory on magnetization dynamics will be introduced. We will describe the main components of the free energy of the ferromagnetic thin samples. Also the full energy expression for GaMnAs will be given. Later in the same chapter the concept of spin waves is discussed and the most common excitation techniques are shown, including magneto-acoustic coupling, to which this work is devoted. In Chapter 2 you will find the description of acoustic waves with a strong emphasis on surface acoustic waves. In Chapter 3 the theory of magneto-acoustics is shown. Chapter 4 presents the literature review on topics related to this thesis. The following chapters are dedicated to experiments. Thus, Chapter 5 recalls the experimental techniques used and shows the magnetic characteristics of the samples investigated. Chapter 6 contains the results of the first project, where surface acoustic waves were excited electrically and magnetization dynamics was detected optically. In the few first pages of this chapter, the experimental set-up that was developed is extensively described. Chapter 7 contains the experimental results for the second project, made in collaboration with Laurent Belliard. In this chapter many 2D maps of magneto-acoustic signal are shown.

1. Magnetization dynamics

Table of content

1.1. Landau-Lifshitz-Gilbert equation

The primary formulation of magnetization precessional motion was given in 1935 by L.D. Landau and E.M. Lifshitz [22, 23]. This is the elemental equation describing the undamped precessional motion of magnetic moments around the effective field. The effective field is the sum of all magnetic fields and it is defined as the derivative of the total energy of the ferromagnetic system with respect to $\vec{\boldsymbol{m}}$, described in the next paragraph. Surely, this is not the real situation, since the magnetization would keep precessing around the equilibrium position ($\vec{\boldsymbol{m}} \parallel \vec{\boldsymbol{H}}_{\boldsymbol{eff}}$) without energy dissipation, and it would never align with it. That is why in 1955 T.L. Gilbert proposed to add a damping part to the equation [24]. He introduced a small torque field which brings the magnetization towards the effective field. The spiral-like precessional motion, is understood as the nonlinear spin relaxation:

$$\frac{\partial \vec{\boldsymbol{m}}}{\partial t} = -\gamma \mu_0 \vec{\boldsymbol{m}} \times \vec{\boldsymbol{H}}_{\boldsymbol{eff}} + \alpha \vec{\boldsymbol{m}} \times \frac{\partial \vec{\boldsymbol{m}}}{\partial t} \tag{1.1}$$

where γ is the gyromagnetic factor ($\gamma > 0$), μ_0 is the permeability of vacuum, $\vec{\boldsymbol{m}}$ is the magnetization unit vector ($\vec{\boldsymbol{M}}/M_s$), α is the dimensionless damping factor.

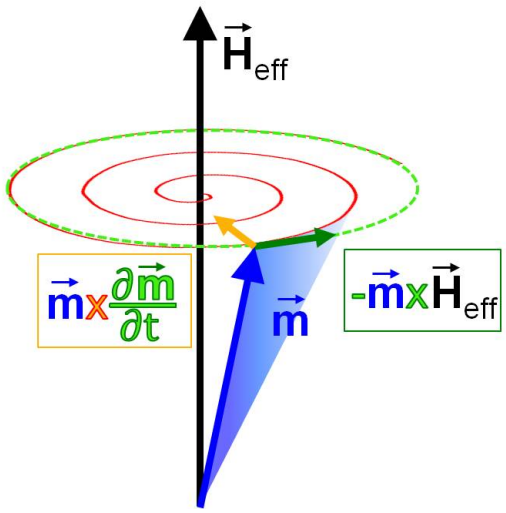

Figure 1.1.: The trajectory of the magnetization described by the Landau-Lifshitz-Gilbert equation.

1.2. Free energy density of the ferromagnetic material

The free energy density ($\frac{f}{V}$) of the ferromagnetic system contains the following contributions: Zeeman energy, exchange energy, demagnetization energy, magnetocrystaline anisotropy energy:

$$f^{Volume} = \frac{f}{V} = f_{Zeem} + f_{Exch} + f_{Dem} + f_{MCA} \tag{1.2}$$

The relation between the effective field and the energy is given by the following equation:

$$\vec{\boldsymbol{H}}_{\boldsymbol{eff}} = -\frac{1}{\mu_0}\vec{\boldsymbol{\nabla}}_m f \tag{1.3}$$

1.2.1. Zeeman energy

The Zeeman energy arises from the interaction of the magnetic moments with the external magnetic field. This energy is minimized when the magnetization lies along the direction of the magnetic field.

$$f_{Zeem} = -\mu_0 \left(\vec{\boldsymbol{M}} \cdot \vec{\boldsymbol{H}}\right) \tag{1.4}$$

1.2.2. Exchange energy

The long range order in the ferromagnetic materials originates from the exchange interaction between the electron spins. The theory of exchange interaction is based on the Pauli exclusion principle and Coulomb electrostatic forces. Because of the Pauli principle, parallel electron spins are spread away and this lowers the Coulomb interaction between them. The energy difference between the parallel and antiparallel spins is the exchange energy [25]. In quantum mechanics this can be written as the Heisenberg Hamiltonian:

$$\mathcal{H} = -\sum_{i,\,j} J_{ij} \vec{\boldsymbol{S}}_{\boldsymbol{i}} \cdot \vec{\boldsymbol{S}}_{\boldsymbol{j}} \tag{1.5}$$

S_i and S_j are the i and j spins and J_{ij} is the exchange integral between them. For ferromagnets J_{ij} is positive. For the continuous ferromagnetic medium the sum can be replaced by an integral. Keeping only nearest neighbors interaction (J), Equation 1.5 leads to an energy density [26, 27]:

$$f_{Exch} = A_{Exch} \mid \boldsymbol{\nabla} \vec{\boldsymbol{m}} \mid^2, \tag{1.6}$$

where A_{Exch} for cubic crystals is defined as $A_{Exch} = 2\frac{JS^2}{a}$ and a is the distance between the closest spins. In (Ga,Mn)As, Manganese spins are too dilute to interact directly. Instead, they interact via the spins of the delocalized holes. Hence, in GaMnAs A_{Exch} =0.4 pJ/m [28] is quite low compare to for example FeGa A_{Exch} =16 pJ/m [29].

1.2.3. Demagnetizing energy

The demagnetizing energy arises from the demagnetizing field $\vec{\boldsymbol{H}}_{Dem}$ and it is strongly dependent on the shape of the ferromagnetic sample. The energy is defined as an integral over the sample shape:

$$f_{Dem} = \frac{1}{2}\mu_0 \int\limits_{sample} \vec{\boldsymbol{M}} \cdot \vec{\boldsymbol{H}}_{Dem} dV \tag{1.7}$$

For a thin ferromagnetic film (thickness-d significantly smaller than the lateral dimensions) it becomes [30]:

$$f_{Dem}^{Volume} = \frac{1}{2}\mu_0 M_s^2 \cos^2\theta \tag{1.8}$$

where θ is the angle with the normal to the film plane. The energy is minimized when the magnetization lies in-plane and this is the equilibrium position for most very thin magnetic films ($d < 1\mu m$ [31]). Moreover, the demagnetizing energy is proportional to the square of the magnetization saturation, it means that for materials with a high M_s value, a huge magnetic field will need to be applied to bring the magnetization out of the sample plane. For instance metals have a very high M_s, the typical values are 1.7×10^6A/m for Fe, 1.4×10^6A/m for Co [27]. Therefore we will need around 2 T to magnetize a sample out of the plane. However, this value is much smaller for ferromagnetic semiconductors such as GaMnAs, the magnetization saturation for this material is around 3.3×10^4A/m [32] and then the required field is 40 mT.

1.2.4. Magnetocrystalline anisotropy energy

In crystalline materials, the magnetization prefers to orient along certain crystallographic axes. For these positions, the magnetocrystalline anisotropy (MCA) energy is minimized. In the literature, the axis with the lowest MCA energy for bulk materials is named easy axis, while the axis for which the energy is maximal is called hard axis. The MCA depends on the crystal symmetry, for instance the easy axes for body-centered cubic Iron are <100>. While for face-centered cubic Nickel, <111> are the easy axes [33]. The origin of MCA lies in the spin-orbit interaction and the interaction with the neighbor's atoms via the crystal field. Strongly coupled non spherically shaped orbitals will favor certain orientations of the spins. This applies to transition metals, while for GaMnAs the mechanism is different since the orbital angular momentum for the d^5 Mn electron configuration is zero (L=0). The interactions between the localized spins are mediated by the holes, which carry non zero total angular momentum, J≠0 (J=L+S) [34]. It is thus the valence band structure, in which holes reside, that will govern the anisotropy.

1.2.4.1. Phenomenological description of the magnetocrystalline energy

The most general formula of the MCA energy is given by the expansion series of the $\vec{\boldsymbol{m}}$ components [27]. For cubic systems with crystallographic axes oriented parallel to the xyz coordinate system, the MCA energy can be written as follows:

$$f_{MCA} = K_1(m_x^2 m_y^2 + m_y^2 m_z^2 + m_x^2 m_z^2) + K_2(m_x^2 m_y^2 m_z^2) + ... \tag{1.9}$$

K_1 and K_2 are the anisotropy constants (higher orders are often negligible). In many textbooks, you can find the above equation expressed by the directional cosines. Here we used a different notation for the reader's comfort. Hence the energy consists only of the K_i and square of $\vec{\boldsymbol{m}}$, the whole function is even. It means that we will consider only the orientation and not the direction of the easy and hard axis. This is caused by the crystal symmetry.

We will introduce now the MCA anisotropy for (Ga,Mn)As zinc-blende structure with a tetragonal distortion:

$$f_{MCA}^{GaMnAs} = -K_{2\perp}m_z^2 - \frac{K_{4\parallel}}{2}\left(m_x^4 + m_y^4\right) - \frac{K_{4\perp}}{2}m_z^4 - \frac{K_{2\parallel}}{2}\left(m_x - m_y\right)^2 \quad (1.10)$$

Equation 1.10 can be obtained from 1.9 by using the relationship for cubic crystals:

$$1 = \left(m_x^2 + m_y^2 + m_z^2\right)^2 = m_x^4 + m_y^4 + m_z^4 + 2\left(m_x^2m_y^2 + m_y^2m_z^2 + m_x^2m_z^2\right) \quad (1.11)$$

Therefore, the first term of equation 1.9 can be rewritten as:

$$f_{MCA} = \frac{K_1}{2}(m_x^4 + m_y^4 + m_z^4) \quad (1.12)$$

provided that the constant term is dropped. Hence you can notice that for (Ga,Mn)As with no tetragonal distortion:

$$K_{4\parallel} = K_{4\perp} = \frac{K_1}{2} \quad (1.13)$$

1.2.5. Equilibrium orientation of the magnetization

Once the most general static energy components were defined, the equilibrium position of the magnetization can be found. For the simplicity of the calculations we will work in the polar coordinate system:

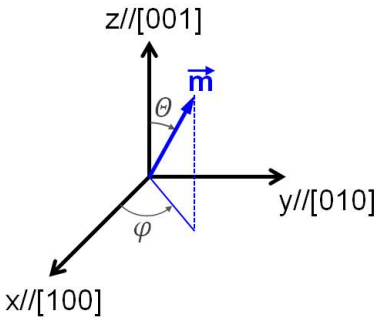

Figure 1.2.: Location of magnetization in polar coordinates system.

$$\begin{cases} m_x = \sin\Theta\cos\varphi \\ m_y = \sin\Theta\sin\varphi \\ m_z = \cos\Theta \end{cases} \tag{1.14}$$

Thus, the position of the magnetization $\vec{\boldsymbol{m}}$, will be defined by two angles, polar angle Θ measured with respect to the sample normal and the azimuthal angle φ equal zero when the magnetization is aligned along [100]. To find the equilibrium angles (φ_0 and Θ_0) of the magnetization we need to equate the derivatives $\frac{df}{d\varphi}$ and $\frac{df}{d\Theta}$ to zero. As an illustration we will use the energy expression for GaMnAs:

$$f_{GaMnAs} = -\mu_0 M_s H\left(\sin\Theta\sin\Theta_H\cos\left(\varphi-\varphi_H\right)+\cos\Theta\cos\Theta_H\right)+\frac{\mu_0 M_s^2}{2}\cos^2\Theta - K_{2\perp}\cos^2\theta$$

$$-\frac{K_{4\perp}}{2}\cos^4\Theta - K_{2\parallel}\sin^2\left(\varphi-\frac{\pi}{4}\right)\sin^2\Theta - \frac{K_{4\parallel}}{8}\left(3+\cos 4\varphi\right)\sin^4\Theta \tag{1.15}$$

The orientation of the easy axis depends on the sign and the magnitude of the anisotropy constants. In the (Ga,Mn)As studied in this thesis: $K_{2\perp} > K_{4\perp}$ and $K_{2\perp} < 0$, thus the polar angle Θ_0 is equal to $\frac{\pi}{2}$ and the easy axis will lie in the sample plane (001). For the in-plane anisotropy, the $K_{2\parallel}$ constant is critical. The azimuthal angle, for the case where $K_{2\parallel} > K_{4\parallel}$ and $K_{2\parallel} > 0$, is determined as $\varphi_0 = -\frac{\pi}{4}$. Hence the easy axis is along [1-10].

1.3. Spin waves

1.3.1. Types of spin waves

Spin waves are a coherent propagating weak excitation of spins in anti- and ferromagnets (Fig. 1.5 (a)). Spin waves present wave properties (Fig. 1.3). They can be reflected [35], diffracted [36], focused [37, 38], etc. Moreover, spin waves like acoustic waves or light, are quantized due to the wave-particle duality. The single quantum of the spin wave is a magnon with energy $\varepsilon = \hbar\omega(k)$.

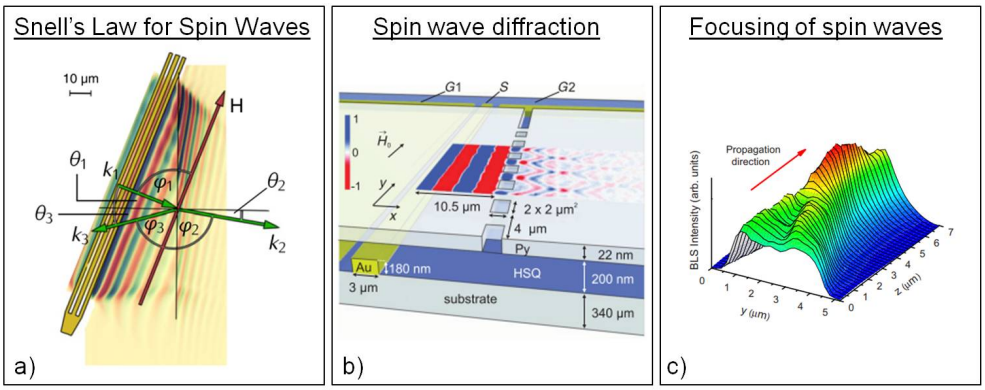

Figure 1.3.: Schemes of experimental concepts for spin waves a) reflection [35] and b) diffraction [36]. c) Map of the spin wave intensity in a Permalloy film [38].

Depending on the wavevector k value and orientation with respect to $\vec{\boldsymbol{M}}$ and $\vec{\boldsymbol{H}}$, different interactions will play a role in the spin wave propagation and different modes will be distinguished. Spin wave modes are described by the dispersion relation $\omega(k)$, which is commonly found by solving the LLG equation. Thus, equation 1.1 in spherical coordinates in the case of a small angle of precession is given as [21]:

$$\begin{cases} \delta\dot{\varphi} = \frac{\gamma}{\sin\Theta_0}\left(f_{\Theta\varphi}\delta\varphi + f_{\Theta\Theta}\delta\Theta\right) + \frac{\alpha}{\sin\Theta_0}\delta\dot{\Theta} \\ -\delta\dot{\Theta} = \frac{\gamma}{\sin\Theta_0}\left(f_{\varphi\varphi}\delta\varphi + f_{\varphi\Theta}\delta\Theta\right) + \alpha\delta\dot{\varphi}\sin\Theta_0 \end{cases} \tag{1.16}$$

where $f_{ln} = \frac{\partial^2 f}{\partial l \partial n}$ for l, $n = \varphi$ or Θ and the dot denotes the derivative with respect to time $\dot{l} = \frac{\partial l}{\partial t}$. Solving the LLG equations we are looking for the solution in k, thus $\vec{\boldsymbol{m}} = \vec{\boldsymbol{m}}_0 + \delta\vec{\boldsymbol{m}}e^{i\left(\vec{k}\vec{r}-\omega t\right)}$ is the plane wave. The wavevector puts different weight on the components of the free energy of the ferromagnet f: exchange energy (Section 1.2.2) and demagnetizing energy (Section 1.2.3), since the short range (exchange energy) and long range (demagnetizing energy) interactions have different dependence on k. Consequently, we can distinguish three main regions defined by k (Fig. 1.4) [39]:

- k $<10^5$ cm^{-1}: region dominated by the long range (long wavelength: $\lambda >$ 60 µm) dipole-dipole interactions. Those interactions are described by the demagnetizing energy. The spin waves belonging to this group are called magnetostatic spin waves. Depending on the $\vec{\boldsymbol{m}}$ orientation with respect to the external magnetic field and the sample planes, different spin waves can be discriminated [40].
- k $>10^6$ cm^{-1}: spin waves in this range are dominated by exchange interactions, the wavelength of those spin waves is short ($\lambda < 6$ µm).
- 10^5 cm$^{-1}<$ k $<10^6$ cm^{-1}: intermediate region were the two interactions have a similar influence: they are called dipole-exchange spin waves.

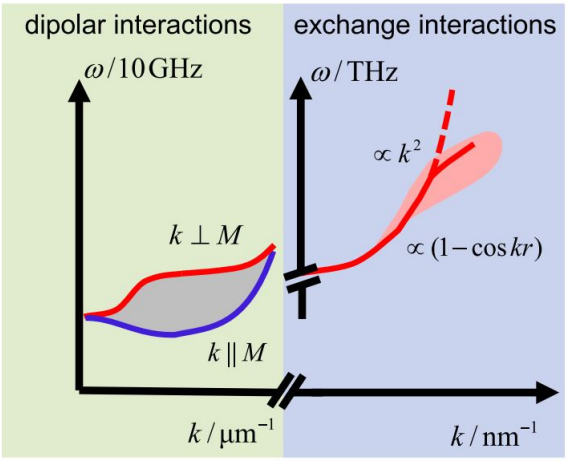

Figure 1.4.: Illustration of spin wave dispersion with two main regions: one dominated by the dipolar interactions and that other by the exchange interactions. From the slope of the presented curve the velocity of the propagating spin waves can be obtained. When the slope is 0, those are stationary (non propagating) spin waves. [41]

Moreover, the wavevector for a sample with finite lateral dimensions will be quantized due to the boundary conditions *e.g.* for the *magnetic wall* boundary condition, magnetization is pinned at the lateral edges. Thus the wavevector can only be integral multiples of the spin waves halfwavelength [42]. However, in this thesis $\vec{\boldsymbol{k}}$ was defined by the wavevector of SAWs, which was rather small: $k_{SAW} \leq \frac{2\pi}{4.7\mu m} \cong 1.3 \times 10^4$ cm^{-1}. The energy characteristic for this range of $\vec{\boldsymbol{k}}$ is flat and can be read as $\omega(k = k_{SAW}) \simeq \omega(k = 0)$ (Fig. 3.2). The wavelength of spin waves with $\vec{\boldsymbol{k}} = 0$ can be considered as infinite, which means that all magnetic moments precess in phase (Fig. 1.5). This mode is called the $uniform$ or FMR mode.

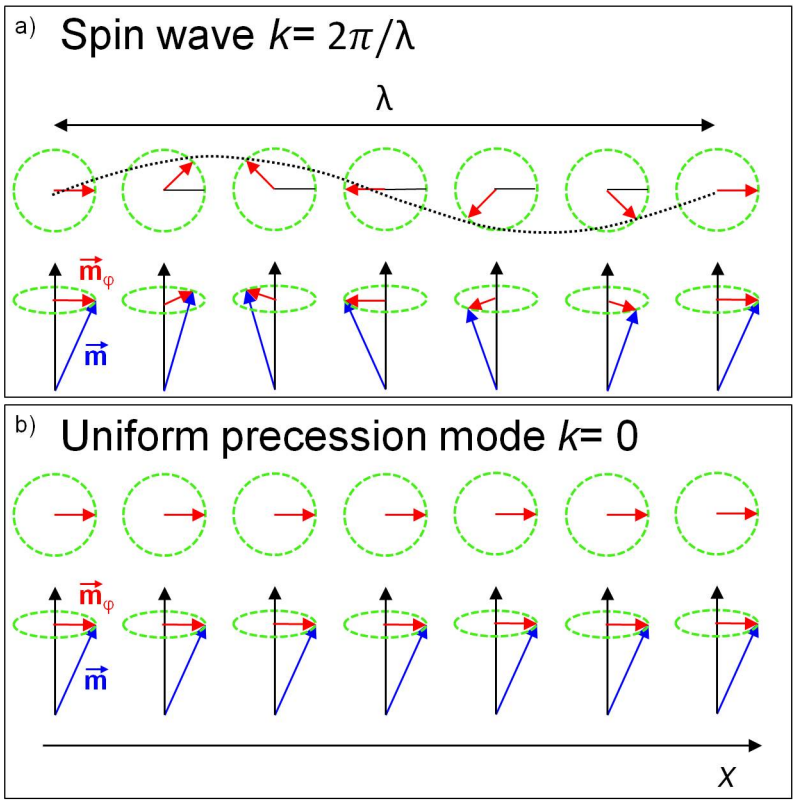

Figure 1.5.: Sketch of a spin wave with a a) finite and an b) infinite wavelength.

The uniform mode is for example excited by FMR (introduced in Chapter 5.1). The precession resonance frequency of the uniform mode can be calculated from the following formula or from equations 1.16 [21]:

$$\omega_p = \frac{1}{\sqrt{1+\alpha^2}}\sqrt{\omega_0^2 - \frac{\alpha^2\gamma^2\left(f_{\Theta\Theta} + \frac{1}{sin^2\Theta_0}f_{\varphi\varphi}\right)}{4M_s^2\left(1+\alpha^2\right)}} \tag{1.17}$$

where ω_0 is the precession frequency in case of zero damping:

$$\omega_0 = \frac{\gamma}{M_s \sin\Theta_0}\sqrt{f_{\Theta\Theta}f_{\varphi\varphi} - f_{\Theta\varphi}^2} \tag{1.18}$$

In most cases, it is sufficient to use the expression without damping. The typical values of damping are: for a 100 nm film of (Ga,Mn)As $\alpha = 0.03$ [43] and for a 100 nm thick Nickel film, $\alpha = 0.02$ [44]. The decay time of the magnetization precession is inversely proportional to α and ω. These damping constants might seem high compared to *e.g.* Yttrium Iron Garnet for which the damping is even 1000× smaller

[45], however Equation 1.18 can still be used with a good approximation. The precession frequency can be modified with the external magnetic field. With the field applied along the hard axis the precession frequency first decreases until the magnetization is aligned with it and after this point increases again (Fig. 1.6 - green curve). Applying the field along the easy axis we can only increase the precession frequency (Fig. 1.6 - red curve).

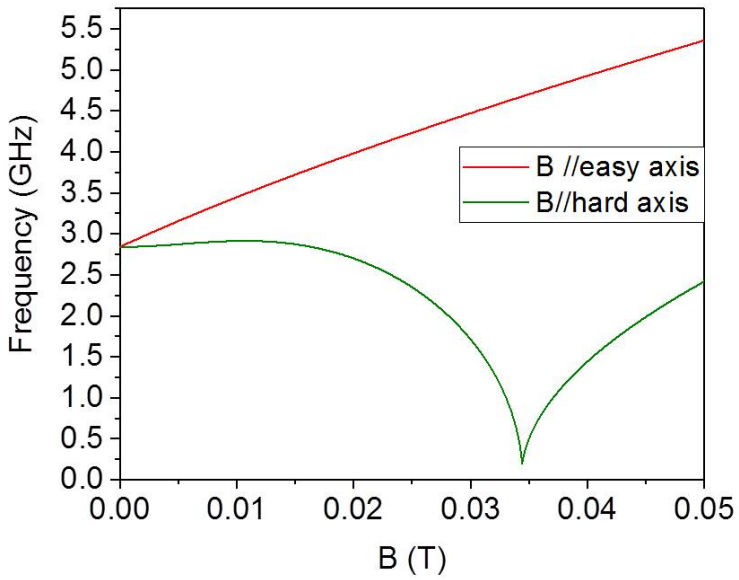

Figure 1.6.: Calculated dependence of FMR frequency for (Ga,Mn)As on magnetic field applied along an easy axis (red line) and a hard axis (green line).

The typical frequency values for ferromagnetic metals are in the range of 5-12 GHz [46]. For (Ga,Mn)As, in a low magnetic field, a resonance frequency below 3 GHz can be obtained.

1.3.2. Excitation of spin waves

There are many techniques to excite spin waves. The simplest one, already used in the 50's is the application of an external radio frequency (RF) magnetic field. The magnetization precession is excited by the RF magnetic field with an amplitude that reaches the maximum when the RF frequency equals the precession frequency. There are two main experimental configurations to perform this excitation. The RF magnetic field can be applied with the use of standing waves in a cavity, this method is called cavity-FMR, or with an RF Oestard field induced by a current flowing through a microstrip placed on the sample surface (Fig. 1.7 (a)). The latter technique is called broad-band FMR due to the fact that the frequency of the

flowing current can be easily tuned. For cavity FMR, tuning the frequency is not possible, since the microwave cavity where the sample is placed, is built to a specific frequency, typically 9, 36 or 115 GHz. However, cavity FMR is widely used for the measurement of the anisotropy constants. This will be discussed further in Chapter 5.1. With microstrip antenna, the propagating magnetostatic modes are excited, with the broad spectrum of wavevector for cases of a single microstrip.

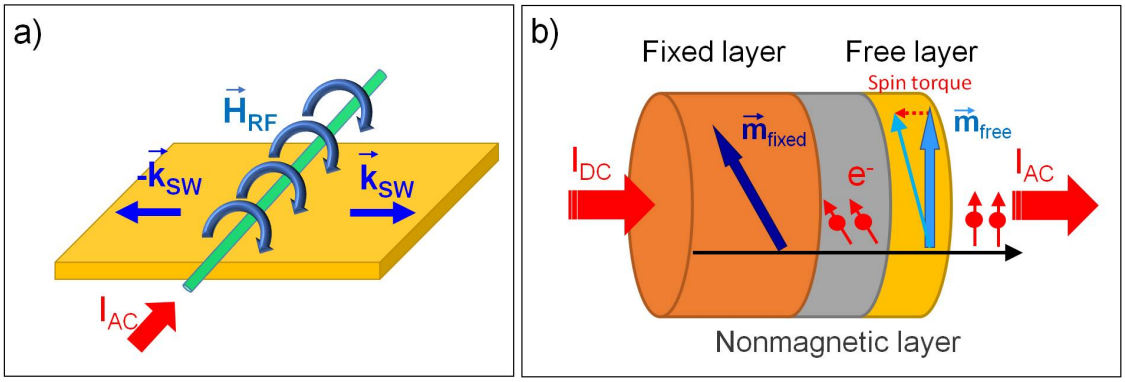

Figure 1.7.: Schematic (a) for antenna excitation spin waves and (b) nano torque oscillator device.

Other methods rely on a different physical mechanism to generate an internal effective RF field. The more recent method introduces the use of spin polarized current in magnetic tunnel junctions. A typical system for this type of excitation consists of three different layers (Fig. 1.7 (b)). Firstly, the hard ferromagnet (thick ferromagnetic layer) is used to polarize flowing charges. Then the current passes through a nonmagnetic layer and arrives to a free layer (thin ferromagnetic layer, with lower M_s than the fixed layer [47]). If the current is not polarized collinearly with the free layer configuration, then the exerted torque results in (uniform) oscillations of the free layer magnetization. The resistivity of the free layer depends on the respective $\vec{\boldsymbol{M}}$ orientation. Thus in the case of DC bias current, continuous oscillation of magnetization produces periodic changes in resistivity, hence an AC voltage [48]. The big advantage of this method is the accessibility to the large oscillation frequency even several tens of GHz as it can be tuned by current and the field. Moreover, the magnetization can be switched at zero magnetic field but it requires high current densities of about $10^7 \mathrm{A/m}^2$[49]. It means that the size of the device needs to be really small. Despite these requirements, it found the application in the second generation of MRAM and in devices taking advantage of the stochastic behavior of the magnetization switching [50]. Another potential application is the signal processing since the magnetization precession can modulate the electric signal.

The excitation of $\vec{\boldsymbol{M}}$ precession that is the most important in this work relies on the use of acoustic waves. They can periodically modify the magnetic anisotropy of a sample and in consequence, the magnetization will oscillate around a new equilibrium position. The acoustic waves, due to the low damping (they can propagate over

few mm distances without notable decrease of amplitude) are great candidates for the remote control of magnetization. The frequency content of spin waves excited with surface acoustic waves is typically in the MHz - GHz range.

2. Acoustic waves

Table of content

2.1. Types of acoustic waves

The term, *acoustic waves* can appear to be associated only with sound waves, nevertheless it is a broad term that covers all the mechanical vibration motions, from seismic waves, with frequencies below 1 Hz to THz hypersonic waves. An alternative name used interchangeably is elastic waves. Acoustic waves like other waves, obey the diffraction mechanism: the energy of the bulk propagating waves decreases as r^{-2}[51]. These are waves not restricted by the boundary conditions. However, these losses can be lowered to r^{-1}, by limiting the crystal with one or two parallel surfaces. With these configurations, only specific modes will be guided. These are either transverse or longitudinal displacements, propagating parallel to the surface. The three most known guided acoustic waves are:

- Lamb waves: waves with transverse and longitudinal displacement components propagating in a plate (Fig. 2.1(a)).
- Love waves: waves with single transverse component propagating at the surface of a semi infinite medium.
- Rayleigh waves: waves consisting of transverse and longitudinal displacement components, dephased by $\frac{\pi}{2}$ propagating at the surface of a semi infinite medium (Fig. 2.1(b)).

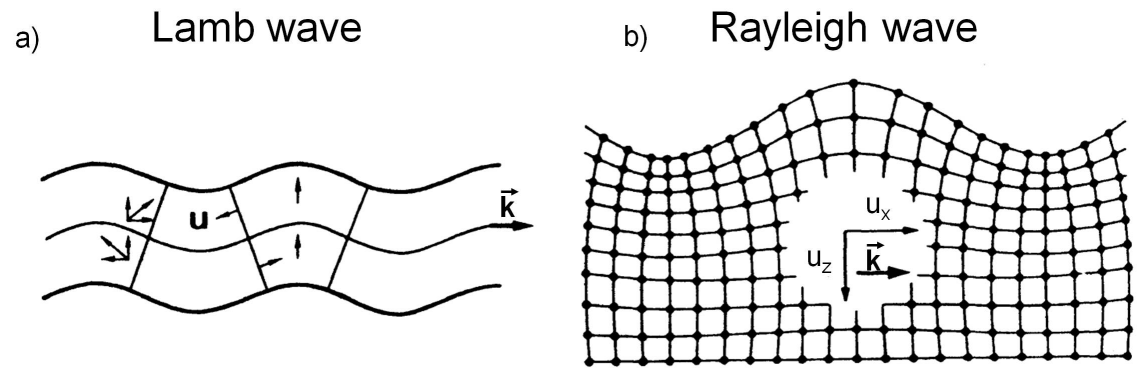

Figure 2.1.: Deformation of: (a) a plate for an antisymmetric Lamb mode and (b) the surface of a semi-infinit body for a Rayleigh wave[51]

The names of the listed waves come from the names of the British mathematicians who have discovered them: Horace Lamb, Augustus Edward Hough Love and John William Strutt, 3rd Baron Rayleigh. In this work we focused only on the Rayleigh waves, since the configuration of the semi-infinite film is suitable for thin films on a substrate and the two displacement components give more possibilities to influence the magnetization (see Chapter 3). Rayleigh waves were discovered in 1885. A great emphasis was placed on the contribution of these waves to earthquakes. Rayleigh waves are also simply called surface acoustic waves (SAWs) since there are strongly confined to the surface of the material. The penetration depth of the SAW is of the order of its wavelength. Since Rayleigh waves propagate on the surface of the body, they are accessible from one side during the whole propagation path, which makes them attractive for many applications, such as acoustic tweezers used to manipulate even a single particle[52] or sensors to measure the material strength[53], temperature[54], humidity, fluid flow[55] and more.

2.2. Elastic energy

To define the elastic energy of the solid, we will first remind some basic concepts such as displacement, strain and stress. Let us consider a 1D spring hooked at the point 0 (Fig. 2.2). When the spring is not deformed, the other end lies at the point x. Then when we stretch the spring form the point x to x', the displacement is defined as the difference between the position of those two points $u = x' - x$.

From that we can introduce strain as the dimensionless ratio of the displacement to the original length $S = \frac{du}{dx}$, it is true for small deformations. Strain for the 3D solid becomes a tensor $S_{ij} = \frac{du_i}{dx_j}$, where i and j take values from 1 to 3. A spring is a great example of the elastic object. Elastic materials can be deformed by external forces but when the forces vanish the object returns to its original size. The force which

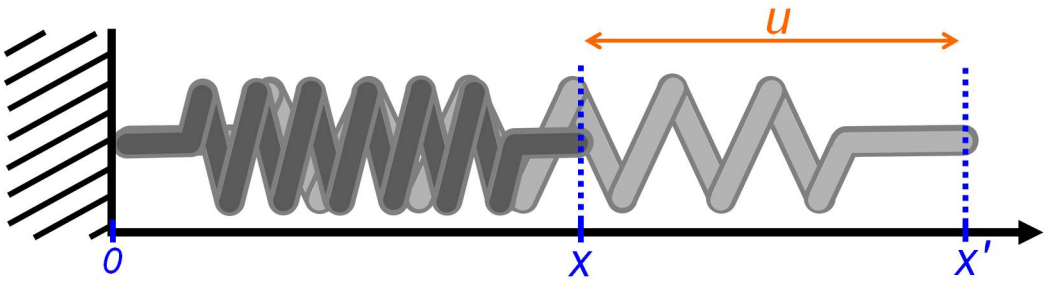

Figure 2.2.: Illustration of the displacement concept with the example of a spring.

works against the external deformation forces is the mechanical traction force. The vector of the mechanical traction forces ($\vec{\boldsymbol{\sigma}}$) of the element of the volume is defined as the force acting on the surface area: $\vec{\boldsymbol{\sigma}} = \frac{d\vec{F}}{ds}$. The mechanical stress acting on the body can be found from the equilibrium condition when the mechanical traction balances the volume forces. According to Hooke's law, for a non piezoelectric body, stress is related to strain by $\sigma_{ij} = c_{ijkl}S_{kl} = c_{ijkl}\frac{du_l}{dx_k}$, where c_{ijkl} is the stiffness tensor in linear elasticity. It can be shown that only the symmetric part of the strain tensor $S_{ij} = \frac{1}{2}\left(\frac{du_i}{dx_j} + \frac{du_j}{dx_i}\right)$ defines a deformation. Now the elastic energy can be introduced as the sum of all kinds of strains working on an elastic body[56, 51]:

$$f_{el} = \frac{1}{2}\sigma_{ij}S_{kl} = \frac{1}{2}c_{ijkl}S_{ij}S_{kl} \tag{2.1}$$

Since σ_{ij} and S_{kl} are both symmetric tensors, the number of independent components of the stiffness tensor is lowered from 3^4= 81 to 36. In a cubic crystal this tensor has only 3 independent components, when the Voigt notation is used[1]:

$$c_{ij}^{cubic} = \begin{pmatrix} c_{11} & c_{12} & c_{12} & 0 & 0 & 0 \\ c_{12} & c_{11} & c_{12} & 0 & 0 & 0 \\ c_{12} & c_{12} & c_{11} & 0 & 0 & 0 \\ 0 & 0 & 0 & c_{44} & 0 & 0 \\ 0 & 0 & 0 & 0 & c_{44} & 0 \\ 0 & 0 & 0 & 0 & 0 & c_{44} \end{pmatrix} \tag{2.2}$$

The typical values of the stiffness constants at a room temperature for a few chosen materials are presented in the table below.

The values of the stiffness constants are of the order of 10^{10}N/m^2. The material with the highest hardness is Diamond, thus it has the highest stiffness constants.

[1]Simplifications of subscripts for the Voigt notation: 11 → 1, 22 → 2, 33 → 3, 23 → 4, 31 → 5, 12 → 6

Material	Stiffness (10^{10}N/m^2)			Mass density (10^3 kg/m^3)	Velocity (10^3 m/s)		
	c_{11}	c_{12}	c_{44}	ρ	V_L	V_T	V_R
Gallium Arsenide[51]	11.88	5.38	5.94	5.3	4.7	3.4	2.7
Silica[51]	7.85	1.61	3.12	2.2	6.0	3.8	3.4
Nickel[56, 57]	24.9	15.2	11.8	8.8	5.3	3.7	2.8
Sapphire†[58]	49.6	15.8	14.5	4.0	11.1	6.0	–
Diamond[58]	102	25	49.2	3.5	17.1	11.9	10.3

Table 2.1.: Values of the stiffness, mass density and longitudinal (V_L), transverse (V_T) and Rayleigh (V_R) velocities for a few materials.†Sapphire is a trigonal crystal, so the stiffness tensor is more complicated. It has three more independent constants: c_{33}, c_{13}, c_{14}.

The stiffness constants are important also for another reason, they will determine the sound velocity as will be shown in the next paragraph. Now we can show a more explicit formula of the elastic energy for the cubic structure[51]:

$$f_{el}^{cubic} = \frac{1}{2}c_{11}\left(S_{11}^2 + S_{22}^2 + S_{33}^2\right) + 2c_{44}\left(S_{13}^2 + S_{23}^2 + S_{12}^2\right) + c_{12}\left(S_{11}S_{22} + S_{22}S_{33} + S_{33}S_{11}\right) \tag{2.3}$$

2.3. Wave equation

The equation of motion for the elastic body in the presence of space and time varying stresses can be written as follow[51, 59]:

$$\rho\frac{\partial^2 u_i\left(\vec{r},t\right)}{\partial t^2} = \frac{\partial \sigma_{ij}}{\partial x_j} = c_{ijkl}\frac{\partial S_{kl}\left(\vec{r},t\right)}{\partial x_j} \tag{2.4}$$

ρ is the mass density. This is valid for non piezoelectric materials. In the case of piezoelectric materials, the mechanical displacement is coupled to the electromagnetic wave, so an extra term needs to be added to 2.4: $e_{kij}\frac{\partial^2\phi}{\partial x_j \partial x_k}$, where e_{kij} is the piezoelectric tensor and ϕ the electric potential. However, for non piezoelectric materials or weak piezoelectric materials, the electromagnetic wave is seen only as a small perturbation of the mechanical displacement, hence it can be neglected. We will use this approach to GaAs where piezoelectric constants are much weaker than for instance in lead zirconate titanate (PZT- the most widely used piezoelectric material)[58] and will not affect much the wave equation.

2.4. Rayleigh waves

We will now solve the wave equation for Rayleigh waves propagating along the [100] direction in a nonpiezoelectric material with the cubic symmetry (see Fig. 2.3).

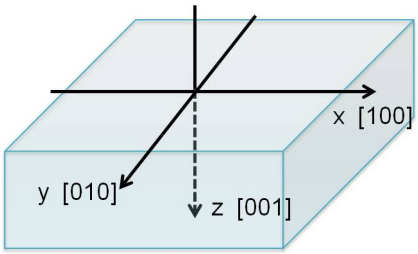

Figure 2.3.: Orientation of the xyz coordinate system with respect to the crystallographic axes.

For simplicity the axes x_1, x_2, x_3 will be denoted simply as x, y, z. We are looking for harmonic Rayleigh plane wave solutions of Equation 2.4 of this form:

$$\begin{cases} u_x = U_x e^{-bz} e^{i(\omega t - kx)} \\ u_y = U_y e^{-bz} e^{i(\omega t - kx)} \\ u_z = U_z e^{-bz} e^{i(\omega t - kx)} \end{cases} \tag{2.5}$$

with $\omega = V_R k$. We assumed here that the three displacement components u_x, u_y and u_z decrease exponentially with the depth (b needs to be positive). No y dependence is taken into account ($\frac{\partial}{\partial y}$=0), since the motion is taken as invariant along y. Applying Equation 2.5 to the wave equation 2.4 we get the system of three equations:

$$\begin{cases} \rho \frac{\partial^2 u_x}{\partial t^2} = c_{11} \frac{\partial^2 u_x}{\partial x^2} + c_{12} \frac{\partial^2 u_z}{\partial x \partial z} + c_{44} \left(\frac{\partial^2 u_x}{\partial z^2} + \frac{\partial^2 u_z}{\partial x \partial z} \right) \\ \rho \frac{\partial^2 u_y}{\partial t^2} = c_{44} \left(\frac{\partial^2 u_y}{\partial x^2} + \frac{\partial^2 u_y}{\partial z^2} \right) \\ \rho \frac{\partial^2 u_z}{\partial t^2} = c_{11} \frac{\partial^2 u_z}{\partial z^2} + c_{12} \frac{\partial^2 u_x}{\partial x \partial z} + c_{44} \left(\frac{\partial^2 u_z}{\partial x^2} + \frac{\partial^2 u_x}{\partial x \partial z} \right) \end{cases} \tag{2.6}$$

The u_y displacement component is decoupled from the other two, furthermore it will not be excited in our experimental geometry therefore we will consider only u_x and u_z displacements (Section 6.3.5.1). Searching for a non trivial solution we equal the determinant to zero:

$$\begin{vmatrix} -k^2 c_{11} + b^2 c_{44} + \rho\omega^2 & ibk\,(c_{12} + c_{44}) \\ ibk\,(c_{12} + c_{44}) & -k^2 c_{44} + b^2 c_{11} + \rho\omega^2 \end{vmatrix} = 0 \tag{2.7}$$

From that we can find two roots of damping parameters b. For simplicity of the calculation it was replaced by the dimensionless ratio $q = \frac{b}{k}$. In the isotropic case (c_{12}=c_{11}-2c_{44}) , the roots of 2.7 are given as:

$$q_1 = \sqrt{1 - \frac{\rho V_R^2}{c_{11}}} \qquad q_2 = \sqrt{1 - \frac{\rho V_R^2}{c_{44}}} \tag{2.8}$$

where $V_R = \frac{\omega}{k}$, is the Rayleigh velocity and the ratios in front of it correspond to the longitudinal and transverse wave velocities $V_L = \sqrt{\frac{c_{11}}{\rho}}$ and $V_T = \sqrt{\frac{c_{44}}{\rho}}$. Typical velocity values are given in Table 2.1. For q_i to be real, V_R needs to fulfill the inequality $V_R < V_T < V_L$. The amplitude ratios are given as:

$$\frac{U_{z,1}}{U_{x,1}} = -iq_1 \qquad \frac{U_{z,2}}{U_{x,2}} = \frac{-i}{q_2} \tag{2.9}$$

We cannot satisfy the boundary condition $\sigma_{zz} = 0$ with expression 2.5 of the displacement, so we need to find the solution as a linear condition of the two:

$$\begin{cases} u_x = \left(U_{x,1}e^{-q_1 kz} + U_{x,2}e^{-q_2 kz}\right) e^{i(\omega t - kx)} \\ u_z = \left(-iq_1 U_{x,1}e^{-q_1 kz} + \frac{-i}{q_2}U_{x,2}e^{-q_2 kz}\right) e^{i(\omega t - kx)} \end{cases} \tag{2.10}$$

To find the relation between the amplitudes $U_{x,1}$ and $U_{x,2}$ we need to apply the mentioned boundary conditions. For a semi infinite solid the mechanical traction at the surface is zero $\sigma_{iz} = 0$ (at z=0). Again we get a system of two equations:

$$\begin{cases} \sigma_{xz} = c_{44}\left(\frac{\partial u_z}{\partial x} + \frac{\partial u_x}{\partial z}\right) = 0 \\ \sigma_{zz} = c_{12}\frac{\partial u_x}{\partial x} + c_{11}\frac{\partial u_z}{\partial z} = 0 \end{cases} \tag{2.11}$$

The ratio between the amplitudes is obtained from the zero of the determinant of these two equations:

$$\frac{U_{x,2}}{U_{x,1}} = -2\frac{q_1 q_2}{1 + q_2^2} \tag{2.12}$$

From Equation 2.11 we can find the master equation for the velocity:

$$\left(c_{44} - \rho V^2\right)\left(c_{11}^2 - c_{12}^2 - c_{11}\rho V^2\right)^2 = c_{11}c_{44}\left(c_{11} - \rho V^2\right)\rho^2 V^4 \tag{2.13}$$

Solving this 8th order equation gives six values of V. The real Rayleigh velocity is the one that fulfills the condition $V_R < V_T < V_L$. Examples of Rayleigh velocities are given in Table 2.1. For anisotropic solids the Rayleigh velocity depends on the propagation direction. For instance in case of acoustic waves propagating along [110] after similar calculations we can find that the Rayleigh velocity is given as follows:

$$\left(c_{44} - \rho V^2\right)\left(c'_{11}c_{11} - c_{12}^2 - c_{11}\rho V^2\right)^2 = c_{11}c_{44}\left(c'_{11} - \rho V^2\right)\rho^2 V^4, \tag{2.14}$$

where $c'_{11} = \frac{1}{2}c_{11} + \frac{1}{2}c_{12} + c_{44}$.

Equation 2.13 can be expressed as a function of ω and k:

$$\left(c_{44} - \rho\frac{\omega^2}{k^2}\right)\left(2c_{44}^2 - c_{11}\rho\frac{\omega^2}{k^2}\right)^2 = c_{11}c_{44}\left(c_{11} - \rho\frac{\omega^2}{k^2}\right)\rho^2\frac{\omega^4}{k^4} \tag{2.15}$$

This is the equation of the acoustic wave dispersion, the dispersion of the three modes can be found from it: longitudinal, transverse and Rayleigh. There are plotted for GaAs in figure 2.4.

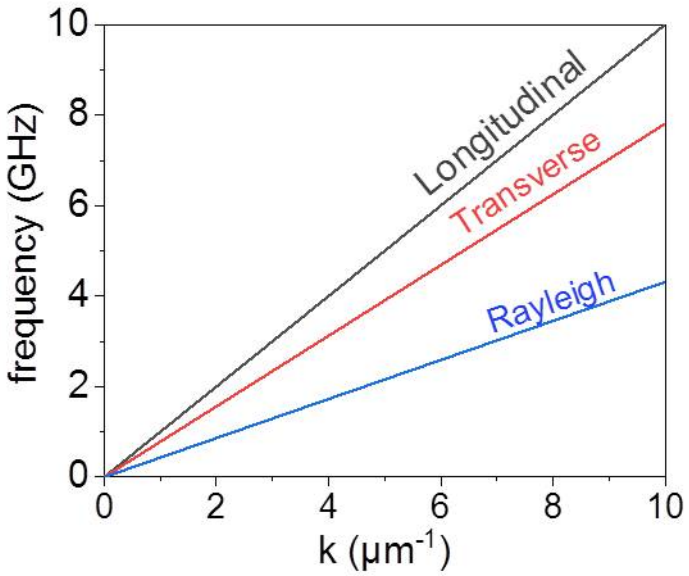

Figure 2.4.: The dispersion of longitudinal, transverse and Rayleigh waves for GaAs.

The dispersion of the three modes is linear. The slope will give the group velocity (v_g) of certain SAW mode (for non-dispersive waves phase velocity is constant v_p = const. and the two velocities are equal $v_g = v_p$). The wave with the highest speed is

longitudinal, then come the transverse and as the combination of the two, Rayleigh wave has the lowest velocity.

Now making use of the amplitude ratio 2.12, we can express the displacements by the common amplitude $U_{x,1}$, which depends on the excitation:

$$\begin{cases} u_x = U_{x,1}\left(e^{-q_1 kz} - 2\frac{q_1 q_2}{1+q_2^2}e^{-q_2 kz}\right)e^{i(\omega t - kx)} \\ u_z = iq_1 U_{x,1}\left(-e^{-q_1 kz} + \frac{2}{1+q_2^2}e^{-q_2 kz}\right)e^{i(\omega t - kx)} \end{cases} \tag{2.16}$$

As a result of i unit before the expression for the u_z component, longitudinal and transverse displacements (u_x and u_z) are in phase quadrature, the two sinusoidal waves are shifted by $\frac{\pi}{2}$ at any place of the wave propagation. The displaced particles move in an ellipse. The typical displacement values are rather small of the order of Å [60]. The variation of the two displacement component with depth for GaAs is plotted in Fig. 2.5. Close to the surface the transverse longitudinal component is much bigger than the longitudinal. Moreover, the longitudinal component decreases very rapidly with depth and changes sign at $z/\lambda = 0.2$.

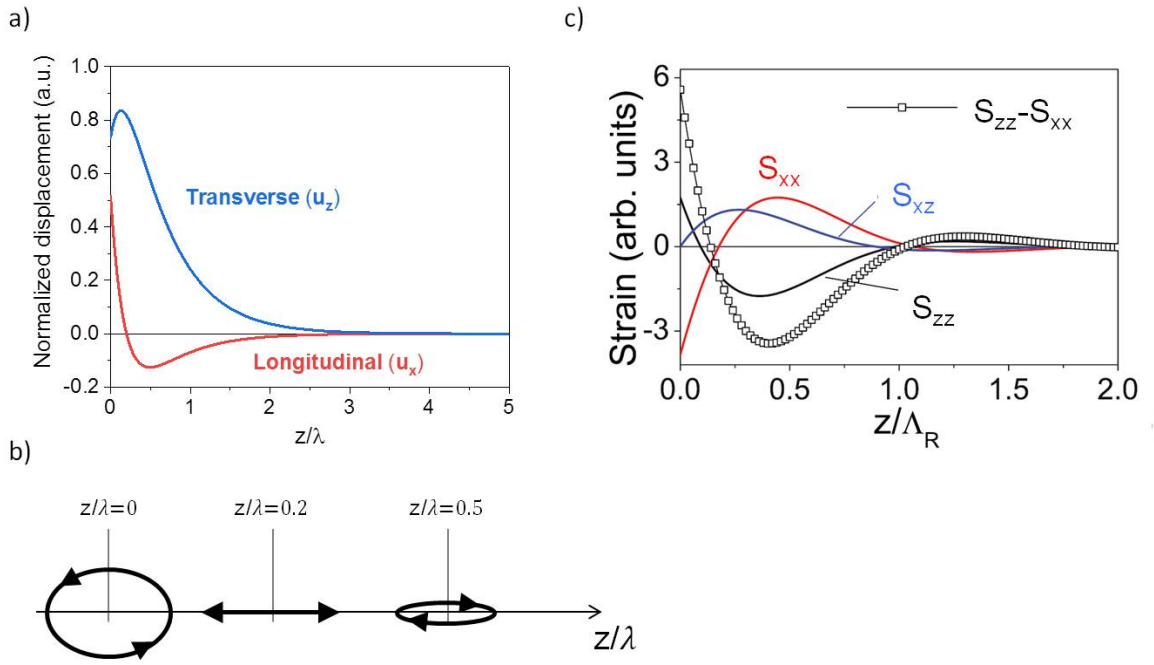

Figure 2.5.: a) Depth dependence of Longitudinal and Transverse components of the Rayleigh waves for GaAs. b) Illustration of the particle motion at the three chosen depths. c) Strain components of the Rayleigh waves for the semi-infinite GaAs [21]. It is worth noticing that the shear strain S_{xz} is zero at the surface.

In case of a thin film on a substrate, the displacement relation will be perturbed. For the substrate the displacement remains unchanged, while close to the surface

of the film, the strain will be modified. This case was studied *e.g.* by Farnell and Adler[61].

In this thesis, the study of (Ga,Mn)As/GaAs is well described by a semi-infinite model. The study of metals on STO, glass and Sapphire are better described by a film over substrate approach.

2.5. Excitation of acoustic waves

Acoustic waves are excited by a time-varying stress. There are two main approaches to realize that, one is optical with the use of laser pulses and the second one is electrical with the piezoelectric effect.

2.5.1. Optical excitation technique

A laser irradiating the surface of an elastic body makes its temperature rise. As a result the heated part of the body expands in size. If this thermally excited stress is rapid enough, bulk and surface acoustic waves are produced. We will start our discussion from the laser point source, however there are also different configurations as will be pointed out later. Commonly the sample consists of a metallic layer on top of the substrate. The metallic film absorbs the laser pulses and transfers the heat to the substrate (which must usually have a high sound velocity in order to obtain a high frequency). The distribution of the temperature close to the excitation area is described by the thermal diffusion equation[62, 63]:

$$\nabla^2 T + \frac{1}{K} w_a = \frac{1}{\kappa} \frac{\partial T}{\partial t} \tag{2.17}$$

K is the thermal conductivity coefficient, κ is the thermal diffusivity, and w_a is the absorbed laser power per unit volume defined as:

$$w_a = \frac{AQ}{2\pi r} \delta(t)\delta(r)\delta(z) \tag{2.18}$$

A is the the proportion of incident light absorbed in the material ($A = \frac{I-R}{I}$) and dielectric permittivity of the material, Q is the laser pulse energy. Then stresses induced thermally are given as:

$$\sigma_{ij} = c_{ijkl} \xi \Delta T \delta_{kl} \tag{2.19}$$

where ξ is the isotropic thermal expansion coefficient, δ_{kl} is a Kronecker delta and ΔT is the temperature increase. Now we have a link between the increase of temperature and stress, Equation 2.4 can be solved for the SAW propagation. This problem was solved previously *inter alia* by Rose [64] and the result for the out-of-plane displacement at the surface for an isotropic solid was shown by Aussel *et al.* [62]. In Fig. 2.6 we show an example for a pulse laser excitation.

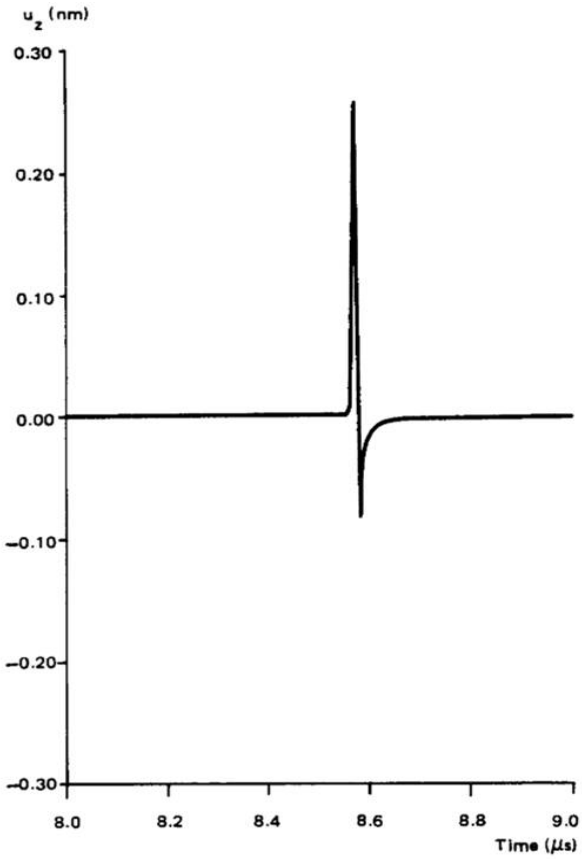

Figure 2.6.: Theoretical displacement upon the irradiation of 25 mm thick Aluminium plate with Gaussian laser pulse of 10 ns duration [62].

Moreover, the SAW generated with a laser spot having a finite space and time excitation was calculated with the response to the δ- like function [65] p.748.

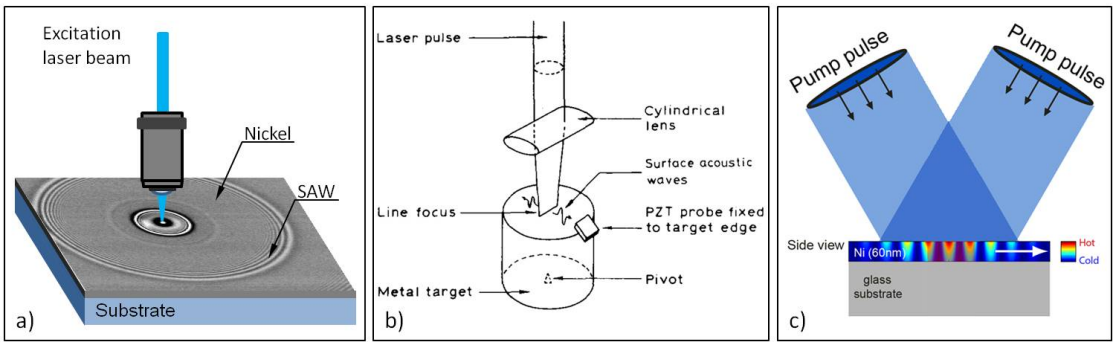

Figure 2.7.: Illustration of the three different photothermal SAW excitation configurations: a) with a point-like laser spot, b) with a line shaped spot [66], c) with interference fringes [67].

The advantages of optical excitation are that the surface is free of any mechanical contact, acoustic waves can be excited with different shapes of the laser spot (i.e. line spot Fig 2.7 (b)[66]). Moreover the excitation of SAWs can be easily performed on curved surfaces [68]. The bandwidth of the excited waves can be narrowed by the use of the transient grating technique, where two coherent laser beams interfere at the material surface and produce bidirectional SAWs propagating in opposite directions. The wavelength of the SAW is defined by the spacing between the fringes and can easily be tuned by changing the angle between the two beams. In this case, the laser pulse energy is transferred to a single wavelength. This method is limited to high frequencies since the interferometric spot must contain a sufficient number of fringes to generate the narrowband SAWs. For a low frequency ($f_{SAW} < 500$ MHz), the wavelength is long ($\lambda_{SAW} > 5$ µm) and thus the big beam spot with high fluence is needed (d > 200µm for 40 periods).

2.5.2. Electrical excitation technique

The most common technique to excite acoustic waves electrically consists of comb shaped electrodes in zipper configuration on the surface of a piezoelectric material (Fig. 2.8 (a)). In piezoelectric materials, electrical charges accumulate at the surface under stress, and strain is generated under applied electric field.

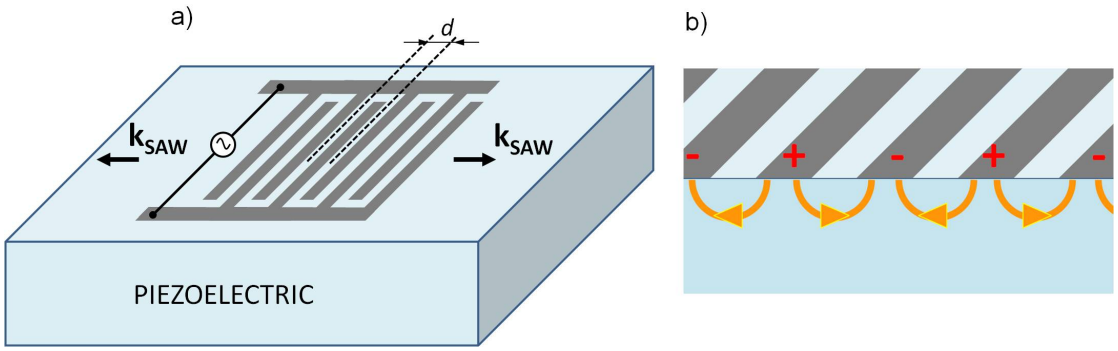

Figure 2.8.: a) The concept of a simple IDT. b) The cross section of the IDT. Opposite charges, distributed alternatively create the electric field which generates the strain in piezoelectric materials.

This phenomena is well illustrated by the electrical displacement equation for piezoelectric materials[69]:

$$D_i = d_{ij}E_j + e_{ikl}S_{kl}, \tag{2.20}$$

where d_{ij} is the dielectric tensor, E_j are the components of the electric field and e_{ikl} is the piezoelectric tensor. Conversely, by the inverse piezoelectric effect, an electric field applied to a surface generates mechanical stresses:

$$\sigma_{jk} = c_{jklm}S_{lm} - d_{ijk}E_i \tag{2.21}$$

To generate the electric field, an interdigitated transducer (IDT) is used. Let us consider the IDT shown in Fig. 2.8. In the cross section of the IDT, an electric potential occurs alternatively when the applied voltage is sinusoidal (Fig. 2.8 (b)). Depending on the sign of the induced electric field, the material is in compressive or tensile strain. As a result, SAWs propagate perpendicular to the electrodes in the two directions. The spacing d between the metallic teeth together with the Rayleigh velocity determine the frequency of the emitted acoustic waves. The resonance frequency of the IDT is given as $f = \frac{V_R}{2d}$. The number of pairs of teeth defines the bandwidth. By increasing it, the bandwidth will be narrowed. Playing with the design of the IDT, various types of waves can be excited, not only SAW plane waves but also SAWs with a curved wavefront (Fig. 2.9 (a)) [70] used for example to focus the SAW in confinement structures [71]. Excitation of SAWs on spherical surfaces is more demanding than with the laser pulses however, it was achieved as reported in [72] (Fig. 2.9 (b)). More details on the geometry and working principles of the IDTs used in our experiment will be given in Section 6.1.4.

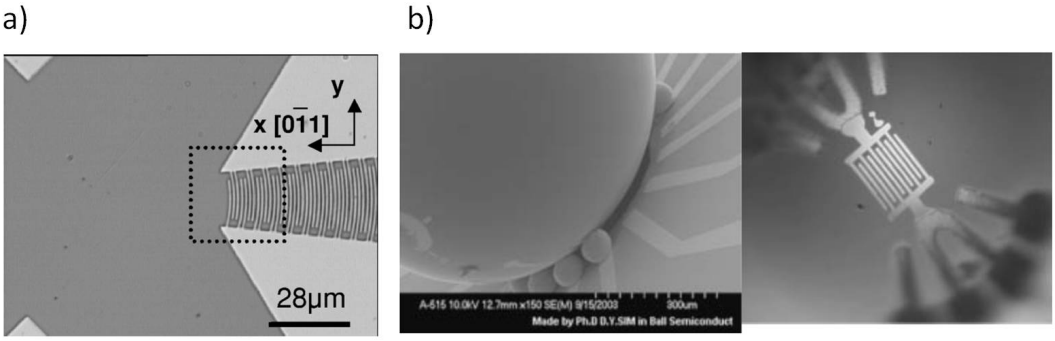

Figure 2.9.: a) Image of the IDT for focused SAWs [70] b) A Quartz 1 mm big (diameter) sphere with supports and IDT for 156 MHz used as a gas sensor [72].

3. Magneto-elastic dynamics

Table of content

3.1. Magnetostriction

Ferromagnetic materials change dimensions upon application of a strong magnetic field (Fig. 3.1 (a)), this phenomenon is called magnetostriction and it was discovered in 1842 by J.P. Joule. Magnetostriction is quantified by the saturation magnetostriction strain coefficient, which for isotropic materials is simply defined as: $\lambda_s = \frac{\Delta l}{l}$ (Fig. 3.1 (b)). This is the measure of strain arising after the application of the saturation magnetic field. One of the strongest known magnetostrictive material is Terfenol-D (alloy of Tb, Dy and Fe) for which $\lambda_s = 2.4 \times 10^{-3}$ [73]. Typically this coefficient is of the order of 10^{-5} *e.g.* for Fe[56]. The inverse process whereby under the mechanical deformation the magnetization properties change is named inverse magnetostriction or Villari effect. This work will take advantage of the latter effect.

3.2. Magneto-elastic energy

The microscopic origin of magnetostriction is the same as MCA discussed in paragraph 1.2.4, it is due to the spin-orbit coupling. In the presence of external magnetic field, spins of electrons will align with it, which will change the orbitals shape. Hence, as a result of orbital-lattice coupling, interatomic separation will be changed, therefore the macroscopic dimensions [75]. Hence, the MCA energy can be expanded in

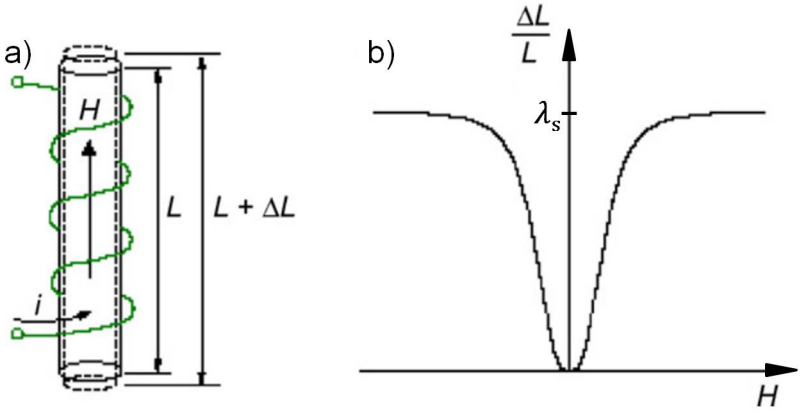

Figure 3.1.: Changes of the dimensions of magnetostrictive material upon application of the magnetic field showed (a) schematically and (b) in the graph [74].

Taylor series about the equilibrium position[76, 77]:

$$f_{MCA} = f^0_{MCA} + \left.\frac{\partial f_{MCA}}{\partial S_{ij}}\right|_0 S_{ij} + ... \tag{3.1}$$

The term that depends on strain is the magneto-elastic energy, it describes the coupling between magnetization and strain. Keeping only terms up to the second order in the magnetization components it is written as:

$$f_{MEl} = \left.\frac{\partial f_{MCA}}{\partial S_{ij}}\right|_0 S_{ij} = B_{ijkl} m_i m_j S_{kl} \tag{3.2}$$

where B_{ijkl} is the magneto-elastic coupling tensor. In the case of cubic symmetry this tensor reduces to two constants, and the magneto-elastic energy becomes [14]:

$$f^{cubic}_{MEl} = B_1 \left(m_x^2 S_{xx} + m_y^2 S_{yy} + m_z^2 S_{zz}\right) + 2B_2 \left(m_x m_y S_{xy} + m_y m_z S_{yz} + m_z m_x S_{zx}\right) \tag{3.3}$$

For non magnetostrictive materials the constants B_1 and B_2 are equal to zero and no coupling to strain occurs. For bulk magnetostrictive materials, the magneto-elastic coupling constants can be calculated from the magnetostriction coefficients:

$$B_1 = -\tfrac{3}{2}\lambda_{100}\left(c_{11} - c_{12}\right) \qquad B_2 = -3\lambda_{111} c_{44} \tag{3.4}$$

λ_{100} and λ_{111} are the saturation magnetostriction constants measured for magnetization aligned along the [100] and [111] directions. Thus the magneto-elastic energy is often presented in the literature with use of λ_s constants, here in a more general form [78]:

$$f_{MEl} = -\frac{3}{2}\lambda_{100}\left(c_{11} - c_{12}\right) m_i^2 S_{ii} - 3\lambda_{111} c_{44} m_i m_j S_{ij} \tag{3.5}$$

3.2.1. Contribution of magneto-elasticity to the magnetocrystalline anisotropy energy

In the Villari effect, stress is imposed externally. For magnetic films it is commonly introduced with the epitaxy where the mismatch between the substrate lattice and magnetic film can be carefully defined in order to lower the crystal symmetry. The epitaxial strain will contribute to MCA energy through the magneto-elasticity. Thus the magnetocrystalline and magneto-elastic energy for our material can be written as follows [79]:

$$f_{MCA} + f_{MEl} = B_c(m_x^4 + m_y^4 + m_z^4) + B_1(m_x^2 S_{xx} + m_y^2 S_{yy} + m_z^2 S_{zz})$$

$$+2B_2\left(m_x m_y S_{xy} + m_y m_z S_{yz} + m_z m_x S_{zx}\right) \tag{3.6}$$

B_c is the cubic anisotropy constant and B_1, B_2 are the magneto-elastic constants. The formula 3.6 is different than one presented in [14], here the quadratic terms of m in magneto-elastic energy were neglected. To determine the magneto-elastic constants in (Ga,Mn)As, the epitaxial strains are measured with X-ray diffractometry. Then the magneto-elastic constants are calculated from the phenomenological relationship with the anisotropy constants measured by cavity FMR. For GaMnAs, this can be obtained by a comparison of Equations 3.6 to 1.15. The result is given as follows:

$$\begin{cases} B_2 = \frac{K_{2\parallel}}{2S_{xy,\,0}} \\ B_1 = \frac{-K_{2\perp}+K_{2\parallel}}{S_{zz,\,0}-\frac{S_{xx,\,0}+S_{yy,\,0}}{2}} \end{cases} \tag{3.7}$$

Zero in strain indices denotes the epitaxial static strain. To find the above relations we neglected $S_{yz,\,0}$ and $S_{zx,\,0}$ components ($S_{yz,\,0} = S_{zx,\,0} = 0$). For our GaMnAs sample magneto-elastic constants at T=60 K, are approximately $B_1 \cong 6.3 \times 10^6$ J/m^3, $B_2 \cong 2.3 \times 10^6$ J/m^3.

3.3. Effect of the magneto-elastic coupling on magnetization and strain dynamics

The acoustic and magnetic waves are coupled through the magneto-elastic energy. Therefore, both magnetization dynamics and the propagation of acoustic waves are modified by this interaction. Let us assume that a harmonic SAW is propagating on the surface of a half-space magnetostrictive material along the [100] direction. The equation of motion for the elastic medium 2.4 is expressed as the function of the elastic and magneto-elastic energy [14]:

$$\frac{\partial^2 \left(f_{el} + f_{Mel}\right)}{\partial x_k \partial S_{ik}} = \rho \frac{\partial^2 u_i}{\partial t^2} \tag{3.8}$$

We used this equation without magneto-elastic energy in the paragraph 2.4 to find the Rayleigh velocity (from this equation the dispersion relation for phonons can be computed, which for the Rayleigh waves is linear $\omega = V_R k$ [80]). For magnetostrictive samples the magneto-elastic energy needs to be added to the elastic contribution. Together with LLG equation 1.1, the SAW propagation equation forms a coupled system:

$$\begin{cases} \frac{\partial \vec{\boldsymbol{m}}}{\partial t} = -\mu_0 \gamma \vec{\boldsymbol{m}} \times \vec{\boldsymbol{H}}_{\boldsymbol{eff}} + \alpha \vec{\boldsymbol{m}} \times \frac{\partial \vec{\boldsymbol{m}}}{\partial t}, \quad \vec{\boldsymbol{H}}_{\boldsymbol{eff}} = -\frac{1}{\mu_0} \vec{\boldsymbol{\nabla}}_m \left(f_{el} + f_{Mel}\right) \\ \frac{\partial^2 (f_{el} + f_{Mel})}{\partial x_k \partial S_{ik}} = \rho \frac{\partial^2 u_i}{\partial t^2} \end{cases} \tag{3.9}$$

The magnetization can be written as $\vec{\boldsymbol{m}}_0 + \delta\vec{\boldsymbol{m}}(t)$. The system leads to 6 coupled equations for the $\delta\vec{\boldsymbol{m}}_i$ and u_i components (actually 4 since $|\vec{\boldsymbol{m}}| = 1$ and $u_y = 0$). First we neglect the backaction of the magnetization on the SAW amplitude. We obtain a usual magnetization precession equation with an effective driving RF field $h_{RF}(t)$ generated by the SAW and directed perpendicular to the static magnetization. In the case of a SAW propagating along $x//$ [1-10] and $\vec{\boldsymbol{m}}_0$ lying in-plane, $h_{RF}(t)$ has only an in-plane component, perpendicular to $\vec{\boldsymbol{m}}_0$, given by:

$$\mu_0 h_{RF}(t) = B_2 S_{xx}(t) \sin 2\varphi_0 \tag{3.10}$$

We made here the same assumption for the static strain components as in the previous paragraph. The SAW has $S_{xx}(t)$, $S_{zz}(t)$ and $S_{xy}(t)$ components. Only one of the magneto-elastic constants contribute to the driving field. The constant B_1 is more critical for the out-of-plane magnetized samples. The SAW propagation is modified through a change of the elastic constants. In the literature this change is known as *delta-E*-effect, where Young's modulus (E) is different for a magnetostrictive material, unsaturated (E_0) and saturated (E_s) with the magnetic field [81]. It

is expressed as the ratio $\Delta E = \frac{E_s - E_0}{E_0}$, with Young's modulus defined as the ratio of the applied stress and strain $E = \frac{\sigma}{S}$. Young's modulus is strongly correlated with the Rayleigh velocity, which can be used to determine it [82]. Applying boundary conditions for the semi-infinite medium to the solution of 3.9 yields the dispersion relation [14]:

$$\left(c_{44} - \rho\frac{\omega^2}{k^2}\right)\left(c'_{11}c_{11} - c_{12}^2 - c_{11}\rho\frac{\omega^2}{k^2}\right)^2 = c_{11}c_{44}\left(c'_{11} - \rho\frac{\omega^2}{k^2}\right)\rho^2\frac{\omega^4}{k^4} \tag{3.11}$$

where c'_{11} is the modified elastic constants due to the magnetostriction, defined as:

$$c'_{11} = \frac{1}{2}c_{11} + \frac{1}{2}c_{12} + c_{44} - M_s\chi_{22}\left(B_2 \sin 2\varphi_0\right)^2 \tag{3.12}$$

χ_{22} is the component of the susceptibility tensor. It depends on the SAW frequency and anisotropy constants. That is the biggest difference between Equation 3.11 and Equation 2.14 for non-magnetostrictive materials where the stiffness constants cannot be modulated by the SAW. For magnetostrictive materials with acoustic waves coupled to the magnetization, the dispersion relation is not linear anymore (Fig. 3.2). The acoustic wave velocities are not only a function of stiffness constants and mass density but also depend on the magnetic properties of the material. In the case of strong magneto-elastic coupling (high $\chi_{22}B_2$), the dispersion curve of phonons can avoid the crossing with the magnon dispersion curve at $\omega_{SW}(k_0) = \omega_R(k_0)$ for Rayleigh waves. Around k_0 the two modes are hybridized and then they can be considered as quasiphonons and quasimagnons. Away from the intersection point, the curves obey the ordinary dispersion relations so for $k \neq k_0$ we have pure magnons and phonons.

The interaction between SAWs and magnetization was studied before theoretically by many groups. The differences mainly rely on the assumed simplification of the system. Ganguly *et al.* and Feng *et al.* demonstrated the theory for the ferromagnetic film on a piezoelectric substrate [83, 84], while Camley and more recently Dreher *et al.* assumed the substrate to be non- piezoelectric [85, 13]. Moreover, those four groups did not consider the decay of the SAWs. Some of them simplified further the Rayleigh waves, *e.g.* Dreher *et al.* treated them as purely longitudinal waves and simplified their shape. The most complete studies were presented by Scott and Mills who took the full description of the SAWs into account[86].

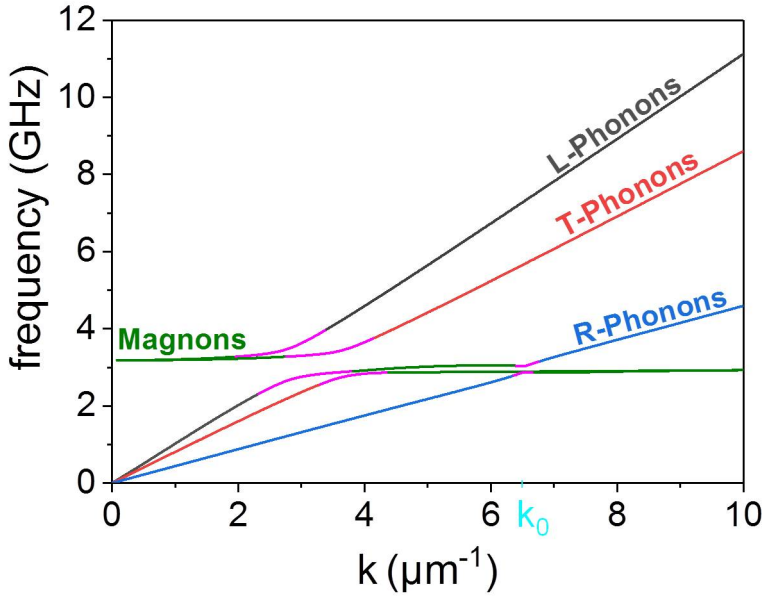

Figure 3.2.: Dispersion of longitudinal, transverse and Rayleigh acoustic waves in case of magneto-elastic interaction.

4. Static and dynamic control of the magnetization with strain: state of the art

Table of content

This paragraph is dedicated to the literature review on the use of strain to control magnetization. As it was carefully introduced in the previous chapters, magnetization can be controlled with static and dynamic strain. Static strain is mainly associated with the intentionally applied stress and with the lattice mismatch between a magnetic film and a substrate, while dynamic strain can be produced with acoustic waves.

4.1. Static strain

Static strain can be used to modify the magnetic properties of a ferromagnet, like an external magnetic field or temperature. In bulk samples, it was reported that a small stress (10 MPa) can strongly affect the hysteresis curves of Permalloy and Nickel [87]. The change of the hysteresis curve can be understood as a modification of the magnetic anisotropy. The used apparatus consisted of a few centimeters long wire of the investigated material hanging out vertically [88]. The upper end was mounted with the spring and the bottom end was loaded with the desired weight. For the thin films to which this work is dedicated, the strain is applied with more sophisticated methods. Strain can originate from the lattice mismatch between the layer and the substrate [89]. One of the best examples is GaMnAs, in which the magnetic anisotropy is very sensitive to the strain. It is magnetized in-plane when the sample is under compressive strain (Fig. 4.1 (a)). That is the case of epitaxially grown GaMnAs on a GaAs substrate. On the other hand, when GaMnAs is grown

on a substrate with a larger lattice constant (Fig. 4.1 (b)), such as InGaAs then it is under a tensile strain and the magnetization points out of plane [90]. This is possible, due to the magneto-elastic energy which can compensate the demagnetizing energy (Equation 3.6).

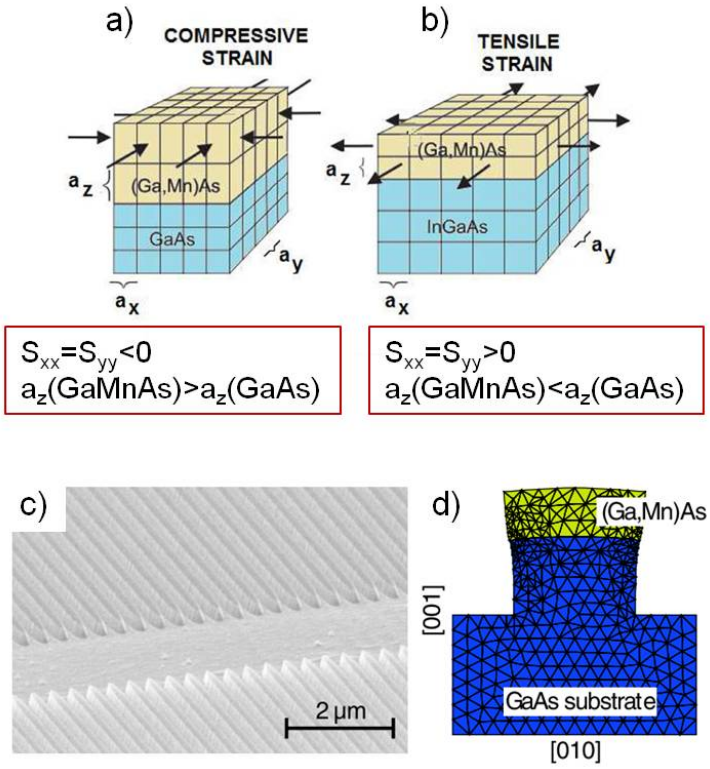

Figure 4.1.: Illustration of the effect of biaxial (a) compressive and (b) tensile strain on a GaMnAs film [91]. Picture of patterned GaMnAs surface (c) taken with scanning electron microscopy and (d) simulated displacement in the cross section in the one of the stripes [92].

The out-of-plane equilibrium position of the magnetization for GaMnAs, which is unusual for thin films, can be engineered also in other ways. Lemaitre and co-workers published a paper where instead of changing the buffer, the lattice constant of the magnetic layer was modified. An experimental demonstration was carried out for GaMnAs on a GaAs substrate with the incorporation of a small amount of Phosphorus (less than 10%). As a result, the samples had an easy axis shifting continuously from in-plane to out-of-plane with increasing Phosphorus [93]. Magnetic anisotropy can be also controlled with the use of lithography patterning. Wenisch *et al.* demonstrated an approach, where the sample surface of GaMnAs is patterned in 200 nm wide and 100 µm long stripes (Fig. 4.1 (c)). As a result strain is relaxed only in the direction perpendicular to the stripe long axis where edges are not bounded (Fig. 4.1 (d)). The easy axis will lay along the stripes, in this case along the [100] axis [92]. A similar experiment was performed by Wunderlich *et al.* They

demonstrated the elastic origin of the in-plane, uniaxial anisotropy. The anisotropy constant $K_{2\parallel}$ originates from the strain component S_{xy} [94]. Other approaches have been also demonstrated, where the easy axis is not permanently fixed to one position. In one of the methods, a strongly piezoelectric ceramic layer, Lead zirconate titanate (PZT), is attached to the thinned GaAs substrate [95, 96]. A micrometer Hall bar was patterned on the GaMnAs layer on GaAs in order to monitor the direction of the magnetization vector using anisotropic magnetoresistance measurements. Depending on the sign of DC electric voltage (+/- 150V) applied to the PZT, the layer it was either under tensile or compressive strain. As a result the easy axis was rotated in the sample plane by 50°.

Since the magneto-elastic energy contributes to the total energy of the ferromagnetic system, not only the magnetic anisotropy can be changed with static strain but also the FMR frequency [97]. This effect plays a crucial role in the interaction of dynamical stresses with magnetization.

4.2. Dynamic strain

Dynamical strain can be introduced easily with acoustic waves. Two types of acoustic waves can be distinguished: bulk and surface acoustic waves. Depending on the experimental requirements (such as frequency, strain components, configuration) one of them is chosen. However, both of them obey the same resonance condition, i.e. they interact the strongest with magnetization when their frequency and wavevector are equal to the spin wave frequency and wavevector, respectively. Since the magnon disspersion curve is very flat in the range of k-vectors available for acoustic waves resonance. This might be achieved by choosing the right frequency of the acoustic waves, or by modifying the FMR frequency *e.g.* with the magnetic field.

4.2.1. Non-resonant interaction

Naturally, the non-resonant conditions have been also studied by many research groups. In this case, strain is used to modify the sample anisotropy quasi statically, to lower the coercive field. Then the magnetization switching at low SAW frequency is possible with magnetic field applied along the easy axis. It was firstly reported by Davis *et al.*[15], who showed the magnetization rotation between in-plane easy and hard axes in 10 nm thick, Co bars (Fig. 4.3 (g)). With static Kerr magnetometry, they observed that the magnetization was pulled from easy to hard axis periodically, above certain strain powers, however irreversible switching was not shown. The work on magnetization switching with electrically excited SAWs was continued by Thevenard *et al.* who showed the magnetization switching for out-of-plane magnetized (Ga,Mn)(As,P) film [98]. They demonstrated a reduction of the coercive field by $\sim 50\%$ (9.8 $\rightarrow$ 4.3 mT) (Fig. 4.2 (a)). Subsequently, Dhagat *et al.* proposed the

concept of acoustically assisted magnetization switching for magnetic data storage [99]. For magnetization writing demonstration they used a floppy disc head and for reading another sensor, magnetoresistive hard disc drive head (Fig. 4.2 (c)). Planar IDTs were used to generate standing acoustic waves. This worked well, but for a single bit writing they proposed that each should have its own curved IDT, which will not provide high density data storage and seems to be far from commercial use. Two years later, Sampath *et al.* (2016) presented an interesting feature of non-resonant interactions [100]. They reported a switching of magnetic state from single domain to the nonvolatile vortex in elliptical cobalt nanomagnet (Fig. 4.2 (b)). After the propagation of SAWs with frequency of 3.4 MHz, the stable vortex state is obtained and it is a new local energy minimum. A large magnetic field (0.2 T) needs to be applied to bring it back to the initial single domain state. The magnetization can be driven again to the vortex state with the use of SAWs .

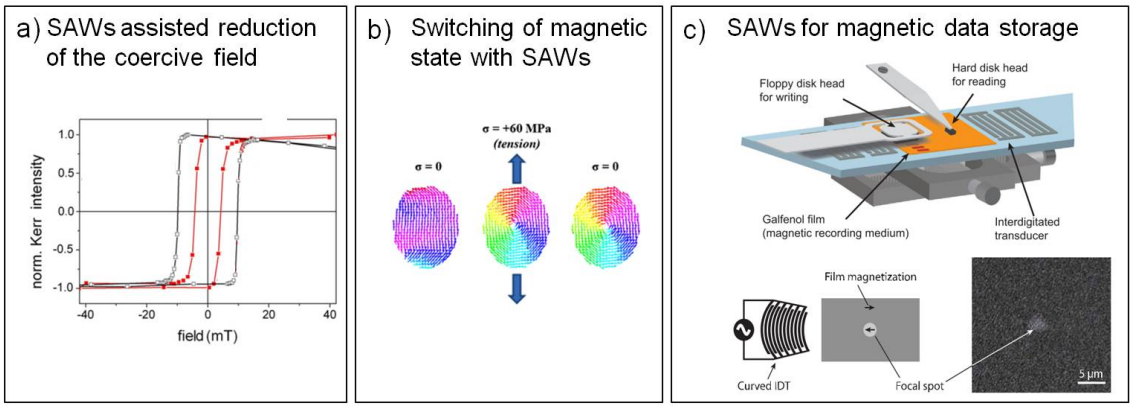

Figure 4.2.: a) Hysteresis cycles with and without SAW for GaMnAs [98]. b) Micromagnetic simulation of a nanomagnet state under the tensile dynamic strain [100]. c) Schematic of the device for magnetic data storage. Data will be recorded with the assistance of the SAW [99]

4.2.2. Resonant interaction

As shown above, the non-resonant conditions are mainly used for magnetization switching, contrary to the resonance conditions. The prime experimental evidence of resonant coupling was carried out with the use of bulk acoustic waves in 1959 for a 180 nm thick Nickel film on a Quartz substrate [101]. The sample was a 12 mm long and 3 mm thick rod, placed between two microwave cavities. The RF magnetic field acted on one of the ends of the sample (Fig. 4.3 (a)). A DC magnetic field was applied along the wire to tune the ferromagnetic resonance frequency in order to level it with RF, fixed at 1 GHz. When this constraint was fulfilled, the magnetization precession was induced and therefore shear dynamic strain due to the magnetostriction. This created electromagnetic waves due to the piezoelectricity of

Quartz, detected with the second cavity [102]. In the same article the authors showed that this process can be reversed, thus magnetization precession was generated with the dynamic strain resulting from the piezoelectricity. Soon the evidence of the magneto-elastic coupling was also reported by Pomerantz [103] who used a very similar set-up, except that he worked with Permalloy (80% of Ni and 20% of Fe) and frequency of around 9 GHz. This experiment attracted a lot of attention in the '60s since it was a cheap method to generate GHz ultrasonic waves.

The development of IDTs (§ 2.5.2) as an easy way for surface acoustic waves excitation made them attractive in the '70s. Soon after this discovery many theoretical papers treating the interaction of magnetization with SAWs came out [104, 105, 106, 107, 86, 83, 108, 85, 109]. The idea of the experimental investigation was rather simple. A set of two IDTs were used, one to excite SAWs and a second to detect them through the piezoelectric effect. Between the two IDTs, a ferromagnetic film was deposited on the surface of the piezoelectric substrate. Changes of SAW amplitude and velocity were measured as a function of magnetic field. The most used material was Nickel with a thickness between 20 and 200 nm (Fig. 4.3 (f)) [110, 111, 84, 109]. SAWs came to be known as a great tool for surface spin waves excitation [86]. For certain magnetic fields, narrow peaks in SAW attenuation and dips in SAW velocity were observed. To prove the magnetic origin of those changes many tests were performed. As one of the proofs susceptibility measurements were proposed [84]. These results showed similar resonance behavior. Moreover, it was found that the magnitude of SAW attenuation depends on the frequency of the SAW and the film thickness due to the resistivity losses [112].

The potential for magnetization switching renewed the interest into this experimental configuration in 2013. Thevenard *et al.* showed calculations evidencing that high amplitude SAWs with frequency below 1 GHz can lead to a large angle precession of magnetization. Magnetization can oscillate around the small bias field applied perpendicular to the easy axis [21, 16, 113]. They showed experimental results for in-plane and out-of-plane magnetized GaMnAs samples, where full magnetization reversal was reported. The efficiency of the switching is higher than 50%, which means that over half of magnetic domains changed their orientations after the passage of a SAW's burst. The resonant behavior of magnetization precession was then theoretically studied by three groups [13, 114, 14]. They showed that electrically excited and electrically detected SAWs can be a very powerful device to detect the FMR. For this purpose they discussed the backaction of magnetization on SAWs (Fig. 4.3 (h)). It is important to mention that in these three papers authors employed different assumptions for SAWs.

The SAW response to the magnetic field in case of propagation in magnetostrictive materials can be used as a magnetic field sensor where the changes of velocity are monitored [110]. If the IDT digits are made of a magnetostrictive material like Nickel, the SAWs resonance frequency will be also changed [115]. That makes the SAWs delay line configuration really interesting for commercial use.

Furthermore, transducers can be also used to excite BAWs. Polzikova *et al.* demonstrated BAWs as a great tool to study FMR, since the high acoustic frequency (1-4 GHz) can be easily excited and the requirements for the uniformity of magnetic field are lowered because of a small transducer aperture. The area can be reduced to the order of 0.03 mm^2 [116, 117, 118]. In the published papers authors presented the variation of the BAWs frequency and amplitude due to the magneto-elastic coupling in yttrium iron garnet (YIG) film.

4.2.2.1. Optical excitation of BAWs

The concept of excitation of magnetization precession using bulk acoustic waves was also studied using optically excited picosecond strain pulses [119, 120]. Up to 2013 a great number of articles came out where the authors used identical experimental schemes[121, 122, 123, 124, 125, 126]. The sample was composed of a ferromagnetic layer on a GaAs substrate with a thin Al metallic film on the back side. Femtosecond laser pulses arrive on the Aluminium layer to excite picosecond strain pulses propagating through the substrate to the magnetic layer. This is the pulsed magnetization excitation, since it is triggered by very short strain pulses. This configuration ensures that the high laser fluence does not influence in any way the magnetic layer due to the clear separation from the excitation place. With this technique, various types of acoustic waves can be excited: longitudinal, quasi-transverse and quasi-longitudinal, depending on the substrate: high (001) or low (311) symmetry GaAs. Strain pulses are a few tens of picosecond long, thus a broad acoustic spectrum is excited centered around 40 GHz [123]. A magnetic field is applied to the sample for tuning the spin wave frequency ($f_{prec}(B) \rightarrow f_{AW}$) (Fig. 4.3 (b)). To match the wavevectors, since the wavevector of acoustic wave cannot be tuned, it is the thickness of the magnetic layer that needs to be chosen adequately. Most articles are devoted to GaMnAs films [122, 123, 124, 127, 121] but results for Nickel [125] and Galfenol ($Fe_{81}Ga_{19}$) films [126] and theoretical studies of Terfanol-D [128] were also reported. The variation of magnetization was directly measured with the optical Kerr time resolved measurement (described in Section 5.2.2). The wavevector of the acoustic pulses is perpendicular to the film plane. That is why standing spin waves are excited in the transversely confined magnetic medium. For magnetic films thicker than 100 nm it was shown that modes higher than the fundamental one can be generated [126]. Another important feature of this method is that the acoustic pulse traveling in the sample can be reflected at the boundaries and thus after a round trip pulse interacts again with magnetization. Recently this was improved by the group of J.-Y. Bigot who used the total internal reflection phenomena to increase the power of the reflected pulse [129]. A free standing Nickel film was fabricated and by using the same strain pulses excitation technique, they observed that the single strain pulse can last for 12 bounces and substantially compensates the Gilbert damping. It was also reported that the inverse process can be used to generate specific BAW components. T. Parpiiev *et al.* demonstrated that the photo-excited spinwaves can

generate shear and longitudinal strain in spin-crossover materials [130].

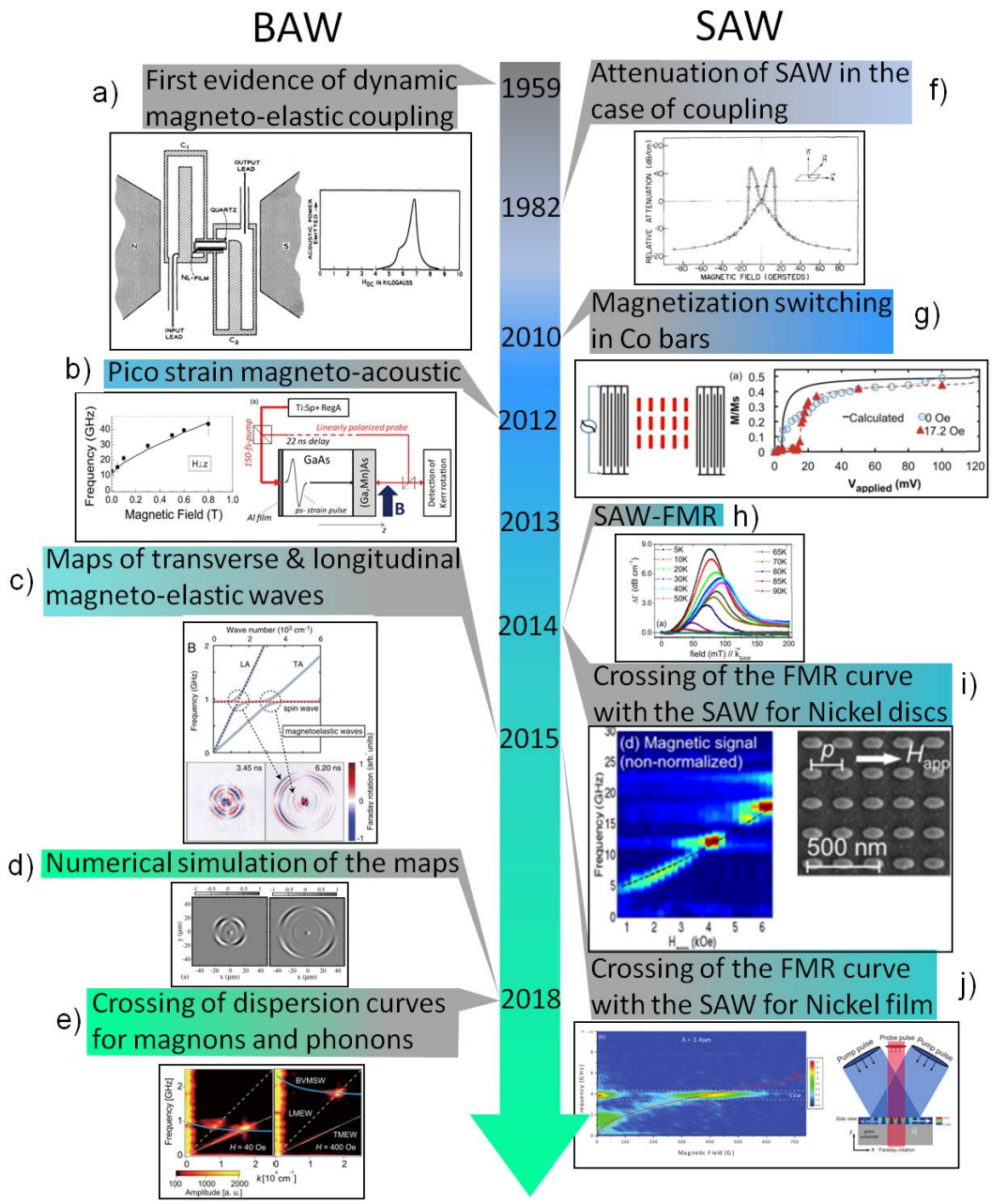

Figure 4.3.: Timeline with chosen magneto-elastic experiments. On the left side the experiment with used of BAWs are shown. First experiment was performed by Bommel in 1959 (a) [101]). Then the data obtained with optically excited pico strains (b) [123]) and interaction of BAWs with magnetization presented as space maps , c) [131], d) [132, 133] and dispersion curves: (e) [134]. The right side of the figure presents the results obtained for SAWs: excited electrically (f) [84], (g) [15], (h) [14], and optically (i) [135], (j) [67].

Later the experimental scheme evolved into the single side system where the sample was a thick magnetic layer on a transparent substrate. Bulk acoustic waves were excited with a tightly focused laser beam. The physical principle of this excitation may rely on the impulsive stimulated Raman scattering [136]. The first experiment was shown for a 50 µm thick Iron Garnet sample [131]. The efficient coupling of transverse and longitudinal bulk acoustic waves to the magnetization was demonstrated. The excited magnetization is considered as the hybrid magneto-elastic wave propagating with longitudinal and transverse sound velocity (Fig. 4.3 (c)). A very similar experiment was performed for 4 µm Bismuth doped Iron Garnet. The dispersion curves of the excited spin waves were shown for a few values of the DC magnetic field (Fig. 4.3 (e)) [134], using spin waves dispersion spectroscopy [137]. These results were also theoretically analyzed by Shen and Bauer (Fig. 4.3 (d)) [132, 133].

Despite all these articles, a remaining problem was the lack of direct time-resolved measurements of magnetization precession excited with SAWs. The signal detected in the IDT set-ups raised many questions and controversy about the origin of SAW attenuation and velocity change with field.. The theory developed among others by Dreher *et al.* and Thevenard *et al.* even if describing well SAW data needed to be also confronted to magnetic data.

4.2.2.2. Optical excitation of SAWs

To allay those doubts researchers headed towards optically excited SAW, since the implementation of optical time-resolved measurements with electrically excited SAWs was not trivial due to the synchronization of the laser pulses to the electrical signal. In this technique a laser pulse is split in two, one is used to generate SAW and the other to detected magnetization precession. In one of the first papers Janusonis *et al.* [67] used the transient grating technique to excite monochromatic 4 GHz SAWs on a Nickel film deposited on a MgO substrate (Fig. 4.3 (j)), with the Faraday rotation detection performed in the center of the excitation area. The magnetization precession was detected. Additionally, strain was monitored through the transient diffraction. The strongest magnetization precession signal occurred exactly at the intersection of the estimated FMR frequency curve with the SAW frequency. Moreover, the continuously tuned wavelength of the SAW gives the possibility to perform dispersion measurement. The dispersion of the SAW overlapped with the magnetization dispersion, which justified the origin of the magnetization precession. Later in the same experimental scheme, parametric magnetization excitation was shown including second harmonic generation [138].

Another approach for monochromatic SAW generation was proposed by Yahagi [135]. An array of Nickel elliptical thin discs on Silicon substrate was heated up with pump pulses (Fig. 4.3 (i)). The principle of SAW excitation is the same as for the transient grating, only here the spacing between the discs determined the wavelength of the excited SAW. This allows to excite SAWs of much smaller λ than

the transient grating technique. Changes in magnetization were probed with the magneto-optical Kerr effect and acoustic waves were probed using reflectivity. Similar features as in Janusonis' paper were observed: magnetization precession showed up when the FMR frequency coincides with the SAW frequency. Moreover, they compared the results with the one obtained for a non-patterned Nickel films and a film of Aluminium. For those samples, the modes correlated to SAWs disappeared.

Considering all these articles one part still missing is the unquestionable evidence of the magnetization precession excitation with electrically excited SAWs. This can be done only by employing one of the optical techniques for the time resolved detection. Another thing which has never been shown is the excitation of spin waves in tightly focused laser beam configuration for which SAWs will not be assigned to a unique wavevector. For this configuration only BAWs were used for magnetization excitation.

These two points will be addressed in this work. The experimental part of the thesis is divided into two sections. In one SAWs are excited with an IDT (Fig. 4.4 (a)) and in the second one they are excited optically with the tightly focused laser beam technique (Fig. 4.4 (b)). With the IDT we have studied magnetization precession excited in a GaMnAs film with 4 frequencies 151, 301, 452 and 603 MHz of SAWs with plane wavefront. The magnetic field was applied along a hard axis to match the FMR frequency with SAWs. The studies were performed for different powers of SAWs and for a few temperatures.

In contrast, for the optical approach, broadband circular SAWs were generated with a central frequency between 1 and 2.5 GHz depending on the substrate. The power of the SAWs could not be tuned as easily as with IDT. However, due to the simplicity of the implementation, we could test many specimens. The experiment was performed at room temperature. Therefore, the studied samples were ferromagnetic metals on transparent substrates. In both cases, magnetization precession was detected with use of the time- and space- resolved magneto-optical Kerr effect. In case of the electrically excited SAWs, the electrical detection of the SAW attenuation and phase change was also possible.

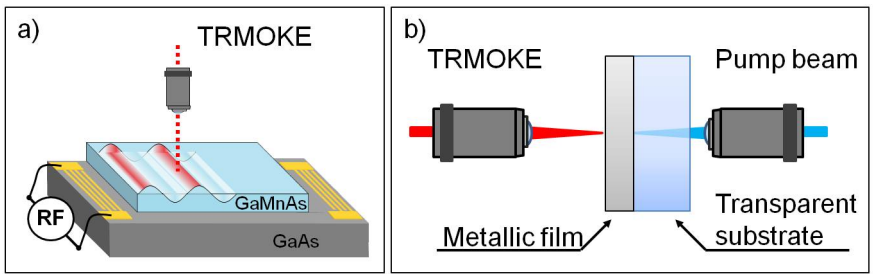

Figure 4.4.: Schemes of two experimental set-ups for SAWs generation: (a) electrically and (b) optically.

5. Experimental techniques

Table of content

The magnetic samples require a good characterization of magnetic properties to determine if they are suitable for a desired experiment. We need to know parameters such as the Curie temperature, the magnetization saturation, the magnetic anisotropy of the sample and, what is critical from the point of view of this work, the Ferromagnetic resonance (FMR) frequency dependence on the magnetic field. Here we describe the FMR techniques for the two group of samples used: cavity FMR (for ferromagnetic semiconductors) and broadband FMR (for ferromagnetic metals). Our experiment assumes the excitation of the magnetization precession in the range of a few hundreds of MHz to the GHz regime. In order to resolve dynamic changes of the magnetization, we used an optical technique (the Kerr magneto-optical effect), since it offers a great spatial resolution, which is important for the excitation of spin waves with the high frequency SAWs. In magneto-optical Kerr effect (MOKE), the rotation of polarization of the reflected light is detected and it is proportional to the magnetization. The measurement of polarization changes can be used not only to detect the magnetization precession but also SAWs through the photo-elastic effect as shown later in this chapter.

5.1. Magnetic characterization

Ferromagnetic resonance spectroscopy is a common technique to determine magnetic anisotropies in ferromagnetic samples. The working principle of the FMR measurement is the absorption of a radio frequency (RF) wave when the uniform magnetization precession mode is resonantly excited (Equation 1.17) by the magnetic component of a linearly polarized microwave field h_{RF}. The excitation is the most efficient when the frequency of h_{RF} is equal to the frequency of the uniform mode. To match the two frequencies, there exist two approaches: in one the frequency of h_{RF} is held constant and the FMR frequency is tuned with a DC magnetic field and in the second the magnetic field is fixed and the h_{RF} frequency is scanned in a broad range.

5.1.1. Cavity FMR

In cavity FMR, the sample is placed in a microwave cavity between magnetic poles. The frequency of the microwave usually around 9.4 GHz is set by the geometry of the cavity. The microwave frequency cannot be too low (>1 GHz), because the wavelength is defined by the size. If the wavelength is too large, this leads to an increase in the spacing between the poles that might lower the uniformity of the field.

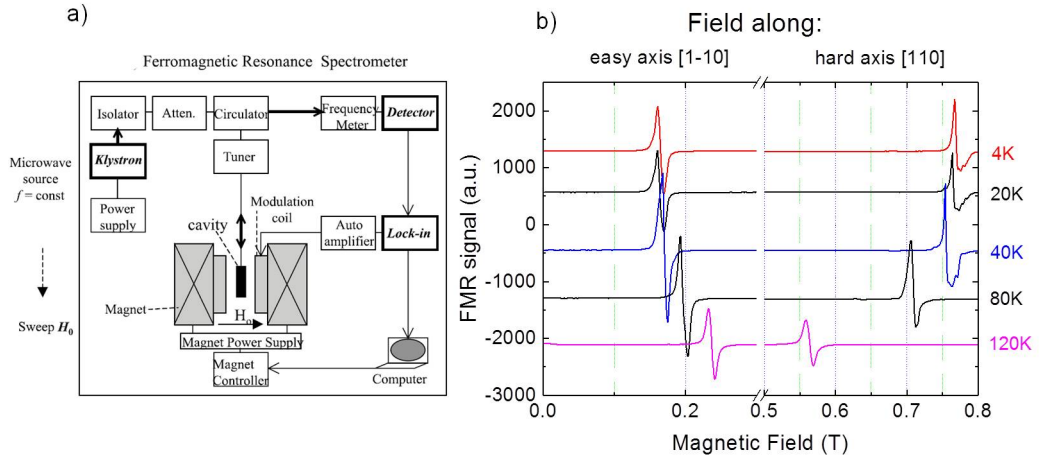

Figure 5.1.: (a) Simplified scheme of the FMR spectrometer [139] and (b) results of cavity FMR measurements for GaMnAs with the field applied along easy and hard axis (sample 4EQ64-r2).

The power of microwave reflected from the cavity is detected by the microwave diode. The signal on the diode is measured as a function of DC magnetic field. The detection sensitivity is increased by modulating the DC magnetic field at a low

frequency of a few hundreds of Hz (Fig. 5.1 (a)). To find the in-plane anisotropy of the sample, the magnetic field is applied at different angles in the sample plane. The sample is rotated around the normal to the plane. The out-of-plane anisotropy is investigated by applying the magnetic field along different directions from the normal to the film to the film plane.

Typical curves of cavity FMR measurements are presented in Fig. 5.1 (b), here for GaMnAs. These data were taken by Jürgen Von Bardeleben and Teyri Amarouche in INSP. The field was applied along the easy and hard axes for a few temperatures. We can see that the field needed to match the two frequencies is lower for the easy axis. The in-plane anisotropy constants: $K_{2\parallel}$ and $K_{4\parallel}$ of the GaMnAs sample were found, by performing the cavity FMR measurements for more DC magnetic field orientations and then by fitting the found FMR fields with Equation 1.15. The linewidth also inform us about the sample homogeneity.

Although FMR can also be used to measure the magnetization $M_s(T)$ [140], after calibration by a sample with know $M_s(T)$, we have instead used a more convenient technique, the vibrating sample magnetometer (VSM) to measure $M_s(T)$.

The FMR technique provides great sensitivity since the sample is placed in the cavity. Moreover, the sample can be measured at low temperature. For samples that do not require low temperature measurement we rather use the broad-band FMR technique recently developed in our group

5.1.2. Broadband FMR (BBFMR)

In BBFMR, the sample is placed on a coplanar waveguide [141]. This is a transmission line consisting of three metallic planar electrodes running parallel to each other on a dielectric slab. The central line is the conductive line, with two ground lines on both sides separated by air. The RF electric current I_{RF} creates the RF magnetic field $\mu_0 h_{RF} \cong \mu_0 \frac{I_{RF}}{w}$ (w is the width of the conducting line) around the line [142].

This can excite the magnetization precession in the sample and as a result of the time varying magnetic flux a micro-voltage is created in the transmission line [144]. To monitor this effect, changes of the impedance are measured. Since the measured changes are small and need to be measured at high frequency (>1 GHz), a Vector Network Analyzer (VNA) is used. It measures the transmission and reflection of electromagnetic waves, which are described by scattering parameters:

$$S = \begin{pmatrix} S_{11} & S_{12} \\ S_{21} & S_{22} \end{pmatrix} \tag{5.1}$$

S_{11} and S_{22} are the reflection parameters, and S_{12}, S_{21} are the transmission parameters. We have mainly worked with the transmission parameter (S_{12}), which can be

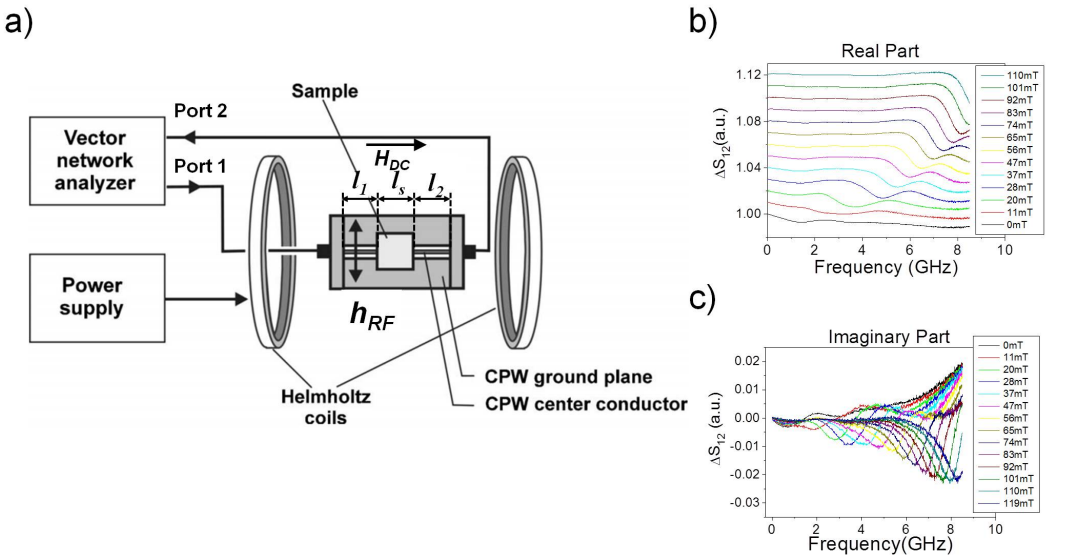

Figure 5.2.: (a) Schematic of the set-up for Broadband FMR measurement [143]. In (b) and (c) are presented the real and imaginary component of the scattering parameter ΔS_{12} for a 100 nm thick Nickel film. The power of I_{RF} was 0 dBm.

expressed as [145]:

$$S_{12} = e^{-\gamma_0(l_1+l_2)} \frac{P\,(1-\Gamma^2)}{1-P^2\Gamma^2} \tag{5.2}$$

where $P = e^{-\gamma l_s}$, $l_1 + l_2$ is the total length of the part of the waveguide not occupied part by the sample (Fig. 5.2 (a)). The sample length is l_s. Γ is the impedance ratio: $\Gamma = \frac{Z-Z_0}{Z+Z_0}$, it is equal to zero when the sample is not loaded, otherwise the waveguide impedance is modified from Z_0 to Z and the propagation constant (γ_0 without sample) becomes γ.

In the experiment, the sample lies with the magnetic layer side down onto the waveguide, which is placed between the poles of a magnet. Two ports of the waveguide are connected with SMA (SubMiniature version A) coaxial cables to the VNA. The h_{RF} field is scanned from 300 kHz to 8 GHz (maximal frequency range of Rohde-Schwarz ZVA8 Vector Network Analyzer) for a chosen static magnetic field value. The impedance mismatch between the waveguide and the 50 Ω cables and VNA can give rise to a S_{12} parameter. That is why it needs to be calibrated when the sample is not positioned on the waveguide. The measured calibrated $\Delta S_{12} = \frac{S_{12}}{S_{12}(ref)}$ parameter has real and imaginary components, which correspond to the magnetic susceptibility[145]. From the measured curves $\Re\Delta S_{12}(B)$ and $\Im\Delta S_{12}(B)$ we can obtain the dependence of the FMR frequency on the magnetic field. On some samples (usually thicker than 100 nm) we can easily fallow the dependence of the resonance frequency with the applied field down to low field values < 20 mT (Fig. 5.2 (b) and

(c)). For thin samples or some of the FeGa samples, the poor quality of the signal makes it difficult to determine the resonance frequency at low field. The BBFMR was developed for INSP by I.S. Camara to characterize ferromagnetic metals. With the established set-up we can measure the samples only at room temperature, that is why it was not used for the ferromagnetic semiconductors.

5.1.3. Vibrating-sample magnetometer (VSM)

VSM is a technique to measure the sample magnetization. The first VSM device was built and used in 1959 by Simon Foner [146]. The working principle is based on the Faraday induction law. The sample is mounted on a rod, vibrating in a constant and uniform magnetic field. The alternating flux induces a voltage in the pick-up coils, which is directly proportional to the magnetization. Varying the external magnetic field, a full hysteresis cycle can be obtained. In VSM devices equipped with cryogenic temperature control, the $M_s(T)$ dependence can be measured. We used this technique to measured $M_s(T)$ of GaMnAs and to obtain the anisotropy constants from cavity FMR and f_{FMR}(B) dependence (Equation 1.15 and 1.18).

5.2. Time and frequency domain detection of spin waves

5.2.1. Faraday effect

Magneto-optical effects illustrate the interaction of light with matter, where the polarization of light can be affected by the magnetic medium. One of these effects was discovered by Michael Faraday in 1845 [147]. He observed that the plane of linearly polarized light is rotated upon propagation in a dielectric medium under an externally applied magnetic field (Fig. 5.3).

A similar effect, but for reflection of light from a magnetic medium was found 30 years later by J. Kerr. Those two effects were named after their discoverer. The observed rotation of light polarization is due to magnetic circular birefringence and dichroism. The material has two different refractive indices for left and right circularly polarized light. Let us consider linear polarized light propagating in the Faraday configuration *i.e.* with the $\vec{\boldsymbol{k}}$ vector along the magnetic field or the magnetization. It can be written as the combination of left and right circularly polarized light. The ($\sigma\pm$) circularly polarized light propagating along the z axis is written as follows:

$$\vec{\boldsymbol{E}} = E_0 \left(\vec{\boldsymbol{e}_x} + \vec{\boldsymbol{e}_y} e^{\pm i \frac{\pi}{2}} \right) e^{i(kz - \omega t)} \tag{5.3}$$

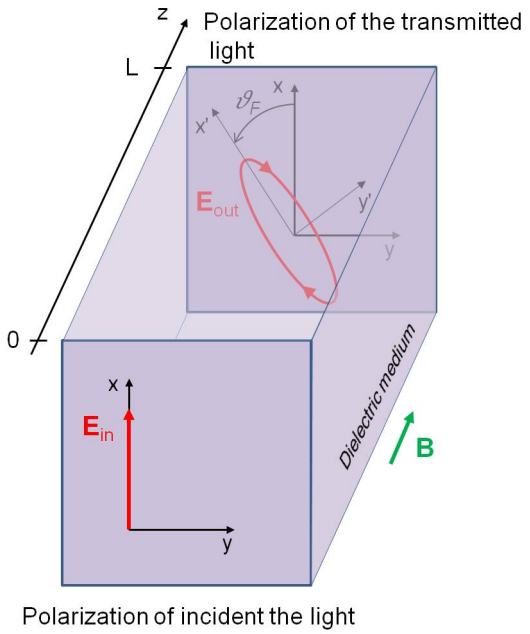

Figure 5.3.: Illustration of the Faraday effect. The state of the polarization of the incident beam is changed upon propagation in a magneto-optical medium.

The plus (minus) is for left (right) circularly polarized light. The polarization associated with the electric field vector rotating anticlockwise is called left circular. Let us assume the incident light polarization along $\vec{\boldsymbol{x}}$. A linear polarization can be decomposed into the sum of a right and left circularly polarized light. The $\vec{\boldsymbol{E}}$ vector of light propagating in the sample can then be written as:

$$\vec{\boldsymbol{E}} = \frac{1}{2}E_0\left(\vec{\boldsymbol{e}_x} + i\vec{\boldsymbol{e}_y}\right)e^{i\left(\frac{2\pi n_+}{\lambda}z-\omega t\right)} + \frac{1}{2}E_0\left(\vec{\boldsymbol{e}_x} - i\vec{\boldsymbol{e}_y}\right)e^{i\left(\frac{2\pi n_-}{\lambda}z-\omega t\right)} \tag{5.4}$$

where n_+ and n_- are the refractive indices for left and right polarized light and λ is the light wavelength in the vacuum. The above equations after some trigonometrical treatment can be presented in the following form [148, 149]:

$$\vec{\boldsymbol{E}} = E_0 e^{i\left(\frac{2\pi\bar{n}}{\lambda}z-\omega t\right)}\left(\vec{\boldsymbol{e}_x}\cos\frac{\delta}{2} - \vec{\boldsymbol{e}_y}\sin\frac{\delta}{2}\right) \tag{5.5}$$

where $\bar{n} = \frac{1}{2}\left(n_+ + n_-\right)$ and $\delta = 2\pi\left(\frac{n_+ - n_-}{\lambda}\right)z$. From this we can immediately see that the linearly polarized light will be rotated due to to the propagation in the circular birefringence medium. The angle of Faraday rotation depends on the optical path and is simply given as:

$$\vartheta_F = \frac{\delta}{2} = \pi\left(\frac{n_+ - n_-}{\lambda}\right)L \tag{5.6}$$

where L is the length of the dielectric medium. For a transparent, paramagnetic material the Faraday rotation angle is directly proportional to the applied magnetic field. To define the indices n_+ and n_- we need to employ Maxwell equations:

$$\vec{\boldsymbol{\nabla}} \times \vec{\boldsymbol{E}} = -\frac{\partial \vec{\boldsymbol{B}}}{\partial t} \qquad \text{Faraday's law of induction} \tag{5.7}$$

$$\vec{\boldsymbol{\nabla}} \times \vec{\boldsymbol{B}} = \mu_0 \epsilon_0 \frac{\partial \vec{\boldsymbol{E}}}{\partial t} + \mu_0 \vec{\boldsymbol{J}} \qquad \text{Ampere's law} \tag{5.8}$$

$$\vec{\boldsymbol{\nabla}} \cdot \vec{\boldsymbol{E}} = \frac{\rho}{\epsilon_0} \qquad \text{Gauss's law} \tag{5.9}$$

$$\vec{\boldsymbol{\nabla}} \cdot \vec{\boldsymbol{B}} = 0 \qquad \text{Gauss's law for magnetism} \tag{5.10}$$

$\vec{\boldsymbol{J}}$ is the current density and ρ is the charge density. The current density is given as: $\vec{\boldsymbol{J}} = \frac{\partial \vec{\boldsymbol{P}}}{\partial t} + \vec{\boldsymbol{\nabla}} \times \vec{\boldsymbol{M}}$, $\vec{\boldsymbol{P}}$ is the electric polarization which for a linear materials has a linear dependence on the electric field. Inserting this formula into Ampere's law (Equation 5.8) we get:

$$\vec{\boldsymbol{\nabla}} \times \vec{\boldsymbol{H}} = \frac{\partial \vec{\boldsymbol{D}}}{\partial t}, \tag{5.11}$$

where $\mu_0 \vec{\boldsymbol{H}} = \vec{\boldsymbol{B}} - \mu_0 \vec{\boldsymbol{M}}$ and the electric displacement $\vec{\boldsymbol{D}} = \epsilon_0 \vec{\boldsymbol{E}} + \vec{\boldsymbol{P}} = \epsilon_0 \epsilon_r \vec{\boldsymbol{E}}$, ϵ_r is the relative dielectric tensor. Now, combining 5.11 with Faraday's induction law (Equation 5.7) and assuming that $\vec{\boldsymbol{M}}$ varies slowly as compared to the period of light, we will get:

$$\nabla^2 \vec{\boldsymbol{E}} - \nabla \left(\nabla \cdot \vec{\boldsymbol{E}} \right) = \mu_0 \epsilon_0 \epsilon_r \frac{\partial^2 \vec{\boldsymbol{E}}}{\partial t^2} \tag{5.12}$$

Looking for plane wave solutions, we obtained:

$$n^2 \vec{\boldsymbol{E}} - \vec{\boldsymbol{n}} \left(\vec{\boldsymbol{n}} \cdot \vec{\boldsymbol{E}} \right) = \epsilon_r \vec{\boldsymbol{E}} \tag{5.13}$$

where $\vec{\boldsymbol{n}} = \vec{\boldsymbol{k}}\frac{c}{\omega}$ is the complex refractive index (the light phase velocity in the material is lowered by the factor n with respect to the vacuum). Since light is a transverse wave ($\vec{\boldsymbol{k}} \perp \vec{\boldsymbol{E}}$) the equation above is simplified to:

$$n^2\vec{\boldsymbol{E}} = \epsilon_r\vec{\boldsymbol{E}} \tag{5.14}$$

For cubic crystals [78] (p24):

$$\epsilon_r = \epsilon \begin{pmatrix} 1 & -iQm_z & iQm_y \\ iQm_z & 1 & -iQm_x \\ -iQm_y & iQm_x & 1 \end{pmatrix} \tag{5.15}$$

Q is the Voigt constant which is proportional to the magnetization M_s existing or induced by the field. The dielectric tensor is related to the electronic transitions from the valence band [150]. The transition excited with left and right circular polarization makes m-electron (m is the magnetic quantum number) obey a different selection rule $\Delta m = +1$ for left and $\Delta m = -1$ for right helicity of photon. In our case the magnetization $\vec{\boldsymbol{m}} \parallel z$ ($m_z = 1$), then ϵ_r is given as:

$$\epsilon_r = \epsilon \begin{pmatrix} 1 & -iQ & 0 \\ iQ & 1 & 0 \\ 0 & 0 & 1 \end{pmatrix} \tag{5.16}$$

Then from Equation 5.14 the refractive indices are:

$$n_{\pm}^2 = \epsilon(1 \pm Q) \tag{5.17}$$

The eigenmodes are $\vec{\boldsymbol{E}}_0 = E_0\left(\vec{\boldsymbol{e}}_{\boldsymbol{x}} \pm i\vec{\boldsymbol{e}}_{\boldsymbol{y}}\right)$, which are the left and right circular polarizations of light. The Faraday angle can now be explicitly defined:

$$\vartheta_F = \pi\frac{L}{\lambda}\Re\left[\sqrt{\epsilon}Q\right] \tag{5.18}$$

Here we assumed that Q is small (~ 0.03 [78]), thus $n_{\pm} = n_0(1 \pm \frac{Q}{2})$, where $n_0 = \sqrt{\epsilon}$. When linearly polarized light passes through a magnetic medium not only its polarization plane undergoes a rotation, but it also becomes slightly elliptical. The ellipticity is related to $\Im\left[\sqrt{\epsilon}Q\right]$, that is to magnetic circular dichroism. The typical value of Faraday rotation for Ni and Co is 35 deg/µm (data for $\lambda = 830$ nm) [151], for GaMnAs the value is around 6 deg/µm(data for $\lambda = 800$ nm) [152].

5.2.2. Magneto-optical Kerr effect

In magneto-optical Kerr effect (MOKE), which is the effect we use in this work, three different configurations to probe three perpendicular magnetization components can be distinguished (Fig. 5.4). In the polar Kerr (PMOKE) configuration, the component perpendicular to the sample plane is probed. Longitudinal and transverse Kerr effects are sensitive to the in plane magnetization components: respectively parallel and transverse to the light incidence plane.

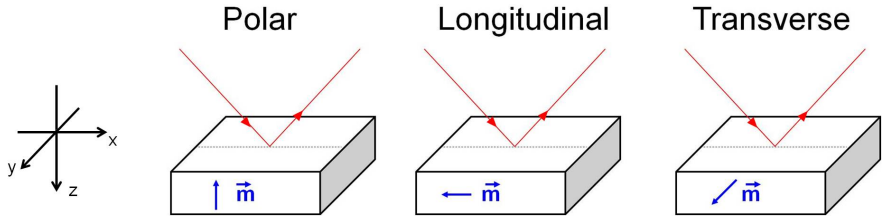

Figure 5.4.: Three configurations of MOKE.

Here we will take a closer look at PMOKE. The linearly polarized light arrives perpendicular to the vacuum/ferromagnet interface. The amplitude of the reflected beam is described by the Fresnel coefficients. As it was discussed in the previous paragraph, it is convenient to decompose the linear polarization into right and left circular polarizations since those two have different refraction indices. The ratio between the reflected $\left(\vec{\boldsymbol{E}}_R\right)$ and incident $\left(\vec{\boldsymbol{E}}_I\right)$ light is given by [149, 153]:

$$r = \frac{E_R}{E_I} = -\frac{n-1}{n+1} \tag{5.19}$$

For us E_R is the sum of left and right circular polarization of light (Equation 5.4), with n_+ and n_- respectively. Hence, if the incident beam is defined as 5.4, the reflected wave is given as:

$$\vec{\boldsymbol{E}}_R = \frac{1}{2}E_I \begin{pmatrix} -\frac{n_+-1}{n_++1} - \frac{n_--1}{n_-+1} \\ i\left[-\frac{n_+-1}{n_++1} + \frac{n_--1}{n_-+1}\right] \end{pmatrix} \begin{pmatrix} \vec{\boldsymbol{e}}_x \\ \vec{\boldsymbol{e}}_y \end{pmatrix} e^{i\left(-\frac{2\pi}{\lambda}z-\omega t\right)} \approx E_I \begin{pmatrix} -\frac{n_0-1}{n_0+1} \\ -i\frac{n_0 Q}{(n_0+1)^2} \end{pmatrix} \begin{pmatrix} \vec{\boldsymbol{e}}_x \\ \vec{\boldsymbol{e}}_y \end{pmatrix} e^{i\left(-\frac{2\pi}{\lambda}z-\omega t\right)} \tag{5.20}$$

The polarization of the reflected beam will be rotated and additionally the state of polarization will be changed. To see it clearly we can define the ratio r between the two orthogonal polarization components:

$$r = \frac{E_y}{E_x} \tag{5.21}$$

The rotation of the major axis of the ellipse is due to the phase difference of the two reflected circular components and this is related to the magnetic circular dichroism, thus for a semi-infinite material:

$$\vartheta_K = \Re\left[r\right] = \Re\left[i\frac{n_0 Q}{n_0^2 - 1}m_z\right] \tag{5.22}$$

The ellipticity results from the inequality of the amplitude of the two reflecte circular polarization components. This is related to the magnetic circular birefringence and we have:

$$\psi_K = \Im\left[r\right] = \Im\left[i\frac{n_0 Q}{n_0^2 - 1}m_z\right] \tag{5.23}$$

The m_z component was added at the end to stress again the magnetization dependence of the two. In this work we used static MOKE to characterize the magnetic hysteresis cycle of the samples (Fig. 5.10) and the time-resolved MOKE (TRMOKE) to study magnetization dynamics. For most magnetic materials, the Kerr rotation angle is of the order of magnitude $0.1 - 1$ deg [154].

5.2.3. Voigt effect

In the case of perpendicular orientation of the light wavevector with respect to the magnetization direction, two secondary effects have to be considered: magnetic linear birefringence (MLB) and magnetic linear dichroism (MLD) called together as Voigt effect. Let us analyze the situation where light arrives normal to sample surface. We assume that the sample is in-plane magnetized since, this applies to the majority of thin films as it was discussed in the first chapter. For cubic crystals the dielectric tensor can be expanded up to quadratic terms in the components of $\vec{\boldsymbol{m}}$ in the following form [78]:

$$\epsilon_r = \epsilon \begin{pmatrix} 1 & -iQm_z & iQm_y \\ iQm_z & 1 & -iQm_x \\ -iQm_y & iQm_x & 1 \end{pmatrix} + \begin{pmatrix} W_1 m_x^2 & W_2 m_x m_y & W_2 m_x m_z \\ W_2 m_x m_y & W_1 m_y^2 & W_2 m_y m_z \\ W_2 m_x m_z & W_2 m_y m_z & W_1 m_z^2 \end{pmatrix} \tag{5.24}$$

where W_1 and W_2 are the quadratic Voigt constants. For an isotropic material $W_1 = W_2$ and since there is no experimental evidence that $W_1 \neq W_2$ in GaMnAs,

we will keep the isotropic approximation, as in [155]. Furthermore, assuming that the sample is magnetized along the x axis, eq. 5.24 will be simplified to:

$$\epsilon_r = \begin{pmatrix} \epsilon + W_1 m_x^2 & 0 & 0 \\ 0 & \epsilon & -iQ\epsilon m_x \\ 0 & iQ\epsilon m_x & \epsilon \end{pmatrix} \tag{5.25}$$

The eigenmodes of light are now linearly polarized along $\vec{\boldsymbol{m}}$ and perpendicular to it. The two reflective indices are:

$$n_{\parallel}^2 = n_x^2 = \epsilon + W_1 \tag{5.26}$$

$$n_{\perp}^2 = n_y^2 = \epsilon(1 - Q^2) \tag{5.27}$$

This makes the polarization rotate. Since the refraction indices are complex numbers the two eigenvalues of polarization will be differently absorbed and it will lead to a change of the orientation of the polarization plane. The polarization rotation of the reflected light beam depends on the orientation of the incidence polarization plane with respect to magnetization. If we consider magnetization at angle φ_0 with the reference axis x (Fig. 5.5) and an incident beam with linear polarization at angle β with respect to the x-axis, we can write:

$$E_I = E_0 \begin{pmatrix} \cos(\beta - \varphi_0) \\ \sin(\beta - \varphi_0) \end{pmatrix} \tag{5.28}$$

in the reference frame ($\vec{x}' \vec{\boldsymbol{m}}$, $\vec{y}' \perp \vec{\boldsymbol{m}}$)

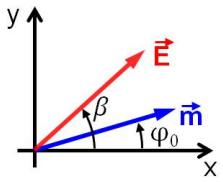

Figure 5.5.: The Voigt configuration for the polarization rotation

Then the electric field of the reflected beam is defined as:

$$E_R = E_0 \begin{pmatrix} -\frac{n_{\parallel}-1}{n_{\parallel}+1} \cos(\beta - \varphi_0) \\ -\frac{n_{\perp}-1}{n_{\perp}+1} \sin(\beta - \varphi_0) \end{pmatrix} \tag{5.29}$$

Projection on the vectors ($\vec{\boldsymbol{e}}_{\parallel}$, $\vec{\boldsymbol{e}}_{\perp}$), $\vec{\boldsymbol{e}}_{\parallel}$ being the unit vector along the incident polarization $\vec{\boldsymbol{E}}$, gives:

$$E_R = E_0 \begin{pmatrix} -\frac{n_{\parallel}-1}{n_{\parallel}+1}\cos^2(\beta-\varphi_0) - \frac{n_{\perp}-1}{n_{\perp}+1}\sin^2(\beta-\varphi_0) \\ \sin(\beta-\varphi_0)\cos(\beta-\varphi_0)\left(\frac{n_{\parallel}-1}{n_{\parallel}+1} - \frac{n_{\perp}-1}{n_{\perp}+1}\right) \end{pmatrix} \tag{5.30}$$

As it was for the Kerr rotation, the ratio between the two polarization components $r = \frac{E_{\perp}}{E_{\parallel}}$ will give the rotation of the polarization angle:

$$\Delta\beta = \frac{\left(n_{\parallel} - n_{\perp}\right)\sin 2(\beta-\varphi_0)}{n_{\perp}n_{\parallel} - 1 + \left(n_{\parallel} - n_{\perp}\right)\cos 2(\beta-\varphi_0)} \tag{5.31}$$

Assuming small polarization rotation angle ($\frac{n_{\parallel}}{n_{\perp}} \approx 1$), the formula 5.31 can be written in more general form:

$$\Delta\beta \approx \frac{n_{\parallel} - n_{\perp}}{n_{\perp}n_{\parallel} - 1}\sin 2(\beta-\varphi_0) = \frac{1}{2}\frac{\frac{W_1}{\epsilon} + Q^2}{n_0^2 - 1}\sin 2(\beta-\varphi_0), \tag{5.32}$$

We define the complex number $V = \Re\left[\frac{1}{2}\frac{\frac{W_1}{\epsilon}+Q^2}{n_0^2-1}\right] + i\Im\left[\frac{1}{2}\frac{\frac{W_1}{\epsilon}+Q^2}{n_0^2-1}\right]$. The real part determines the Voigt polarization rotation and the imaginary part the ellipticity. The Voigt effect is maximized for the incoming polarization oriented at 45 *deg* to the static magnetization. The polarization rotation due to the Voigt effect is usually much smaller than the one due to the PMOKE (if $W \ll Q^2$ then the Voigt effect is proportional to Q^2 which is much smaller then Q since $Q \ll 1$). However, the Voigt and Kerr effects depend on the light wavelenght have strong dependence on λ, which may be chosen to maximize or to minimize one of them. It was shown that for GaMnAs, the ratio between the two effects can be modified by the factor of 10 by changing the wavelength [156]. For ferromagnetic metals the λ-dependence is very small [157].

5.2.4. Brillouin light scattering spectroscopy (BLSS)

BLSS is a different approach to detect spin waves. A photon with energy $\hbar\omega_I$ of the probing beam is inelastically scattered by a magnon of energy $\hbar\omega_m$ (Fig. 5.6 (a)). As a result of energy and momentum conservation, one has [158]:

$$\hbar\omega_S = \hbar(\omega_I \pm \omega_m) \tag{5.33}$$

$$\hbar\vec{k}_S = \hbar\left(\vec{k}_I \pm \vec{k}_m\right) \tag{5.34}$$

the energy of the scattered photon is increased (+ sign) or decreased (- sign), depending on whether a magnon is annihilated or created. The probability of the two processes depends on the temperature when only thermal magnons are present. Using BLSS one can also probe coherent magnons, *i.e.* magnons excited by an antenna. From the point of view of classical physics, it can be understood as the refraction of the light on a moving phase grating, induced by the spin wave. Then the Doppler shift of the frequency will correspond to the frequency of the spin wave [159].

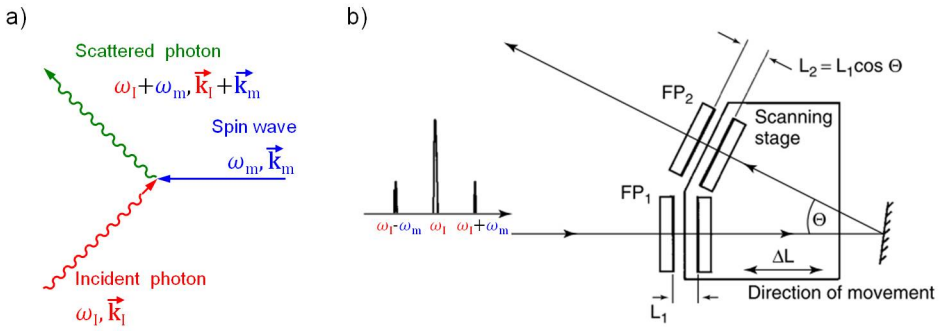

Figure 5.6.: (a) Diagram of one of the two scattering processes. (b) The working principle of a tandem Fabry-Perot interferometer [159].

By detecting the scattered photons one can directly measure the frequency of the spin waves. This light frequency change is commonly detected with the use of a tandem Fabry-Perot interferometer which can spectrally filter the light scattered from the sample (only the light whose wavelength fulfills the constructive interferometry condition is transmitted) (Fig. 5.6 (b)).

One advantage of BLSS is that it can provide in plane wave-vector resolution by changing the incidence angle of light. Therefore the spin wave dispersion curve can be measured. This is also possible with scanning TRMOKE.

The biggest difference between these two is that BLSS is a frequency domain technique while TRMOKE is measured in the time domain. However, with BLSS one can also perform time domain studies but only for a one chosen, fixed frequency[160]. Recently microfocused BLSS with the spatial resolution of the order of 1 μm was used to study spin waves in patterned ferromagnetic materials. In that case the wavevector resolution is partially lost.

The frequency reachable with BLSS is in the range of 0.2 GHz - 1 THz [159], which covers the spectrum of spinwaves for ferromagnetic materials (a few GHz) but not for antiferromagnetic materials (usually >1 THz). Moreover, it can be used to

detect acoustic waves by playing with excitation/detection light polarization [161], *e.g.* it was used to measure the frequency of the surface acoustic waves in a 1 µm thin optical fiber [162]. BLSS is generally a good choice to study propagating spin waves modes, while TRMOKE is an excellent technique to investigate the uniform spinwave mode. In this work we used the later method, since it is devoted to the uniform mode.

5.3. Detection of Surface acoustic waves - Photo-elastic effect

In paragraph 5.2 we showed that the magnetic order in the materials can lead to birefringence, which might be detected as a change of a polarization of the reflected light beam. We will show here that birefringence can also originate from strain. In this case, the variation of the permittivity tensor due to strain can be expressed as follows [63]:

$$\Delta\varepsilon_{il} = -\varepsilon_{ij} P_{jkmn} \varepsilon_{kl} \frac{\partial u_m}{\partial x_n}, \tag{5.35}$$

where P_{jkmn} is the elasto-optic tensor with values ranging from 0.1-0.3. For an isotropic medium it is given as:

$$\Delta\varepsilon = -\varepsilon^2 \begin{pmatrix} P_{11}S_{xx} + P_{12}\left(S_{yy}+S_{zz}\right) & \left(P_{11}-P_{12}\right)S_{xy} & \left(P_{11}-P_{12}\right)S_{xz} \\ \left(P_{11}-P_{12}\right)S_{xy} & P_{11}S_{yy} + P_{12}\left(S_{xx}+S_{zz}\right) & \left(P_{11}-P_{12}\right)S_{yz} \\ \left(P_{11}-P_{12}\right)S_{xz} & \left(P_{11}-P_{12}\right)S_{yz} & P_{11}S_{zz} + P_{12}\left(S_{xx}+S_{yy}\right) \end{pmatrix} \tag{5.36}$$

Here we use the Voigt notation for the elasto-optic tensor. We will consider now the case of a Rayleigh surface acoustic waves with $\vec{\boldsymbol{k}}_{SAW} \parallel \vec{\boldsymbol{x}}$ excited electrically by an IDT. The only non zero strain components at the surface are S_{xx} and S_{zz} . Hence the permittivity tensor will be simplified to:

$$\Delta\varepsilon = -\varepsilon^2 \begin{pmatrix} P_{11}S_{xx} + P_{12}S_{zz} & 0 & 0 \\ 0 & P_{12}\left(S_{xx}+S_{zz}\right) & 0 \\ 0 & 0 & P_{11}S_{zz} + P_{12}S_{xx} \end{pmatrix} \tag{5.37}$$

Now we can define two refractive indices for light propagating along the z axis:

$$\begin{cases} n_x = \sqrt{\varepsilon + \Delta\varepsilon_{xx}} \\ n_y = \sqrt{\varepsilon + \Delta\varepsilon_{yy}} \end{cases} \tag{5.38}$$

Since the strain is of the order of 10^{-5}, we assume that the perturbation of the indices is small and can be expressed as follows:

$$\begin{cases} n_x = n\left(1 - \varepsilon\frac{P_{11}S_{xx}+P_{12}S_{zz}}{2}\right) \\ n_y = n\left(1 - \varepsilon\frac{P_{12}(S_{xx}+S_{zz})}{2}\right) \end{cases} \tag{5.39}$$

Using formula 5.32 developed for the Voigt effect, the polarization rotation due to the SAW is written as:

$$\Delta\beta_{strain} = \Re\left[\frac{n^3(P_{11} - P_{12})S_{xx}}{2\,(n^2 - 1)}\right]\sin 2\beta \tag{5.40}$$

From equation 5.40 we can calculate the polarization rotation due to the photo-elastic effect for a given strain, if we know the elasto-optic constants. For GaAs it is around 1.2 µrad for $S_{xx} = 10^{-5}$ and $|P_{11} - P_{12}| = 0.06$ (for $\lambda = 870$ nm) [163]. The polarization rotation is sensitive to the in-plane strain component S_{xx}. On the contrary, with the interferometric measurements which is the most common method for SAW detection, only the out-of-plane displacement is probed (U_z). However, it provides very high sensitivity: a pico-meter surface displacement can be observed with it. We used the PE effect to detect SAW excited electrically and interferometric measurement were used for metallic samples with SAW generated optically.

5.4. Materials

In this thesis, two different groups of materials were used. For the studies with electrically excited SAWs we worked with GaMnAs (Fig. 5.7 (a)), which is a good material for PMOKE measurement, because of the relatively low out-of-plane anisotropy. Moreover, the FMR frequency can be easily tuned with the magnetic field. However, it required low temperature (T<100 K). Because of this requirement and the fact that it cannot be grown on a transparent substrate, it was not used in the second project where acoustic waves are excited through the substrate with a tightly focused laser beam and magnetization variations are detected on the other side (Fig. 5.7 (b)). This set-up specification makes another group of materials perfect candidates: ferromagnetic metals that have a Curie temperature well above room temperature and that absorb very well visible light. More details on these materials will be given below.

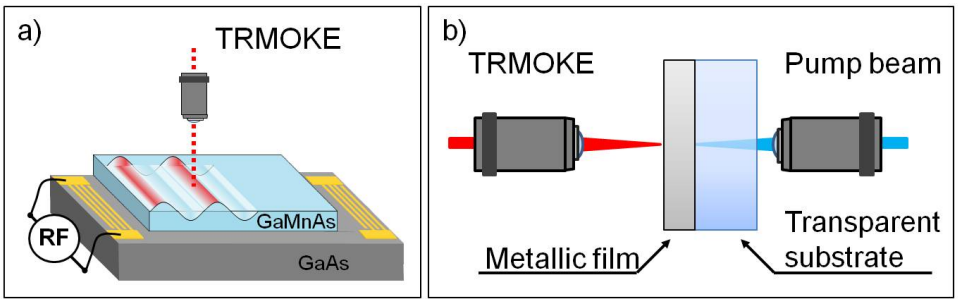

Figure 5.7.: Schemes of two experimental set-ups for SAW generation (a) electrically and (b) optically.

5.4.1. GaMnAs

GaMnAs joins together two important properties: ferromagnetic and semiconductor, used in the information technology for data storing and processing respectively. This material gave a green light for developing spintronic devices. The concept of GaMnAs relies on replacing of few Ga atoms from the GaAs lattice by Mn atoms. Comparing the electronic structure of the two atoms (Ga: $3d^{10}4s^2p^1$, Mn: $3d^54s^2$), one can see that the 3d shell will now be only half filled but also, what is more important for the magnetic order, due to the lack of 4p valence electron, one hole is introduced. This weakly bound hole mediates the interaction between the localized Mn spins and aligns them ferromagnetically. The first GaMnAs sample was grown by H. Ohno in 1996 [164]. In order to incorporate a few percents of Mn atoms, the growth temperature needs to be below 300°C, which is at least two times lower than the growth temperature of GaAs (∼600°C). However, the lowered growth temperature leads to the reduction of the film quality, introducing defects such as interstitial Mn and As in antisites and post-growth annealing needs to be achieved in order to remove part of the defects [165]. The Curie temperature (T_C) is related to the concentration of Mn ions. T_C increases monotonically with the effective concentration of Mn (x_{eff}) and hole concentration (p) [166]. Up to now, the highest reported Curie temperature for GaMnAs is 191 K [167], which is still far from room temperature. According to the theory developed in 2000 [34], room temperature T_C should be achieved for $x_{eff} = 12.5\%$ and $p = 3.5 \times 10^{20} cm^3$. However, now we know that this concentration will be very hard to achieved, since Mn-atoms can also occupy the interstitial position in the lattice and couple antiferromagnetically to the Mn in Ga position [168].

Despite its low T_C, GaMnAs is a good test-bench material because its magnetic and magneto-elastic properties can be tuned by the epitaxial strain, and the Mn and hole concentrations.

In this work, we have studied one GaMnAs sample. GaMnAs was our first choice, since our group has a great experience with it, *e.g.* the former PhD student Sylvain Shihab developed TRMOKE set-up to study magnetization precession and to

determine the spin stiffness constants with the use of Kerr and Voigt effects. The sample was carefully architectured by Aristide Lemaître from C2N laboratory to have a strong in-plane anisotropy. He has grown 45 nm thick GaMnAs film on (001) GaAs substrate, therefore with built-in epitaxial strain (see Eq. 3.7). After growth, the sample was annealed for 16h at 200°C. The Mn concentration was $x_{eff} = 5\%$ and Curie temperature $T_C = 130$ K.

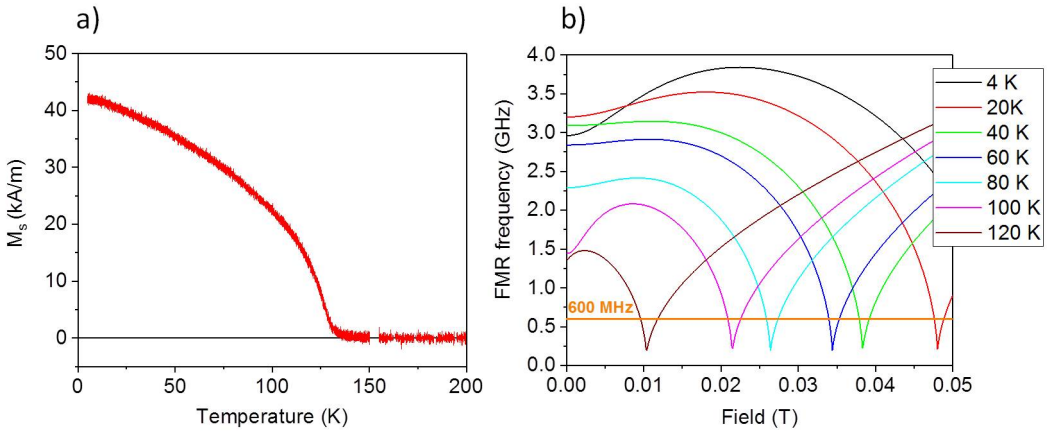

Figure 5.8.: (a) The saturation magnetization as a function of temperature obtained using VSM. (b) The calculated FMR frequency versus magnetic field along the hard magnetic axis [110] for different temperatures.

Two factors determined the conditions of our measurement: M_s and the frequency of SAW. With the VSM we have measured the saturation magnetization dependence on the temperature, showing that the magnetization decreased by a factor of 2 from T=0 K to T=100 K (Fig. 5.8 (a)). Lower magnetization means lower MOKE signal. The second important quantity is the FMR frequency calculated from the anisotropy constants measured with cavity FMR as a function of the magnetic field. The curves for 7 temperatures are presented for a field applied along the hard axis (Fig. 5.8 (b)). They possess the same features: first the FMR frequency decreases until magnetization is aligned with the field and after that it increases again. We have chosen to work with SAW frequency below 600 MHz (wavelength $\geqslant 5\mu$m) compatible with our spatial resolution. Therefore we need to lower the FMR frequency by an in-plane field as shown here in order to match the SAW frequency.

5.4.2. Ferromagnetic metals

We have studied four ferromagnetic films for different reasons. Galfenol, an alloy of Fe and Ga was chosen because of its very high magnetostriction. It was reported that substituting 19 % of Fe by Ga-atoms in thin epitaxial layers, makes the magnetostriction coefficient increase 10 times ($\lambda_{100}^{Fe} = 0.2 \times 10^{-4} \rightarrow \lambda_{100}^{FeGa} = 2.6 \times 10^{-4}$)

[169]. This is a very high value for thin layers. We used two different FeGa films one was prepared by Mahmoud Eddrief at INSP and another one by Rocio Ranchal at Universidad Complutense de Madrid. The latter one was prepared to have an in-plane uniaxial magnetic anisotropy. Our second choice was Nickel due to low FMR frequency which could be easily made equal to the SAW frequency even in zero magnetic field. This sample was made by Loïc Becerra at INSP. Moreover, we also investigated Cobalt which is likewise known as a good magnetostrictive material.

5.4.2.1. Nickel

Previous studies have revealed that the magnetic properties such as saturation magnetization, coercive field, hysteresis squareness, static strain of magnetic films depend on their thickness and on which substrate they were deposited [170, 171]. In this work, we have studied different thicknesses of Nickel films (20, 100 and 300 nm) sputtered on glass, since the substrate had to be transparent.

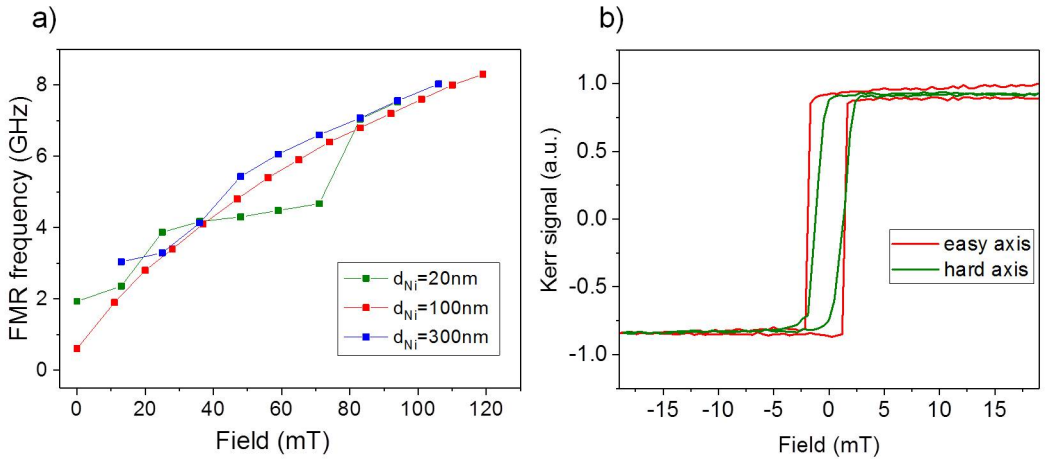

Figure 5.9.: (a) The BBFMR characteristics for the three Nickel films. (b) Hysteresis cycles for 20 nm Nickel sample measured with static longitudinal MOKE.

In Figure 5.9 (a) the FMR resonance frequency obtained from BBFMR (Fig. 5.2 (b) and (c) for the 100 nm sample) is plotted versus magnetic field for the three Nickel samples. These data clearly show that a resonance frequency below 1 GHz in zero magnetic field can be obtained for the 100 nm thick Nickel sample. That is why we mainly worked with this sample as you will see later in the experimental part (Chapter 7). Samples have a small in-plane anisotropy as it is presented in graph (b) of Figure 5.9. The typical magnetization saturation for bulk Nickel samples is $M_S = 0.5 \times 10^6$ A/m [27].

5.4.2.2. FeGa

We studied the two FeGa sample. The first sample was a 88 nm thick $Fe_{0.8}Ga_{0.2}$film grown by molecular beam epitaxy on a $SrTiO_3$ substrate (STO). Galfenol was capped with a 10 nm Au layer to protect it from oxidation. With longitudinal MOKE we found that the sample is isotropic in the plane (Fig. 5.10). Broadband FMR measurements showed that the resonance frequency in zero magnetic field is around 3.8 GHz, which is quite high compared to the Nickel samples. The sample parameters are $M_S \cong 1.4 \times 10^6$ A/m and anisotropy constants $K_{2\perp} \cong 4.7 \times 10^5$ J/m^3, and $K_{2\parallel} \cong 0$ J/m^3 [29].

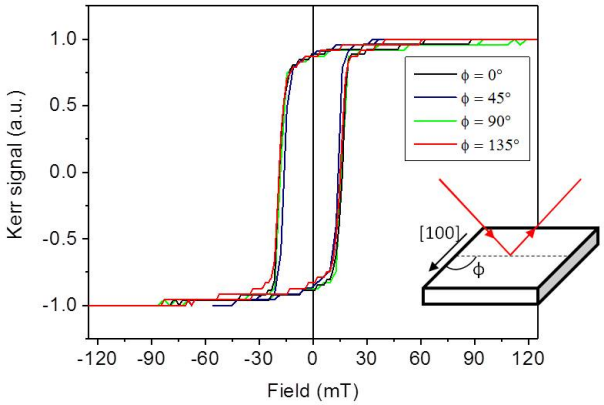

Figure 5.10.: FeGa on STO substrate. The hysteresis cycles from longitudinal taken along 4 different axes.

The second sample was a 120 nm $Fe_{72}Ga_{28}$ layer sputtered on a 500 µm Sapphire substrate cut along the C- plane (0001). The two buffer layers of Molybdenum were deposited: 14 nm on Sapphire/FeGa interface and 7 nm on top of the FeGa layer. The details on the sample preparation can be found here in ref: [172]. This sample was prepared to have an in-plane uniaxial magnetic anisotropy. The longitudinal Kerr cycles are presented in Fig. 5.11 (a), showing a strong uniaxial anisotropy.

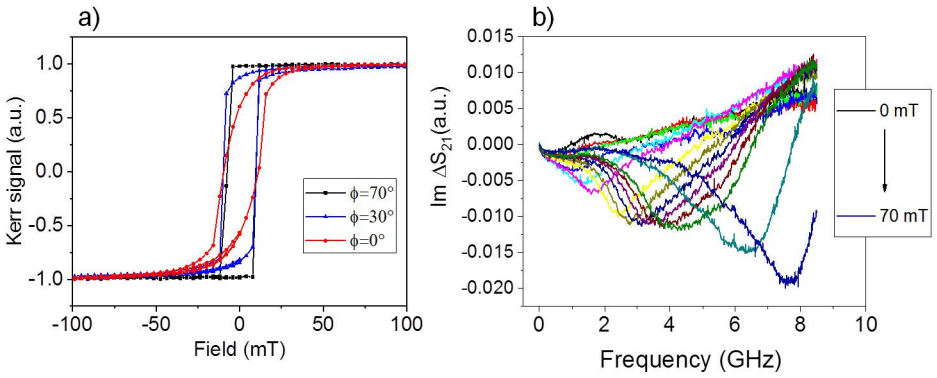

Figure 5.11.: The hysteresis cycles of FeGa on Sapphire substrate measured with longitudinal MOKE and (b) BBFMR characteristic with magnetic field applied along the hard axis.

To find the precession frequency dependence on magnetic field we performed BBFMR (Fig. 5.11 (b)). The FMR frequency was never lower than 1 GHz ($f_{FMR}(\mu_0 H{=}17\text{mT})$=1.2 GHz). However, we knew that with a Sapphire substrate we can aim for higher SAWs frequency than with glass due to its higher Rayleigh velocity.

5.4.2.3. Cobalt

The last sample was 100 nm Cobalt on Sapphire. This sample was prepared by sputtering by Stefan Suffit at University Paris VII. The layer was not uniform, showing many micro-holes (Fig. 5.12 (a)). We used two different substrates but we could not get rid off of the holes. The sputtering conditions were probably not optimal. Nevertheless, we obtained a good MOKE signal (Fig. 5.12 (b)). It was found that Cobalt layer was isotropic. In the experiment using optical SAW excitation, we did not experience any difficulties due to these holes.

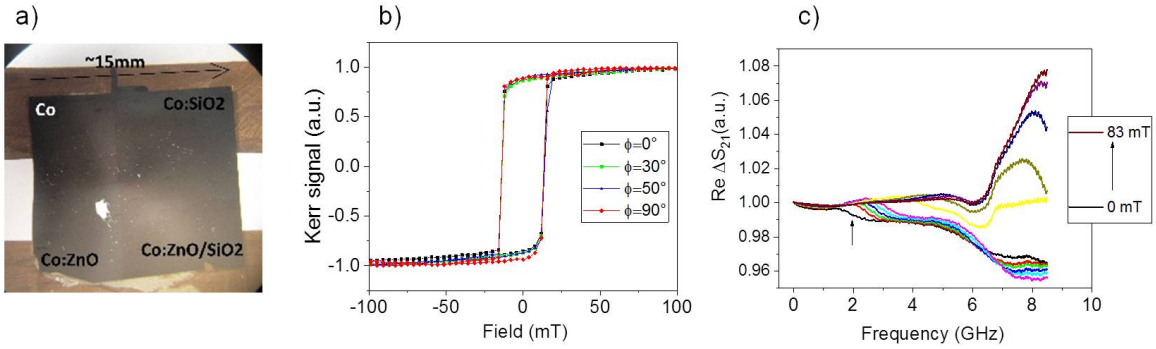

Figure 5.12.: Microscope image of Cobalt on Sapphire. Here shown with different cap layers which were tested to enhanced the Kerr signal. (b) The hysteresis measured with longitudinal MOKE configuration. (c) Result of the BBFMR for a field from 0 to 83 mT.

The precession frequency at zero magnetic field was around 2 GHz (arrow in Fig. 5.12 (c)). The M_S value for Cobalt is $M_S = 1.4 \times 10^6$ A/m [27].

6. Spatial and dynamical control of magnetization with electrically excited surface acoustic waves

Table of content

In this chapter, the results of magnetization precession excited in a thin film of (Ga,Mn)As with the use of electrically generated SAWs will be presented. This is the first time that magnetization precession is detected optically in this type of system. For that purpose, we developed a unique experimental set-up and the method to distinguish magnetic and elastic contributions from MOKE and PE effect, respectively. The results show the resonant magneto-elastic coupling, in good agreement with the model. The IDT design used allowed us to generate SAWs at four different frequencies 151, 301, 452 and 602 MHz. We will discuss the efficiency of detection of the acoustically-induced resonant magnetization dynamics at these frequencies.

This project was led in close collaboration with Jean-Yves Duquesne.

6.1. Phase synchronization

Time-resolved measurements require stable phase locking between the excitation and the detection signals. In the case of magneto-optical measurements, with magnetization precession excited by electrically generated SAWs, the common solution to synchronize the optical probing pulses and the electrical signal is a master-slave configuration. The laser frequency and the frequency of the electrical wave are imposed by a common clock. This can be done with laser systems equipped with the synchro-lock function, where the laser cavity length is tuned with a movable mirror mounted on a piezoelectric stage. The laser repetition rate frequency has to be a multiple of 10 MHz to make it suitable for a phase-locked loop. For the acoustic wave excitation, the clock of the pulse generator is synchronized with the common clock using the 10 MHz input [173].

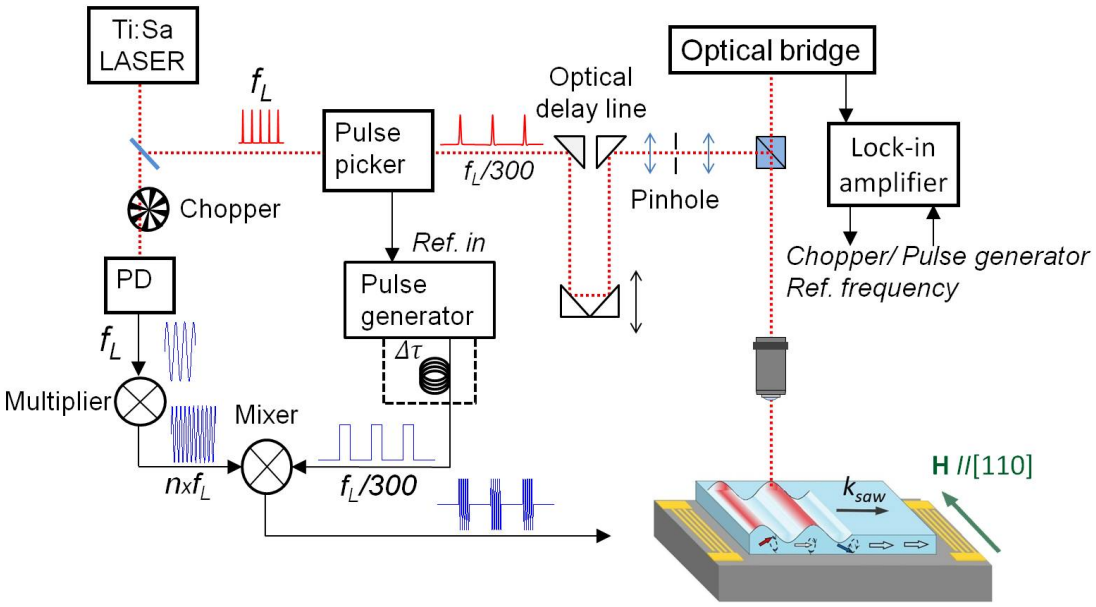

Figure 6.1.: Experimental set-up

However, this technique requires expensive devices. In this thesis, we proposed a simpler, alternative and widely accessible approach. Herein, we used a laser signal to create the electrical signal. The laser frequency was picked up with a photodiode, then this signal was converted with RF components to higher frequencies. Additionally it was shaped in a form of burst a few hundred ns long which were sent to the IDT. Because the SAW frequency f_{SAW} was built from the laser repetition rate (f_L) a stable phase lock between the SAW and the optical probe pulses was assured.

6.1.1. Experimental set-up

For the purpose of this project an existing pump-probe set-up, developed by Sylvain Shihab was modified. The operating frequency $f_L \cong 75$ MHz of the Ti:Sapphire laser was picked up by a slow Silicon photodiode (PDA10A-EC, Thorlabs) positioned behind the backside polished mirror (Fig. 6.1). Then the electronic signal was processed for the SAW excitation. The harmonics of the fundamental f_L were sufficiently lowered with a 50dB rejection bandpass filter. Next, multiples of the laser frequency n$\times f_L$ (n = 2, 4, 6, 8) were obtained with various RF multipliers. To generate $\sim$ 151 MHz, 301 MHz and 602 MHz we have used n/2 number of doublers, except for the 452 MHz where a $\times$ 6 multiplier was used. After each multiplication of the frequency, the signal was filtered with a band-pass filter (Fig. 6.2).

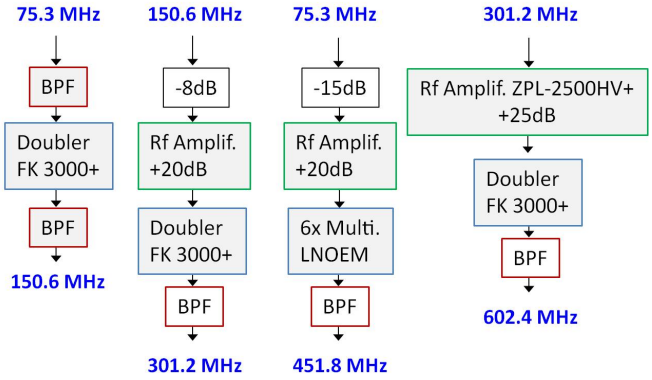

Figure 6.2.: RF connections for generation of harmonic frequencies of the laser repetition rate. RF amplifiers were used because the multipliers required a very specific RF input power. They may also introduced other harmonics, that is why a band-pass filter (BPF) was placed at the output.

The part of the light reflected from the mirror (nearly 100%) was sent to an APE pulse picker. This device is based on the acousto-optic effect. It allows to divide f_L by an integer number N, where N is 2 - 260 000. The efficiency of this process depends on the chosen N, for N higher than 40, an efficiency of 80% can be obtained. Every laser pulse at the frequency f_L /N can be delayed by 12 ns with a 6$\times$60 cm long motorized optical delay line. The maximum temporal resolution was $\sim$ 0.5 ps. The laser probe beam was spatially filtered with a 20 µm pinhole, positioned between two lenses in the plane conjugated with the sample plane. It ensured very high spatial stability on the sample surface during scanning the delay line. The beam was expanded 1.7 times, to fully cover the entrance pupil of the Mitutoyo (LCD Plan Apo 20x, NA=0.4) objective, as a result the spot size of $\sim$ 1 µm (at FWHM) was obtained. The probe beam fluence was about 1.5 $\frac{mJ}{cm^2}$ and the wavelength was $\lambda = 722$ nm.

Before delivering the n$\times f_L$ electronic signal to the IDT, it was shaped into bursts. For this purpose the signal was mixed with a square wave generated with the pulse

generator (81150A Keysight Pulse function arbitrary noise generator) at the pulse picker frequency f_L /N. In order to generate pulses at the pulse picker frequency, the pulse generator was externally triggered via the pulse-monitor electronic output of the pulse picker (the maximum accepted frequency for the Keysight pulse generator was 120 MHz). Thus both the carrier frequency and the envelope frequency were commensurate with f_L . That also protected the signal in the envelope from drifting. Moreover, with the pulse generator we could delay the bursts with respect to the optical signal. The maximum delay time was equal to the burst period, typically a few µs. Finally, the produced signal was applied to the IDT after a 40 dB amplifier. The highest reachable power was around 36 dBm (∼4 Watts), it depended on the carrier frequency used and the electronic configuration. The typical strains are in the order of 6×10^{-5}(for 100 mW of input power) [60, 174].

6.1.2. Jitter measurement

To quantify the stability of the set-up we have performed jitter measurements. Jitter is defined as the short-term variation of the transition edge positions in time from their ideal values [175, 176]. There exist many types of jitter which help to characterize the timing performance. Exemplary types of the deterministic jitter are: Period jitter, Cycle to Cycle jitter, Time interval error (TIE) jitter. The Period jitter and Cycle to Cycle jitter refer to the variation of the clock period, measured either as the deviation of a large number of cycles from the ideal (average) period value or as the difference of the adjacent cycles across the given number of cycles. When the ideal clock source is available, the TIE jitter can be measured, which is the difference between the location of the ideal edge and the signal edge (Fig. 6.3).

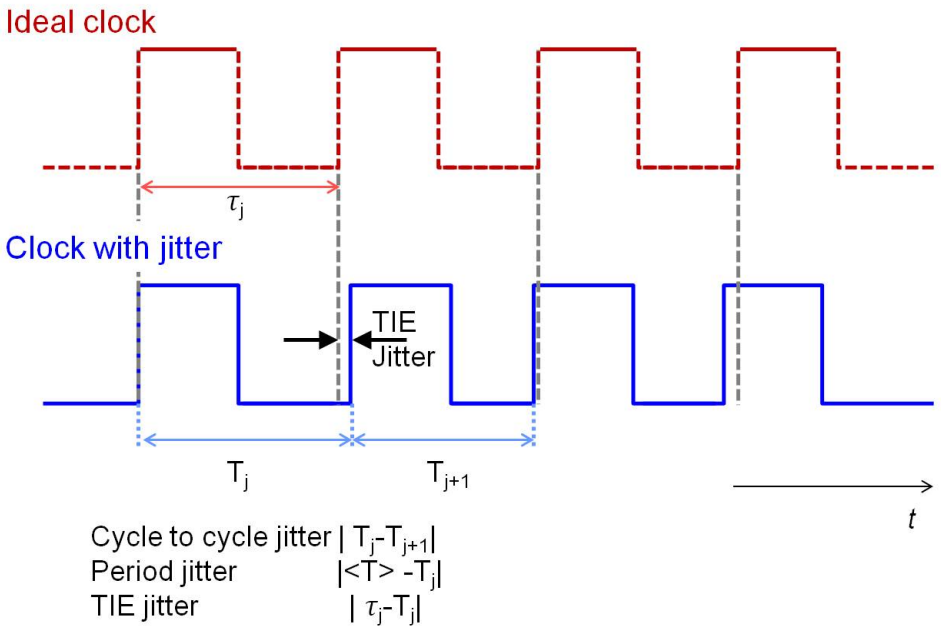

Figure 6.3.: Three main types of the deterministic jitter: Cycle to cycle, Period and TIE jitter.

In the case when the ideal clock signal is used as the reference source to generate the signal then a more appropriate name for TIE jitter is the edge-to-reference jitter [175]. This jitter was the most relevant for us. Therefore, to estimate the jitter we displayed on the oscilloscope (LeCroy HDO9204) traces of the square signal generated with the pulse generator and the laser pulses picked up with the fast photodiode (mounted for this purpose in the set up) at f_L /300 (Fig. 6.4). The signal was triggered with the laser pulses. The jitter was measured with the delay oscilloscope function which measures the delay between the trigger and the signal edge. The delay was measured over 1000 samples. The most meaningful value which describes the jitter is the standard deviation which was found to be equal to 13.1 ps, which is much lower than 1% of a period of the lowest SAW period used in this work.

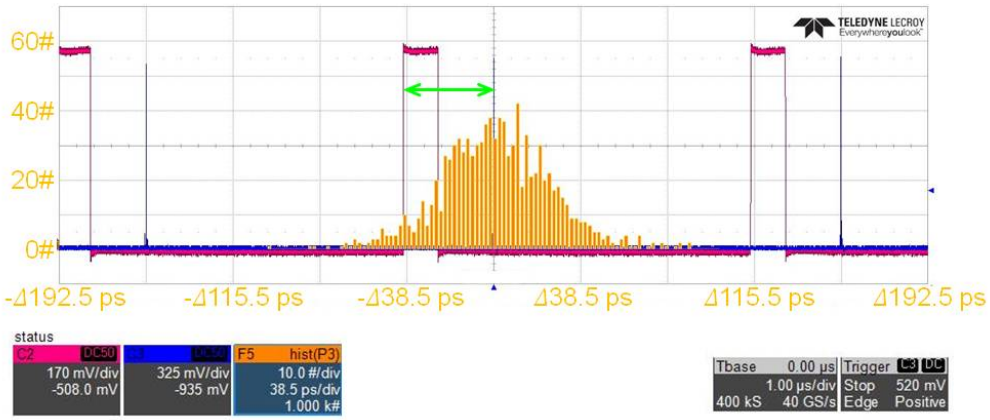

Figure 6.4.: Time traces of the laser pulses and square wave at f_L /300 with the distribution of the TIE jitter.

6.1.3. Lock-in detection of the optical signal

Linearly polarized laser pulses reflected from the sample return through the same objective and are delivered to the balanced optical bridge detector (Thorlabs PDB150A) (Fig. 6.1). It consists of two photodiodes, on which the two orthogonal polarization components are projected by a polarizing beam splitter. Then the difference is amplified.

The signal from the bridge was next detected with the Lock-in amplifier (7270 General-Purpose DSP Lock-in Amplifier) at the frequency of the mechanical chopper. The chopper was placed just before the slow photodiaode to modulate the burst at 541 Hz (Fig. 6.1). This configuration allows to measure the polarization rotation lower than 1 µrad.

The polarization rotation was calculated from the following formula:

$$\delta\beta = \frac{s_{Lock-in}^{Chop}}{4\mathbb{R}s_{Lock-in}^{ps,\,1d}} \tag{6.1}$$

where $s_{Lock-in}^{Chop}$ is the signal detected at the chopper frequency, $s_{Lock-in}^{ps,\,1d}$ is the signal detected on one diode at the pulse picker frequency and $\mathbb{R}$ is the conversion ratio equal to to 1.3 for a bridge gain 10^6. The $s_{Lock-in}^{Chop,\,1d}$ was used not only to find the polarization rotation but also to normalize the time domain signal since the light intensity was not the same for all the delay line positions because of the light divergence. The details on the derivation of Formula 6.1 can be found in the Appendix A.

6.1.4. IDT design

The specific design of an IDT allows to excite efficiently certain overtone harmonics of the fundamental frequency (f_0). In our case the frequencies were imposed by the synchronization strategy. When a certain design is chosen the parameters determining which frequencies are excited are the digit periodicity, the number of digits and the metallization ratio. The architecture of the IDTs used in this work was elaborated with the help of Jean-Yves Duquesne. The frequency response of the IDT is calculated from the so-called δ-function. Here we will briefly describe it based on an example of the basic IDT design presented in Fig. 6.8 (a). The full description can be found in [63]. The alternating voltage applied to the IDT creates a gradient of the electric field which is the highest at the edges of the electrodes where charges are accumulated. The distribution of the electric field can be illustrated by the two δ-functions of the same polarity associated with each tooth (Fig. 6.5). This model can be simplified using only one equivalent δ-function at the center of an electrode. Hence the time domain response of the IDT is given as [63, 177]:

$$h(t) = \sum_{n=0}^{N-1} (-1)^n A_n \delta(t - t_n) \tag{6.2}$$

and in the frequency domain Equation 6.2 is:

$$H(\omega) = \sum_{n=0}^{N-1} (-1)^n A_n e^{-i\omega t_n} \tag{6.3}$$

where A_n is the amplitude of each delta and t_n is the time interval from the n_{th} electrode to the detection point: $t_n = t_0 + n\frac{d}{v} = t_0 + n\frac{\pi}{\omega_0}$.

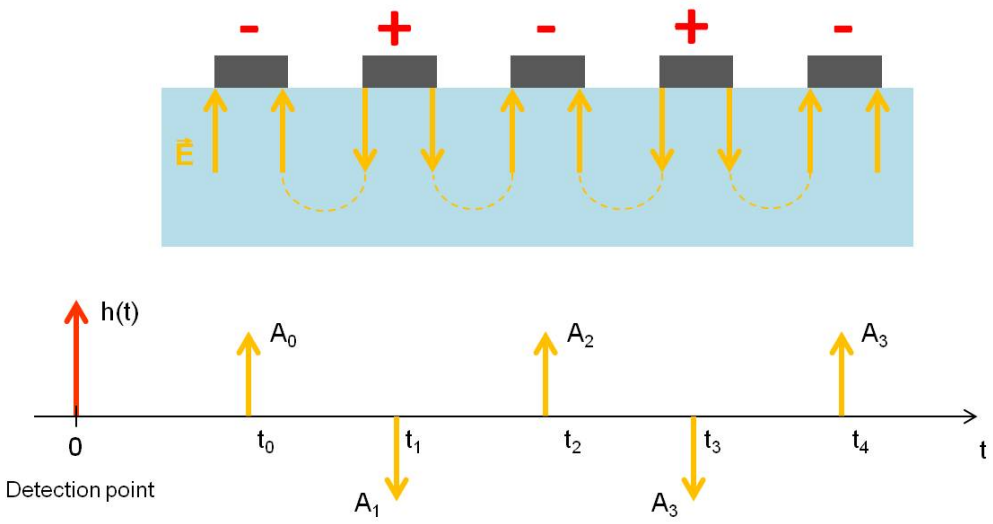

Figure 6.5.: Illustration of the electric field distribution as the δ-function in a uniform IDT [63, 177].

Then the condition for constructive summation is $\frac{\omega}{\omega_0} = m$, where m can only take odd numbers as it is the Fourier transform of a square wave. Thus only the odd multiple of the fundamental frequency will be sustained. From Equation 6.3, we can find that the response of the IDT for the frequency detuned from the synchronous frequency f_0 is in the form of a sinc function:

$$H_n(f) = A_n N \frac{\sin X_m}{X_m} \qquad X_m = N\frac{\pi}{2}\frac{f - mf_0}{f_0} \tag{6.4}$$

The boundaries of the bandwidth are located where $H_n(f)$ goes to zero. This is for $N = 2\frac{f_0}{\Delta f}$ with $\Delta f = f - mf_0$, which can be written as:

$$\frac{\Delta f}{f_0} = \frac{2}{N} \tag{6.5}$$

From 6.5 we can directly see that the bandwidth is inversely proportional to the number of teeth. It means that increasing the N we narrow the bandwidth (Fig. 6.6). Moreover, the value of N also governs the transient time. It increase with N, which means that to obtain a plateau, the burst width has to be long enough but it cannot be too long if we want to have a clear separation from the electromagnetic radiation on the receiving IDT as it will be shown later.

These simple calculations show that the even harmonics cannot be excited with a highly symmetric structure. In a paper by Schülein [178] the design for odd and even

harmonics excitation was proposed. He showed that double, triple, quadruple and less efficiently sextuple ($f_m = m \times f_0$, $m = 1, 2, 3, 4, 6$) harmonics can be generated. The fundamental frequency was defined by the longest periodicity. The possibility to generate even and odd harmonics allows to characterize the investigated system with discrete SAWs frequencies laying close to each other. We adopted this so-called split-52 design to our experiment (Fig. 6.8 (b)). The highest frequency was chosen for the corresponding wavelength to be compatible with a good spatial resolution with the probe beam. The diameter of the beam spot was around w=1 µm (full width at half maximum). Hence the λ_{SAW} for quadruple frequency was selected as $\lambda_{SAW} = \frac{\upsilon_R}{8 \times f_L} = 4.6$ µm $> 4 \times w$. Thus the period of the IDT had to be designed to fit to the laser frequency ($d = \frac{\upsilon_R(T)}{2 f_L}$). Since the IDT period depends on the Rayleigh velocity which varies with temperature and one of our restriction was to work in the temperature range of 3-100 K (Ga,Mn)As, the IDT had to be well tailored. The IDT period was designed for υ_R at the center of the temperature range. To ensure efficient work in the wide temperature range the number of digits could not be too high. We tested two sets of IDT on GaAs: one with N=15 and the other with N=25. We found that the -3 dB bandwidth was $\Delta f_{N=25} \simeq 3.9$ MHz and $\Delta f_{N=15} \simeq 6.1$ MHz.

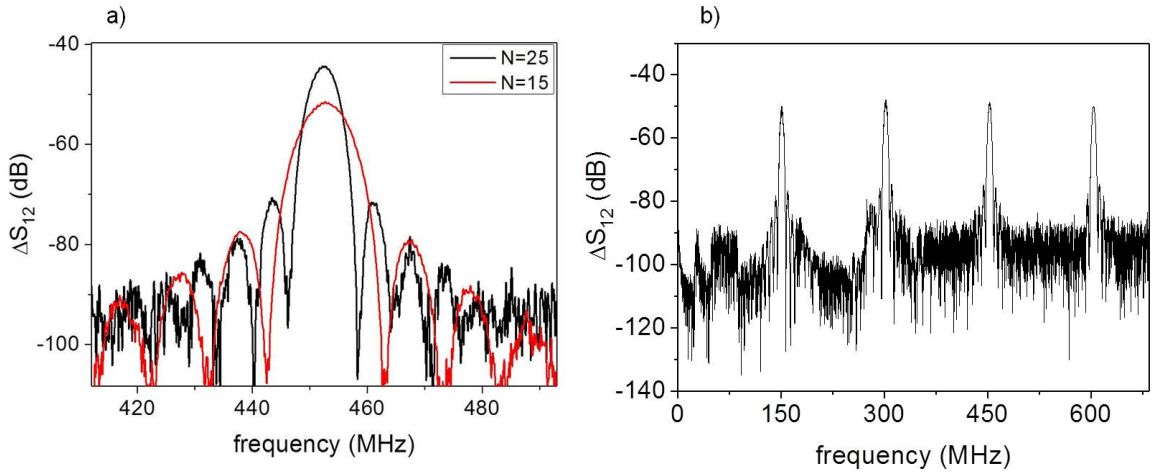

Figure 6.6.: (a) Frequency span of the IDT with N=15 and N=25 measured with a VNA, for a 0 dBm excitation power. (b) The frequency response of the IDT with 25 digits.

However, the power of excited SAWs was 7 dB lower for the N=15 therefore we decided to work with the narrower bandwidth design (N=25) (Fig. 6.6 (a)). In Figure 6.7 we plotted the center frequency for four harmonics vs temperature. The violet line in the graphs indicates the multiple of the laser frequency. For the scale we put on the right the $\Delta f_{N=25}$ bandwidth. As you can see the deviations from the maximal frequency are far below the bandwidth.

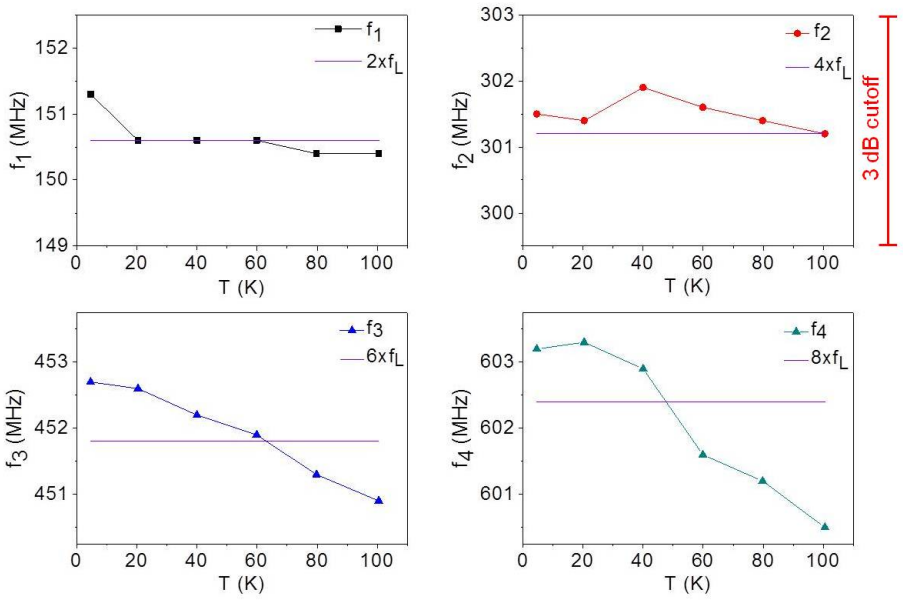

Figure 6.7.: Temperature dependence of the central frequency of the four harmonics excited with the IDT of split 52 - design. The horizontal, purple line indicates the multiple of the laser frequency.

Note that there exists another approach for wide frequency SAWs excitation. Instead of decreasing the number of teeth, a small linear variation of the IDT periodicity (period changed by 10% in a 400 µm long IDT structure) can be introduced [179]. As the result, the bandwidth is enlarged by the frequency chirp.

The (Ga,Mn)As sample was made by A. Lemaître, see Chapter 5 Section 4.1 for its full characteristic. Than the sample was processed by Loïc Becerra at INSP by optical lithography with the lift-off method to deposit the IDTs. First the 2×2 mm^2 mesa of the 45 nm thick GaMnAs film on GaAs was prepared by the wet etching technique. Then the whole sample was covered with a 1.2 µm thick positive photoresist by a spinning technique. Next, a UV laser beam traced the pattern according to the IDT design and the irradiated resist is removed. Finally a 45 nm thick Aluminium layer was evaporated forming the IDTs and contacts on GaAs. In the last step, the non-irradiated photoresist is removed with Acetone and the Aluminium remained only in the places illuminated by the laser.

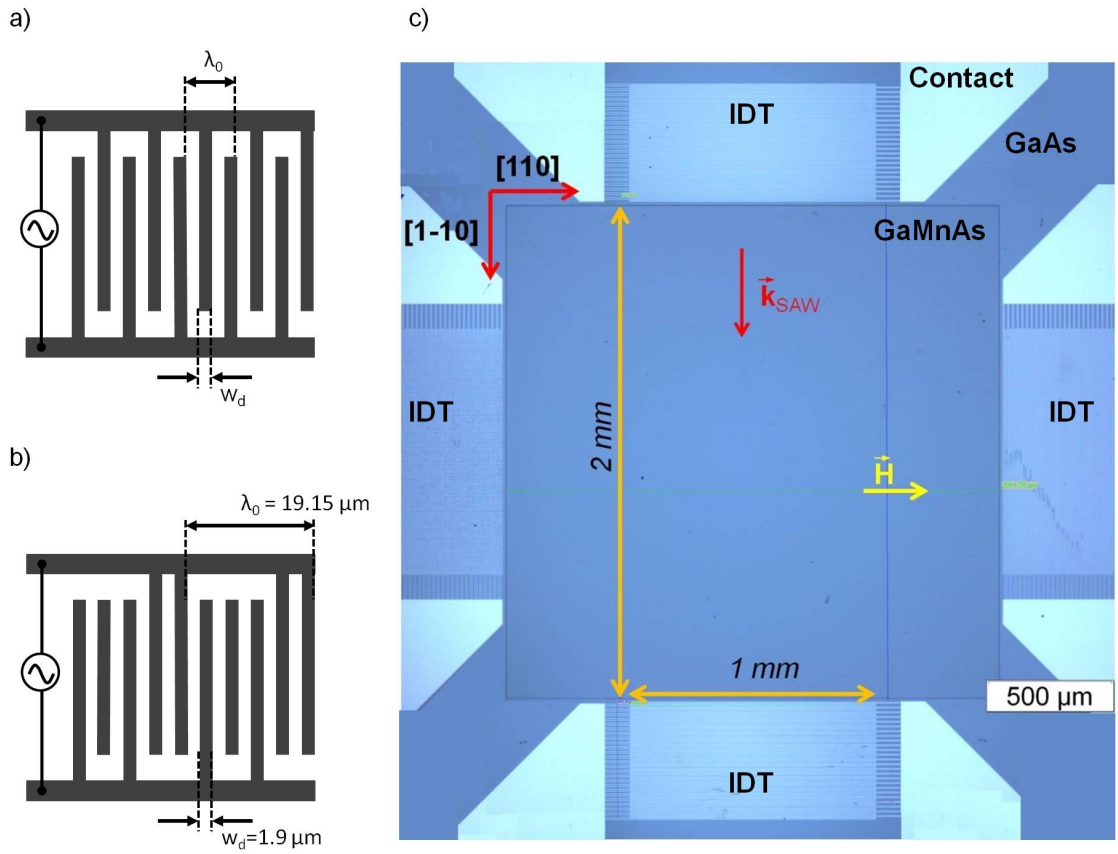

Figure 6.8.: (a) The most common design of IDT. The metallization ratio is defined as $\frac{2w_d}{\lambda_0}$ (b) Final IDT 52 design and (c) an image of the sample taken with an optical microscope.

Two pairs of IDTs were deposited: one for the propagation of SAW along the easy axis and the other along the hard axis of (Ga,Mn)As (Fig. 6.8 (c)). The SAWFMR studies obtained before for the same sample showed that these the resonance field and attenuation amplitude were similar [180]. We have chosen to work with $\vec{\boldsymbol{k}}_{SAW}$ along the easy axis because these IDTs were more efficient. Moreover, we used the SAWFMR measurement to check the resonance field and the conditions for the linear regime of magnetization precession.

6.1.5. Phase between the optical and electrical signal

To define the phase between the SAWs and laser pulses we placed the fast photodiode (Thorlabs DET10A) in front of the sample, so the laser pulses were visualized on the oscilloscope with the electronic bursts. The burst and laser signals were triggered on the latter one. We found that there was a fixed delay $\tau_f \simeq 657$ ns between the laser pulse and the first rising edge of the burst, due to the different velocities of

the electric and optical signals (typically $v_e \simeq 0.7c$). Based on this measurement we found an empirical formula for the delay ($\Delta\tau$) of the acoustic waves in order to define their spatial position between two IDTs:

$$\Delta\tau = \tau_P - \frac{a}{v_R} - \tau_f + \tau_w/2, \tag{6.6}$$

where τ_P is the burst period (typically a few µs), $\frac{a}{v_R}$ described the arrival time to the detection point and τ_w is the burst width (usually 400ns) (Fig. 6.9). Here we put $\tau_w/2$, which is the situation where the center of the burst is detected.

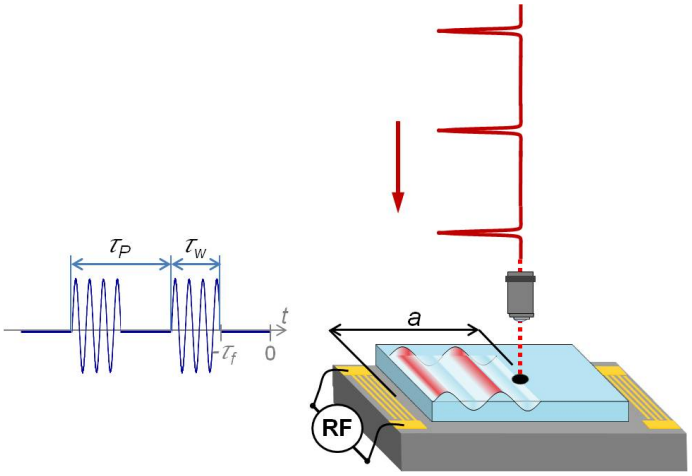

Figure 6.9.: The determination of the phase between the SAW's bursts and laser pulses was essential to detect the signal.

6.2. Detection of the magneto-acoustic signal

We spent about one year building and characterizing the set-up. Now the data obtained for the (Ga,Mn)As sample will be presented. Figure 6.10 shows typical time-resolved polarization rotation (TRPR) measurements taken at 60 K for the four IDT excitation frequencies 151, 301, 452 and 602 MHz available in our sample. The probe beam was polarized at 60° with respect to $\vec{k}_{SAW}$. The frequency of the detected signal was found to be equal to the excitation frequency. The signal-to-noise ratio is good for all frequencies and we do not see a big influence of the decrease of λ_{SAW} to the beam spot size ratio. Furthermore, to illustrate how high frequencies can be measured, the result for excitation with 904 MHz is also presented in Fig. 6.10 (e). The signal still looks very good and probably we can aim for 1 GHz, even though in this case $\lambda_{SAW} < 3$ µm. We see also 452 MHz in the excitation signal, because we did not have an electronic filter for this frequency since we did not plan

to work with it. The amplitude of the TPRP signals changed with magnetic field, but only up to T_C, above which they became field independent. Moreover, we have observed a polarization dependence of the signal below and above the T_C.

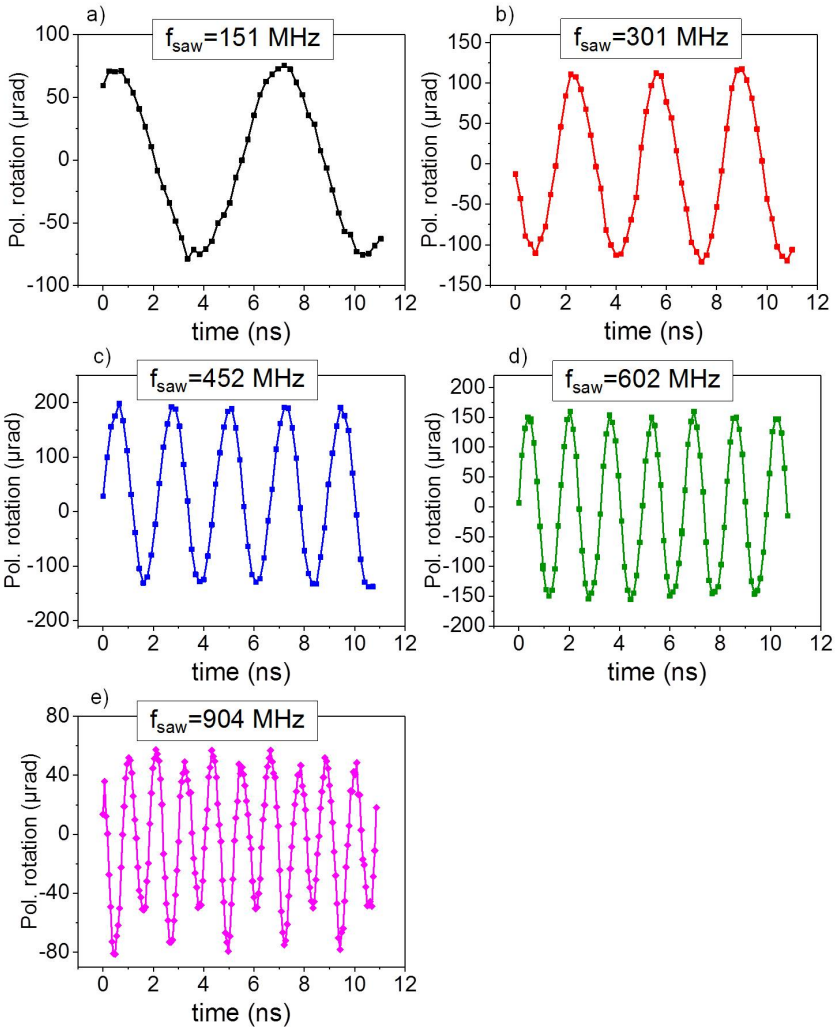

Figure 6.10.: Polarization rotation signal measured as a function of the optical delay for five SAW excitation frequencies (a) - (d). The signal was taken with a magnetic field μ_0H=19.5 mT applied along the hard axis at a temperature of T=60 K. (e) f_{SAW} = 904 MHz. This frequency was measured at T=90 K and with μ_0H= 0.7 mT. The second frequency in (e) is very possible due to the presence of 452 and 904 MHz in the excitation signal.

We assigned it to three different contributions, two of magnetic origin and one of acoustic origin. We were sensitive to the variation of the out-of–plane and in-plane magnetization components due to the Polar Kerr effect (§ 5.2.2) and MLD (§ 5.2.3) respectively. An additional contribution to the polarization rotation came from the acoustic wave to which we were sensitive through the photo-elastic effect (§

5.3). Hence the measured polarization rotation can be described by the following expression:

$$\delta\beta(\beta,\, H,\, t) = K\delta\theta(H,\, t) + 2V\delta\varphi(H,\, t)\cos 2(\beta - \varphi_0(H)) + P_E S_{xx}(t)\sin 2\beta, \quad (6.7)$$

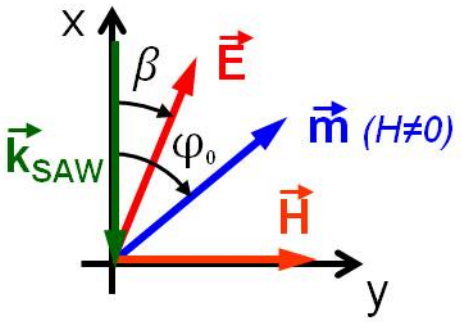

Figure 6.11.: Coordinate system for polarization rotation measurements.

where P_E is the photo-elastic constant which was defined in section 5.3 and for isotropic materials $P_E = \Re\left|\frac{n^3 P_{44}}{n^2-1}\right|$, $\delta\theta(H,\, t)$ and $\delta\varphi(H,\, t)$ are the dynamic functions of magnetization orientation given as:

$$\delta\theta(H,\, t) = \delta\theta_{Max}\cos\left(2\pi f_{SAW} t + \psi_\theta\right) \quad (6.8)$$

$$\delta\varphi(H,\, t) = \delta\varphi_{Max}\cos\left(2\pi f_{SAW} t + \psi_\varphi\right) \quad (6.9)$$

In contrast to the MLD and PE effects, PMOKE is independent of the polarization orientation. On the other hand, the PE effect does not depend on the magnetic field. Therefore we can use these dependencies to distinguish the three effects from each other.

We expected to see two physical regimes: linear and nonlinear. The linear regime is when the magnetization precession amplitude is small and we observe it oscillating only at a single frequency equal to f_{SAW} (Equations 6.8 and 6.9). This is the case for most of the data taken at 60 K at a low power. For higher temperatures, it is easier to enter the nonlinear regime, where the magnetization oscillates with the large amplitude at $2f_{SAW}$ or in case of the magnetization switching at $f_{SAW}/2$.

6.2.1. Burst shape

Firstly, to confirm that the detected signal was due to the SAWs we measured the amplitude of the magneto-acoustic signal measured in TRPR as a function of the electrical burst delay $\Delta\tau$. For each delay, the signal was measured as a function of the optical delay, the amplitude was simply extracted by fitting the curve with the single sine function. Here, the purpose was not to disentangle magnetic and acoustic signals, that is why scans were taken for only one probe polarization ($\beta = 30°$) and at one value of the magnetic field (μ_0H=20 mT). The features of the optically measured signal were compared with the signal detected electrically (red solid line) with the second IDT through the inverse piezo-electric effect and visualized with an oscilloscope. In the electrically detected signal the electromagnetic radiation 400 ns burst arrived first, traveling at the speed of light. After $t_{trans} = \frac{d}{v_R} \cong 730$ ns, the acoustic echo arrived. The Rayleigh velocity was found around $v_R = 2780$ m/s. The width of the acoustic burst was bigger because of the lower velocity, which increases the transition time through the 25 digits. The burst-shaped excitation, with short enough *on* time ensured that those two signals were well separated from each other.

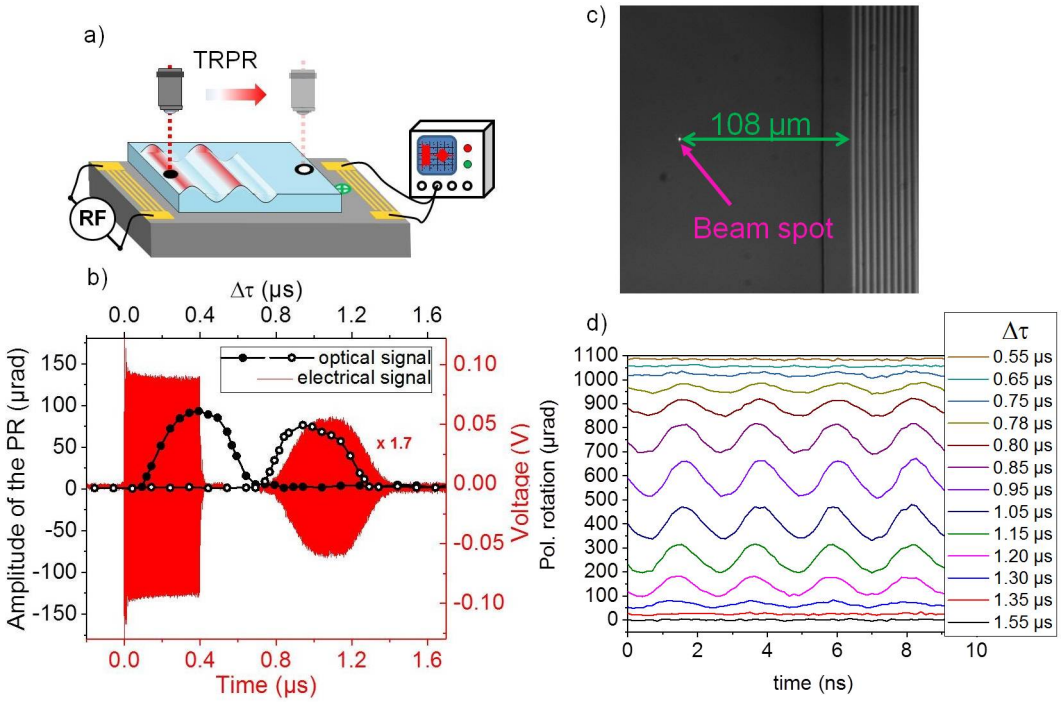

Figure 6.12.: (b) The red curve is the time trace detected electrically and the two dotted lines represent the amplitude of the TRPR signal detected in two places on the sample marked in the scheme in (a). The data was taken at 60 K with a magnetic field of 19.5 mT. (c) is the image of the IDT and the beam spot, where the data represented by empty dots in (b) was taken. The time scans for chosen electronic delays are plotted in (d) (vertically off-set for clarity).

First the probe beam was positioned 108 µm from the receiving IDT (Fig. 6.12 (a) and (b) - empty circles) - the precise position of the spots on the sample was found with an imaging system not shown in the set-up scheme (Fig. 6.12 (c)). Each point of the empty circle curve in Fig. 6.12 (b) indicates an amplitude of the oscillations observed in TRPR (Fig. 6.12 (d)). We can see that the shape of this curve corresponds to the acoustic echo detected with the IDT and it is almost overlapped with it since it was detected nearly at the same place. The rise and fall time is defined by the time the SAW excited with the last digits pair needs to travel through the whole IDT. The duration of a steady state of the burst was proportional to the excitation pulse width reduced by the rising and falling time. Moreover, we can conclude that the electromagnetic radiation does not trigger the precession. Then the probe beam was moved 67 µm from the emitting IDT (black spot in Fig. 6.12 (a)) and an identical profile was found, but this time closer to the excitation moment (Fig. 6.12 (b) full circles). The $\sim 20\%$ change of the amplitude of the peak is due to attenuation of the SAW by the magneto-elastic coupling. Moreover, we can find the Rayleigh velocity, since we know the distance between the two detection points: $\upsilon_R = 2880$ m/s. The small deviation from the value detected electrically originates from the measurement condition, in optically detected SAWs, the burst profile is discretized and it is difficult to give an exact arrival time.

6.3. Polarization dependence studies

6.3.1. Methodology

To study the magnetization precession excited with the SAW we performed a series of 12 ns - delay line time scans, probing the center of the burst for different orientations of the incoming linear polarization. Then we plotted the measured signal versus the polarization for each delay line position and we fitted it with the following expression:

$$\delta\beta = F_\theta + G_\varphi \cos 2\beta + H_{\varphi S} \sin 2\beta, \tag{6.10}$$

where

$$\begin{cases} F_\theta(H,\, t) = K\delta\theta(H,\, t) \\ G_\varphi(H,\, t) = 2V\delta\varphi(H,\, t)\cos 2\varphi_0(H) \\ H_{\varphi S}(H,\, t) = 2V\delta\varphi(H,\, t)\sin 2\varphi_0(H) + P_E S_{xx}(t) \end{cases} \tag{6.11}$$

Figure 6.13 (a) shows the TRPR signal for 6 orientations of the incoming beam polarization. The curves were taken for a SAW excitation frequency $f_{SAW} = 301$ MHz

at T= 60 K. The clear evidence of polarization dependence of the TRPR signal is also presented in the Figure 6.13 (b), for which data were extracted from the previous graph at a fixed time indicated by the green dashed line (Figure 6.13 (a)). The data points were fitted with the function 6.10. For zero magnetic field we see mainly the PE contribution of $\sin 2\beta$, since the magnetization is along the easy axis and if our experiment is well aligned the precession will not be excited (Equation 3.10). Moreover, when the polarization is at 0°, it is along k_{SAW} and we are not sensitive to the PE effect. The application of the magnetic field clearly modified the signal (red curve). The offset that appears corresponds to PMOKE which does not depend on polarization and the change of the phase is due to the presence of the Voigt effect. By performing the fitting for each time and fitting the extracted parameters $(F_\theta(H,t), G_\varphi(H,t), H_{\varphi S}(H,t))$ with a sinusoidal function of f_{SAW} we can obtain the amplitudes of Kerr $(f_\theta(H), F_\theta(H,\ t) = f_b + f_\theta(H)\cos(\omega_{SAW}t - \psi_f))$ and the Voigt $(g_\varphi(H), G_\varphi(H,t) = g_b + g_\varphi(H)\cos(\omega_{SAW}t - \psi_g))$ rotation and the photo-elastic part mixed with the Voigt effect $(h_{\varphi S}(H), H_{\varphi S}(H,\ t) = h_b + h_{\varphi S}(H)\cos(\omega_{SAW}t - \psi_h))$ at a given field value.

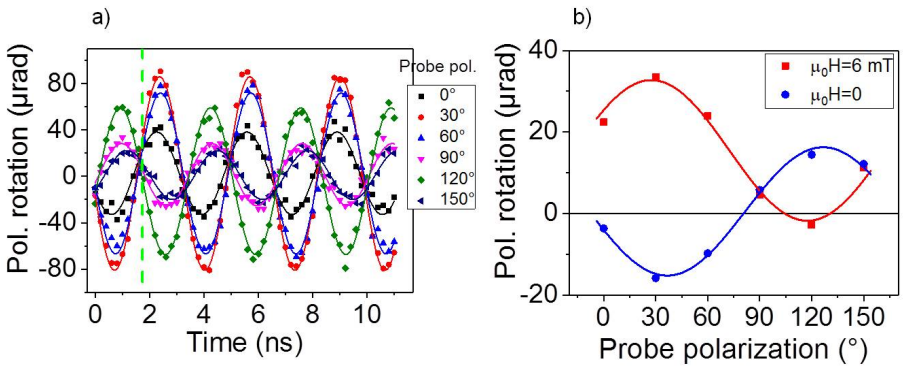

Figure 6.13.: (a) TRPR signal taken for six probe orientations of the polarization at μ_0H=6 mT, f_{SAW}=301 MHz, T=60K. (b) The polarization dependence of the signal at fixed optical delay (green dashed line in Fig. 6.13(a)) for two values of field.

6.3.2. Field dependence

To find how the parameters vary with the field we performed the polarization studies for field up to 36 mT. The amplitudes $f_\theta(H)$, $g_\varphi(H)$ and $h_{\varphi S}(H)$ are presented in Fig. 6.14 (a).

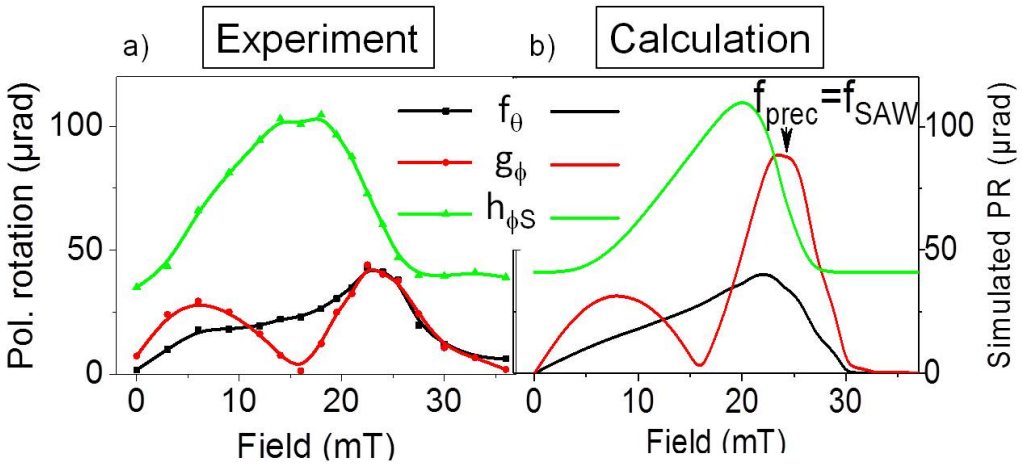

Figure 6.14.: (a) Field dependence of the three parameters f_θ, g_φ and $h_{\varphi S}$ for f_{SAW}=302 MHz and T= 60 K. To keep measurement time low we limited the polarization studies only to 6 polarizations. However, we checked that fit quality was not lower than for 18 polarization orientations. The time needed to take the curves from (a) is 6.5 h. (b) Calculated f_θ, g_φ and $h_{\varphi S}$ components. The values of fitting parameters used are K=18 mrad, V=0.8 mrad, PE=0.77 rad with $S_{xx} = 5.3\times10^{-5}$. The arrow in the graph indicates the field value for which $f_{prec} = f_{SAW}$.

Before discussing the obtained field dependence we will explicit the relations of these amplitudes with the magnetization and the strain components:

- $f_\theta = K\delta\theta_{Max}$ - the amplitude of out-of-plane magnetization precession multiplied by the Kerr constant,
- $g_\varphi = V\delta\varphi_{Max}\cos 2\varphi_0$ - the amplitude of in-plane magnetization precession multiplied by the Voigt constant and by cosine of $2\varphi_0$, φ_0 is giving the orientation of $\vec{\boldsymbol{m}}$with respect to $\vec{\boldsymbol{k}}_{SAW}$,
- $h_{\varphi S}$ - represents a mixed contribution of the amplitude of the in-plane dynamical magnetization and the longitudinal component of the SAW.

$f_\theta(H)$ increases monotonously up to $\sim$ 23 mT, where f_{SAW} is expected to be the closest to f_{FMR}, and decreases again to zero. $g_\varphi(H)$ has two maxima with an intermediate position at 16 mT for which $\cos 2\varphi_0(H) = 0$ and the magnetization is oriented at 45° to the easy axis (Equation 6.11) . In $h_{\varphi S}(H)$ signal we can see the two contributions, the constant offset is directly proportional to the field independent S_{xx} strain component and the signal on top of it to the Voigt effect. To confirm the $f_\theta(H)$, $g_\varphi(H)$ and $h_{\varphi S}(H)$ field dependence, we calculated the same components using the coupled equation system (Equation 3.9) and the measured sample parameters (Section 5.4.1). The results are presented in Fig 6.14 (b). They are in very good agreement with the data measured experimentally. To obtain comparable peak's height and width, a small dispersion of the uniaxial in-plane anisotropy was introduced.

As shown, the TRPR signal decomposition into the three elements is a technique which allows us to distinguish in-plane and out-of-plane dynamical magnetization component and S_{xx} strain component. The results obtained experimentally agree with the analytical solutions. Hence we used this approach to study the dependence of the magnetization precession amplitude upon various factors such as the SAWs frequency and power, and temperature.

6.3.3. The magnetization precession excitation efficiency versus SAW frequency

When the magneto-acoustic coupling occurs part of the SAW power is absorbed by the magnetic layer, when the magneto-acoustic coupling occurs and it is used to excite magnetization precession. It can be expressed as $P_{abs} = -\frac{\omega_{SAW}}{2}\Im\vec{\boldsymbol{h}}^*_{RF}\chi\vec{\boldsymbol{h}}_{RF}$, where χ is the tensor of magnetic susceptibility [13, 180, 114]. This general formula indicates that we can expect some f_{SAW} dependence of the absorbed power. Indeed this behavior was demonstrated experimentally by monitoring electrically the SAW amplitude attenuation versus magnetic field [180, 181, 13], it was also verified by us, see Fig. 6.22. Measuring optically the amplitude of magnetization precession we expected to observe a similar behavior: the largest amplitude oscillations for the highest f_{SAW}. In Figure 6.15 the three extracted components f_θ, g_φ and $h_{\varphi S}$ are plotted for 151, 301, 452 and 602 MHz excitation SAW frequencies.

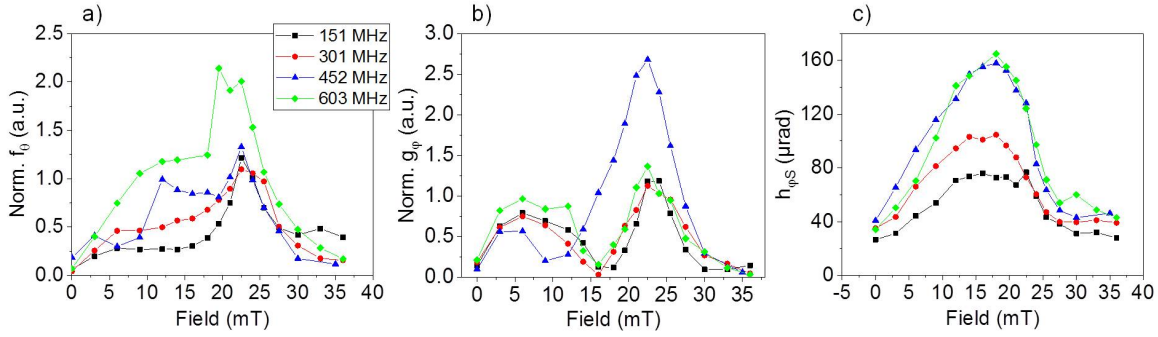

Figure 6.15.: Comparison of the field dependence of f_θ, g_φ and $h_{\varphi S}$ for the four excitation frequencies.

We have excited the 4 frequencies with equal voltage amplitudes ($P_{RF} = 24$ dBm≅251 mW), however it does not mean that the excited strains had the same amplitude since the IDT did not have a flat characteristic as you can see in Fig. 6.6 (b) and 6.7. Fortunately, we were able to use the PE (baseline of $h_{\varphi S}(H)$), which is a very good indicator of the amplitude of strain S_{xx}(as it will be shown after) to normalize the f_θ and g_φ curves. Such normalized f_θ showed a strong peak around 22.5 mT for all frequencies. This was because there was little dependence of the resonance field on SAW frequency since the FMR curve is very steep for the frequency range below

1 GHz (Fig. 5.8 (b)). Moreover, it is seen that only the amplitude for 602 MHz differ from the rest. The g_φ curves coincide for three frequencies 151, 301 and 602 MHz. The amplitude of g_φ is comparable with f_θ. Thus, the motion of the magnetization vector is that of an ellipse $|\delta\theta_{Max}| \ll |\delta\varphi_{Max}|$, because $K > V$. The static $\vec{\boldsymbol{m}}$ position φ_0 reached 45° around the same field value (∼16 mT), which is a good evidence of the temperature stability of our system and measurement repeatability. For 452 MHz, the two bumps were strongly asymmetric. It is from the $h_{\varphi S}$ curves dependencies that the f_{SAW} dependency was better observed. The baseline for $h_{\varphi S}$ was not adjusted to show the strain amplitude is not very different for the four frequencies. Again the curve for 452 MHz strays from the rest which may suggest that the experimental conditions for this frequency were different than for the rest.

6.3.4. Phase of the TRPR signal

The data which were not discussed up to now, but carry as important informations as the signal amplitude, is the phase. The relative phase of F_θ, G_φ and $H_{\varphi S}$ was obtained from the same fit used before to determine the variations of the precession amplitude with field. The three components have different phases as can be seen in Figure 6.16 (a), where $F_\theta(H,t)$, $G_\varphi(H,t)$ and $H_{\varphi S}(H,t)$ are plotted for $\mu_0 H = 6mT$.

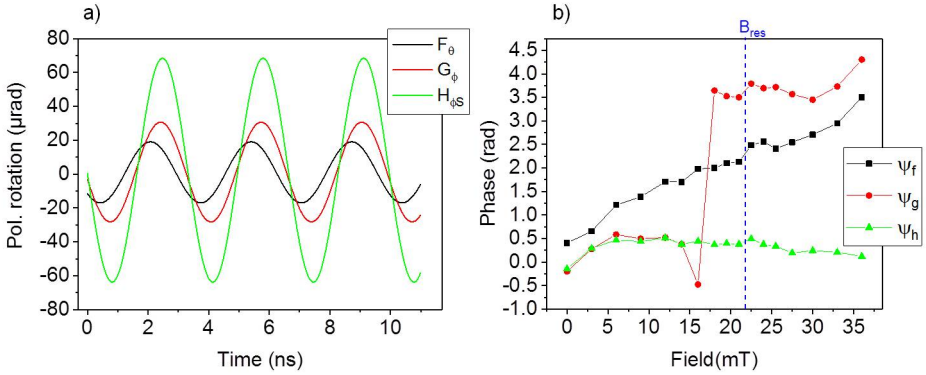

Figure 6.16.: (a) Time traces of F_θ, G_φ and $H_{\varphi S}$ for $\mu_0 H = 6\,mT$. (b) Dependence of F_θ, G_φ, $H_{\varphi S}$ phases on magnetic field for 301 MHz.

The extracted phase versus field is shown in Figure 6.16 (b) versus field. The phase of certain components shows very interesting features. The change of phase of the $H_{\varphi S}$ component is almost flat. This phase is difficult to analyze since we have the contribution of the two effects. In the two other components, we observe changes related to the magnetic field. The phase of F_θ changes monotonously by π. In the case of small damping we expect an abrupt change of phase by π at the point where $f_{SAW} = f_{FMR}(H)$. A higher damping ($\alpha = 0.05$) and small misalignment of the magnetic field in respect to the hard axis can make this change smoother. A similar π phase changed was observe by Janusonis *et al.* [182], where the magnetization

precession was excited with SAWs generated with the transient grating technique. In the phase of $G_\varphi(H,\, t)$ we also observe a π changed, however much sharper. This change is due to the rotation of the orientation of the static magnetization. When it traverses 45°, the phase changed by π since in our fitting procedure we forced the amplitude to be positive by adjusting the phase ψ_g.

6.3.5. Temperature dependence

At temperatures close to T_C, the magnetization orientation can be tuned more easily, with lower fields than at low temperature. The anisotropy field of the (Ga,Mn)As sample decrease with increasing the temperature (§ 5.4.1). In Fig. 6.17 we present f_θ, g_φ components normalized by the PE effect and $h_{\varphi S}$ components for 151 MHz at T= 60 K and 90 K.

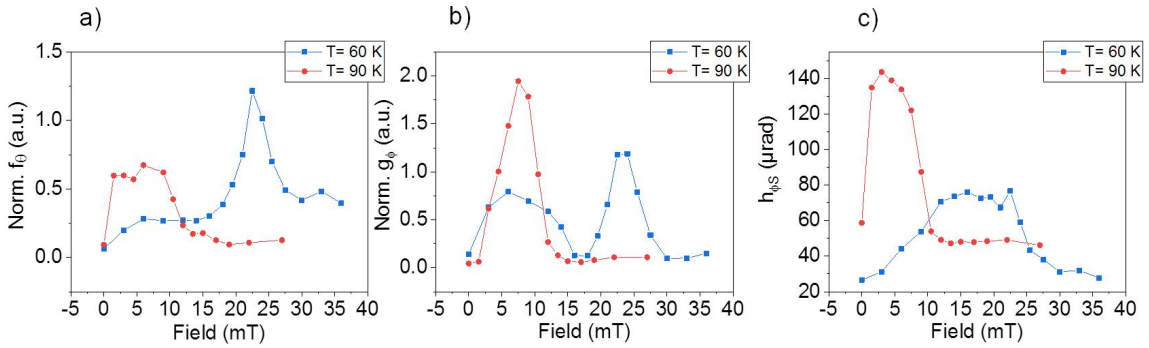

Figure 6.17.: f_θ, g_φ normalized by the PE effect and $h_{\varphi S}$ component for 60 K and 90 K, versus magnetic field for the sample excited with SAW at 151 MHz. The excitation power was 25 dBm.

The temperature influence is very well illustrated by the g_φ component. For 90 K we observe only a single, sharp peak. This peak can be identified as the second (high field) peak in the data taken for 60K. It means that even small field (∼1 mT) can bring magnetization at 45°. Similar features are observed in f_θ and $h_{\varphi S}$ signals. The peaks are much shifted to the lower fields. This is explained by the fact that the FMR frequency depends strongly on temperature as it was shown in Fig. 5.8. Indeed here we see a confirmation of that. The resonance field is lower by around 15 mT for 90 K.

In Figure 6.18, the results for three other frequencies are shown. The dependence looks similar to one observed for 151 MHz. The excitation power for 90 K was chosen to be relatively low (17 dBm= 50 mW) to avoid nonlinear effects, which will be discussed in the next paragraph.

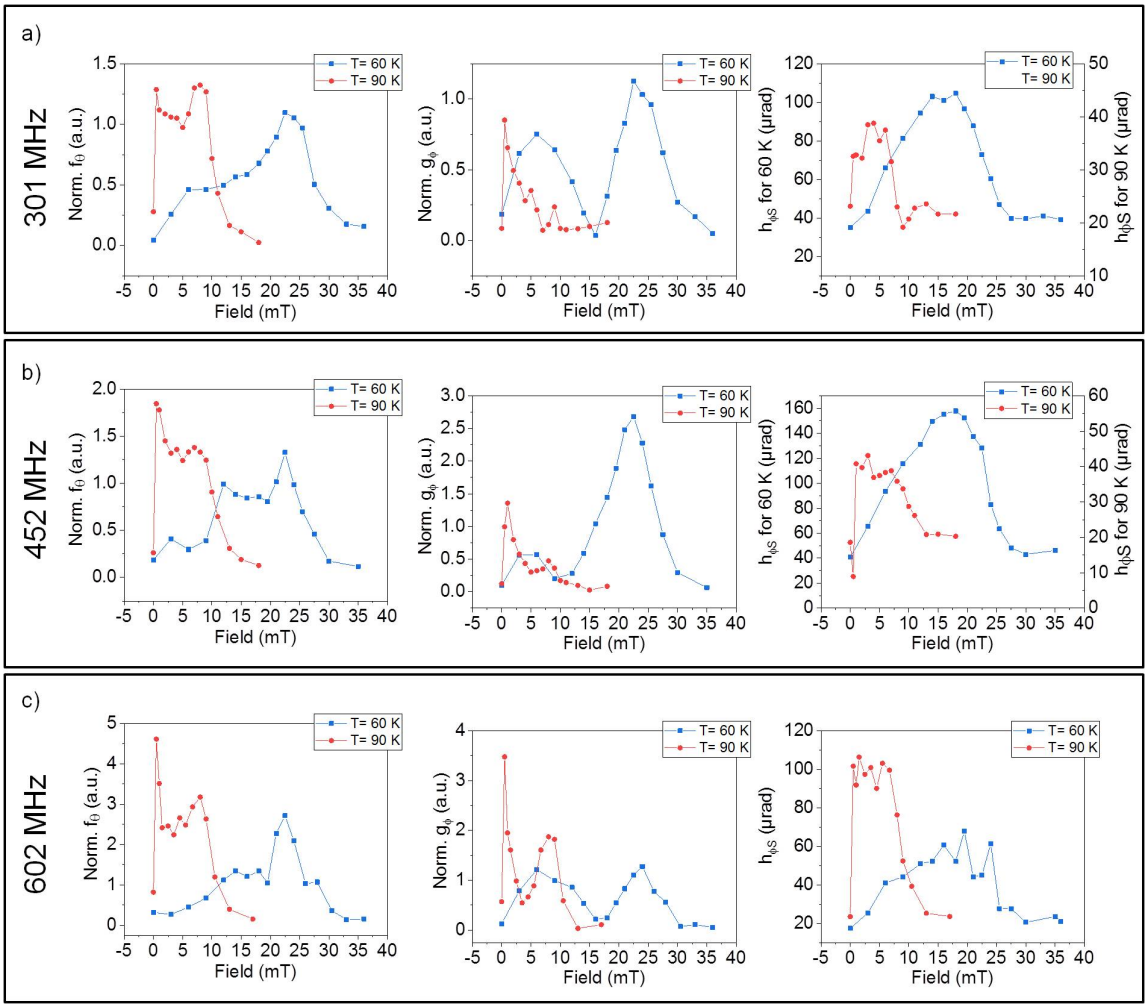

Figure 6.18.: The normalized f_θ, g_φ components and not-normalized $h_{\varphi S}$ plotted versus magnetic field for f_{SAW} = 301 MHz (a), 452 MHz (b) and 602 MHz for T= 60 K and T=90 K. The IDT was excited with 17 dBm for 452 and 602 MHz for both temperatures. For f_{SAW} = 301 MHz, the excitation power was 24 dBm and 19 dBm for 60K and 90 K, respectively.

6.3.5.1. Detection above the T_C

Furthermore, for the 452 MHz excitation frequency we have verified whether the baseline is really due to the PE effect. We increased the temperature above the Curie temperature to 130 K, and measured the amplitude of the oscillations as a function of β. The amplitude of the obtained signal showed a pure sinusoidal dependence (Fig. 6.19 a)), which means that only the photo-elastic effect was detected.

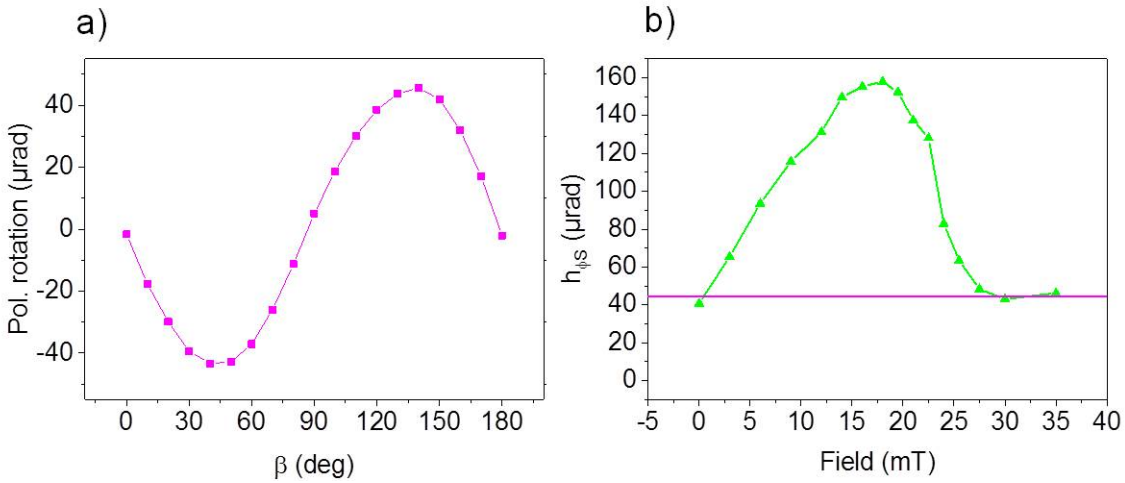

Figure 6.19.: (a) Amplitude of photo-elastic signal measured above the T_C for f_{SAW}= 452 MHz. (b) Amplitude of $h_{\varphi S}$ signal versus magnetic field at T= 60 K and for f_{SAW}= 452 MHz. The horizontal line indicates the amplitude of the signal from the left graph.

The amplitude of the signal extracted from Fig. 6.19 a), is plotted on top of the $h_{\varphi S}$ field dependence curve taken for the same excitation power and frequency at 60 K (Fig. 6.19 b)). The baseline perfectly overlaid with the PE signal measured above T_C. This clearly confirmed our predictions, that no magnetic contribution is detected above the T_C and that only below T_C, 2 other components are detected. If we would know the P_E for GaAs at low temperature, we could deduce the strain amplitude from Fig. 6.19 (a).

6.3.6. Power dependence

We also tested the efficiency of the precession excitation for different SAW powers. For electrically excited SAW, the power can be easily adjusted by tuning the voltage with which the IDT is excited. In Figure 6.20 we present $F_\theta(t)$, $G_\varphi(t)$ and $H_{\varphi S}(t)$ signals for f_{SAW} = 452 MHz, for three excitation powers: 17, 24 and 30 dBm. The $F_\theta(t)$ and $H_{\varphi S}(t)$ signal amplitudes increase with increasing SAW amplitude. However, the most interesting signal is presented in Figure 6.20 (b), where $G_\varphi(t)$ for the highest power oscillated at two frequencies: 452 MHz and double of this frequency. Since the 904 MHz frequency is not observed in $H_{\varphi S}(t)$ and disappears at high magnetic field, it can clearly be ascribed to the nonlinear precession of magnetization and not to the nonlinear excitation of SAW [183]. The component oscillating at 904 MHz is also present in the $F_\theta(t)$ signal but because of the ratio between two amplitudes is smaller ($\frac{f_\theta^{904MHz}}{f_\theta^{904MHz}+f_\theta^{452MHz}} \times 100 = 11\%$; $\frac{g_\varphi^{904MHz}}{g_\varphi^{904MHz}+g_\varphi^{452MHz}} \times 100 = 14\%$) and the phase between them is also different it is not so well visible as in $G_\varphi(t)$.

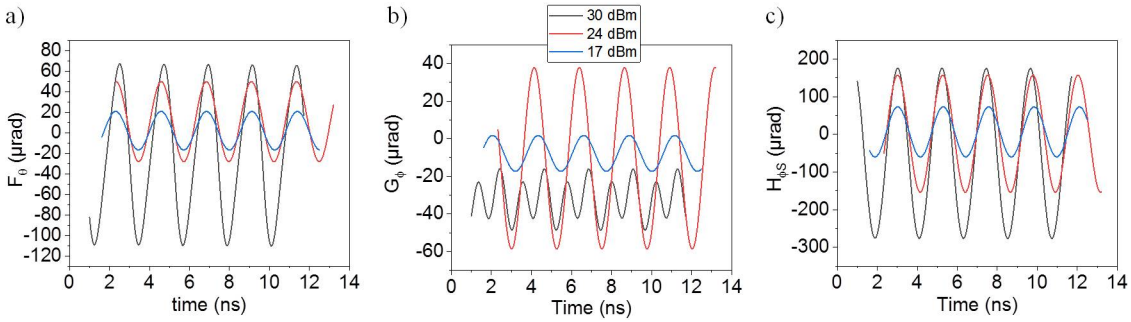

Figure 6.20.: $F_\theta(t)$, $G_\varphi(t)$ and $H_{\varphi S}(t)$ curves for $f_{SAW} = 452$ MHz for three SAWs excitation powers at 60 K and with a magnetic field of 16 mT.

The oscillation of magnetization at the double of the SAW frequency is the signature of a nonlinear precession regime, where magnetization oscillates around the axis located between the static magnetization position and the external magnetic field due to that the strong offset is observed. . This is attractive because we are close to the switching regime [21, 16, 113] and that a high frequency magnetization precession is excited with half lower SAW frequency. For example with the lithography method it is difficult to manufacture IDTs for SAW above 1 GHz (in order to excite magnetization precession) and this can be the way to overcome this limitation.

6.3.7. Back-action of the magnetization precession on SAW - SAWFMR

As already mentioned in this work, the magnetization precession can also be measured indirectly by measuring the changes of SAW amplitude and phase. The back-action of magnetization on SAW is described by the Equation 3.11, whose solution gives the wavevector k_{sol}. Then the changes of amplitude and phase are proportional to $exp(\Im[\Delta k_{sol}]\, l)$ and to $\Re[\Delta k_{sol}]\, l$, respectivly where l is the distance between the two IDTs [14]. The central part of an acoustic echo detected by the receiver IDT (Fig. 6.12) was fitted by a sinusoidal function to determine the phase and the amplitude of the signal. The data obtained for 602 MHz is plotted in Figure (6.21 red squares), where the broad peaks of the absorbed SAW and velocity changes are visible. The SAW amplitude and velocity decrease the most when the f_{SAW} is the closest to the magnetization resonance frequency. To show the multifunctionality of the developed set-up we set the probe beam inbetween the (Ga,Mn)As and the receiver IDT, on the 15 µm GaAs gap (Fig. 6.12 green crossed circle). The probe beam polarization was set at 45° where we expect to observe the strongest PE signal. Next, the magnetic field was scanned in the same way as for electrical detection of SAWFMR. They show similar dips as the SAWFMR. To ensure that the observed changes are due to the magnetic sample, we set the probe beam in the gap between the emitter IDT and the sample, where the SAW is just excited and has not yet

propagated through the magnetic layer. This time, the signal (empty triangles in Fig. 6.21) hardly shows any significant variation with the field.

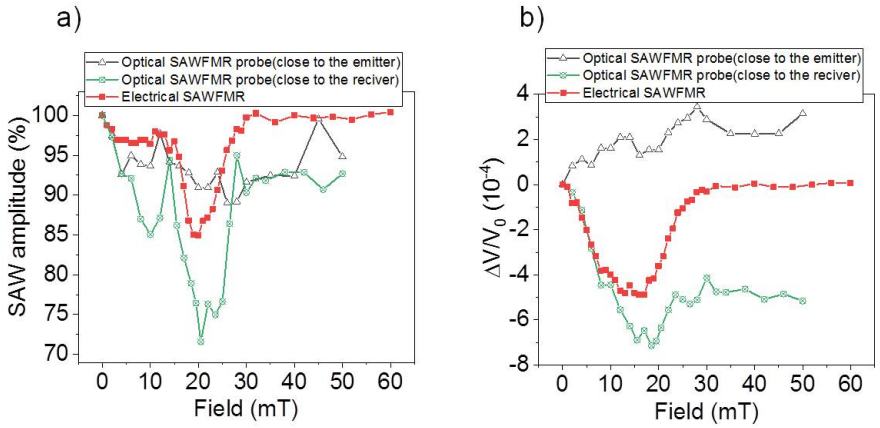

Figure 6.21.: Electrically detected SAWFMR versus optically detected SAWFMR. (a) Amplitude and (b) phase of the electrically and optically measured (in a two places) amplitude and phase variations of the SAWs.

As a result, a maximum attenuation of SAWs was observed for the same field in the signal detected electrically and optically closer to the receiver IDT. The signal detected electrically seems to be less noisy, on the grounds that it is faster to measure the electrical signal and it can be averaged over a few hundred times. In the phase variation of the optically detected signal we see that it did not return to its original position, probably we could not measure it, due to a small drift seen in the presented for data detected before the magnetic sample. It is not present in the signal measured on the receiver IDT, since the whole measurement was at least 10 times shorter.

6.3.7.1. Comparison between the optical detection of magnetization and the standard SAWFMR

To compare sensitivity and compatibility of the optical detection of magnetization and electrical SAWFMR techniques we will first consider the data presented in Figure 6.15 (a), since f_θ data is the easiest to interpret and compare to the SAWFMR.

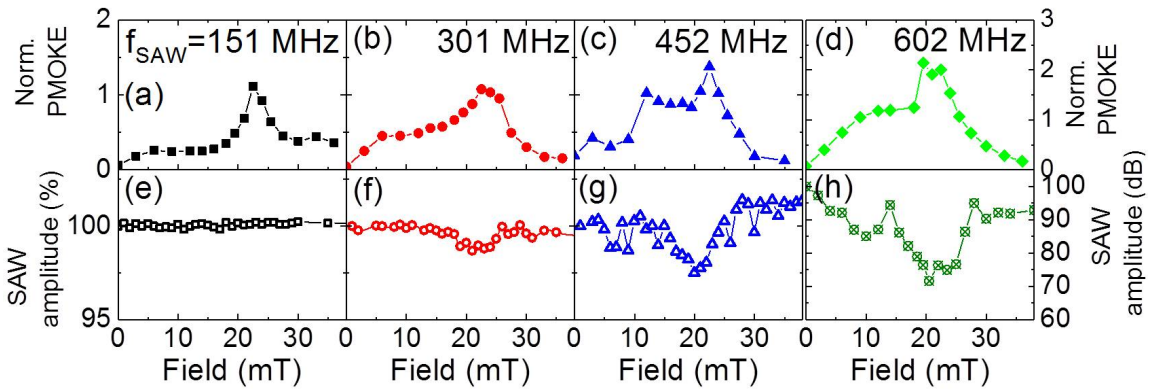

Figure 6.22.: Top panels: Field dependence of f_θ measured in TRPR for four SAW frequencies at 60 K. f_θ was normalized by the PE effect (baseline of $h_{\varphi S}$, not shown here). Bottom panels: electrically measured variation of the SAW amplitude with the magnetic field. The excitation powers were the same for optically and electrically measured signals.

In Fig. 6.22, the top row shows the amplitude of the out-of-plane precession measured optically and the bottom row is the variation of the SAW amplitude detected electrically. It is very clear that for SAWFMR measurements, when the amplitude changes are small (<1%), they are below the detection threshold. This happened for the low SAW frequency f_{SAW}= 150 MHz, where we were not able to detect any changes of the amplitude, while in PMOKE we can clearly observe a sharp peak at the resonance field. As f_{SAW} is higher the SAWFMR dip is more pronounced, but still seems to be more noisy than for optical measurements. With the TRPR measurement we are sensitive even to very small changes (a few µrad) because the signal was detected over a zero background.

6.3.7.2. Temperature dependence- electrical SAWFMR

To confirm the results observed with TRPR for the low (60 K) and high (90 K) temperature (Section 6.3.5), we performed similar studies with SAWFMR. Here we report the measurement taken for f_{SAW} = 452 MHz at several temperatures for excitation power 17 dBm.

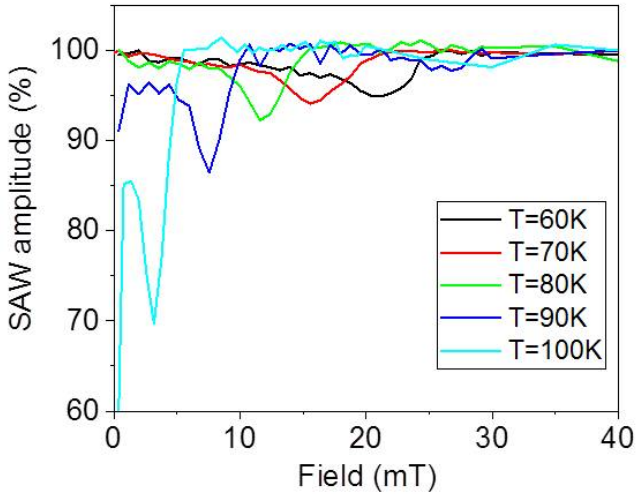

Figure 6.23.: The variation of the SAW amplitude versus magnetic field for a several temperatures. The SAW frequency was equal to 452 MHz and SAWs were excited with 17 dBm.

Figure 6.23 reveals similar features as already observed with optical SAWFMR, when the temperature is increased the resonance field is shifted to the lower field. Moreover, the dip is also bigger (increase of SAW attenuation) for higher temperatures which is consistent with f_θ.

6.3.8. Spatial mapping of the magnetic and acoustic waves

The final modification of our set-up, which was not discussed in the description of the experiment, was introduction of the XYZ piezo stage. This was made in the late spring 2018. The objective was mounted on a remotely movable stage with a range of 300 µm in all three directions. By using the stage, we could perform spatially resolved maps of SAWs or magnetization precession. In Fig. 6.24 (a), the 150 × 300 µm map of propagating SAWs with $f_{SAW} = 452$ MHz at room temperature (T=291 K) is presented. Only part of the image displays the SAW, because the map was taken at an edge of the excitation transducer, as it is shown in Fig. 6.24 (b), where the dashed line rectangle indicates the size and the position of the map.

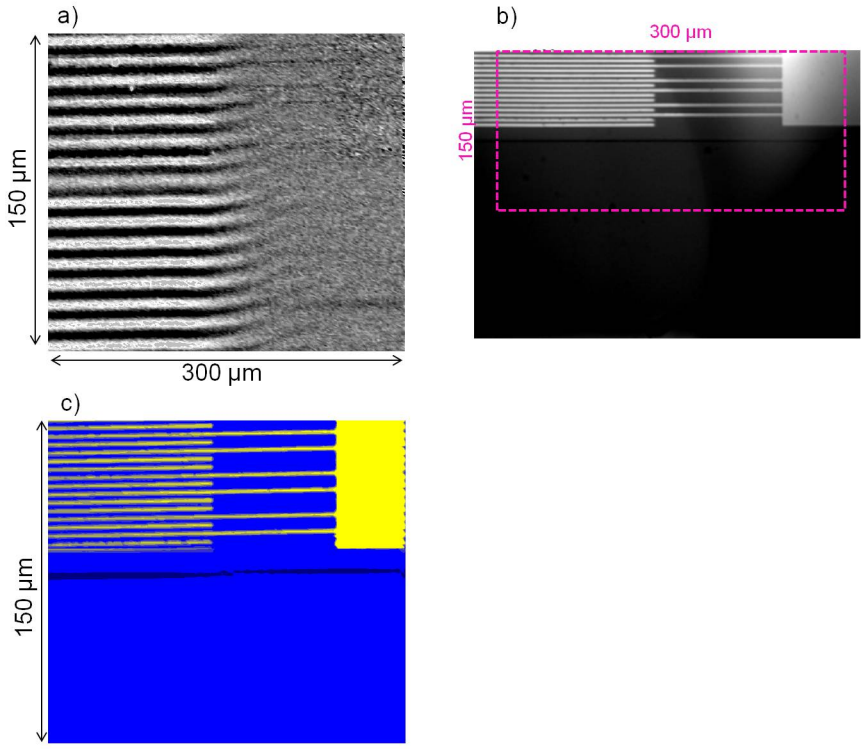

Figure 6.24.: (a) Map of the SAWs detected through the PE effect at T= 291 K. The SAW frequency was 452 MHz, excited with power of 17 dBm. (b) The sample image taken with the camera, The magenta rectangular mark where the (a) and (c) images were taken. (c) is the reflectometry map.

The SAWs generated in front of the IDT is a plane wave with $\lambda_{SAW} \simeq 9$ µm, while at the edge of the IDT the wavefront is not anymore flat. However, all data shown in this chapter was taken with the probe positioned in the center of IDT and we will not analyze this effect further. To confirm that the map was taken in the place of choice, we performed a reflectometry image, where one of the diodes of the detection bridge is blocked and changes of the reflected light intensity are monitored due to the different reflection index. As a result, we can identify the IDT and the part of its contact (yellow part of Fig. 6.24 (c)). The dark blue line indicates the border between the GaAs and GaMnAs layer. Moreover, the width of the IDT's digits is ∼1.9 µm and it is still very well resolved, which is another proof that we are not limited only to 600 MHz. In figure 6.24, the image for the three SAW frequencies f_{SAW}= 151 MHz, 302 MHz and 452 MHz are presented.

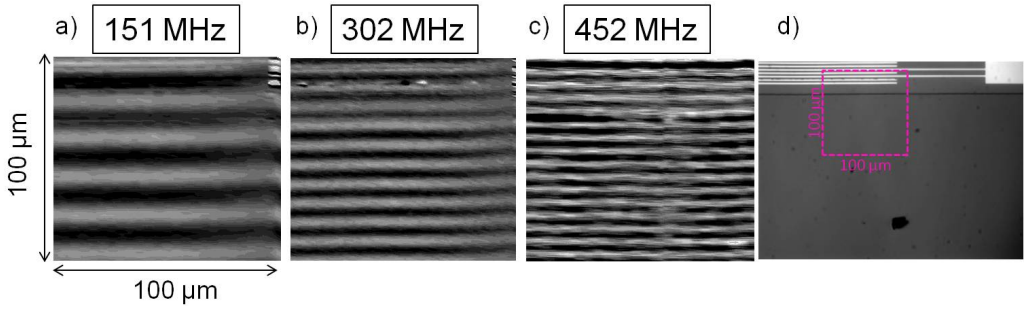

Figure 6.25.: Maps taken above T_C, using PE effect for three SAWs frequencies: (a) 151 MHz, (b) 302 MHz and (c) 452 MHz. In (d) the image of the sample with the magenta rectangle that shows were the three maps were taken.

After proving that all used SAW frequencies can be spatially resolved, we performed studies below T_C at T=60 K for f_{SAW}= 453 MHz to image the magnetization precession. However, now the magnetization and strain cannot be as easily distinguished from each other as before, since maps for at least 6 polarizations would need to be recorded and every line of the picture should be analyzed separately. This would take an enormous amount of time if we would like to do it for at least few field values. Instead, we probed the magnetization with the vertically polarized light (β=0°) where we are not sensitive to PE effect. Nevertheless, the measured signal was a mixture of the in-plane and out-of-plane magnetization dynamics.

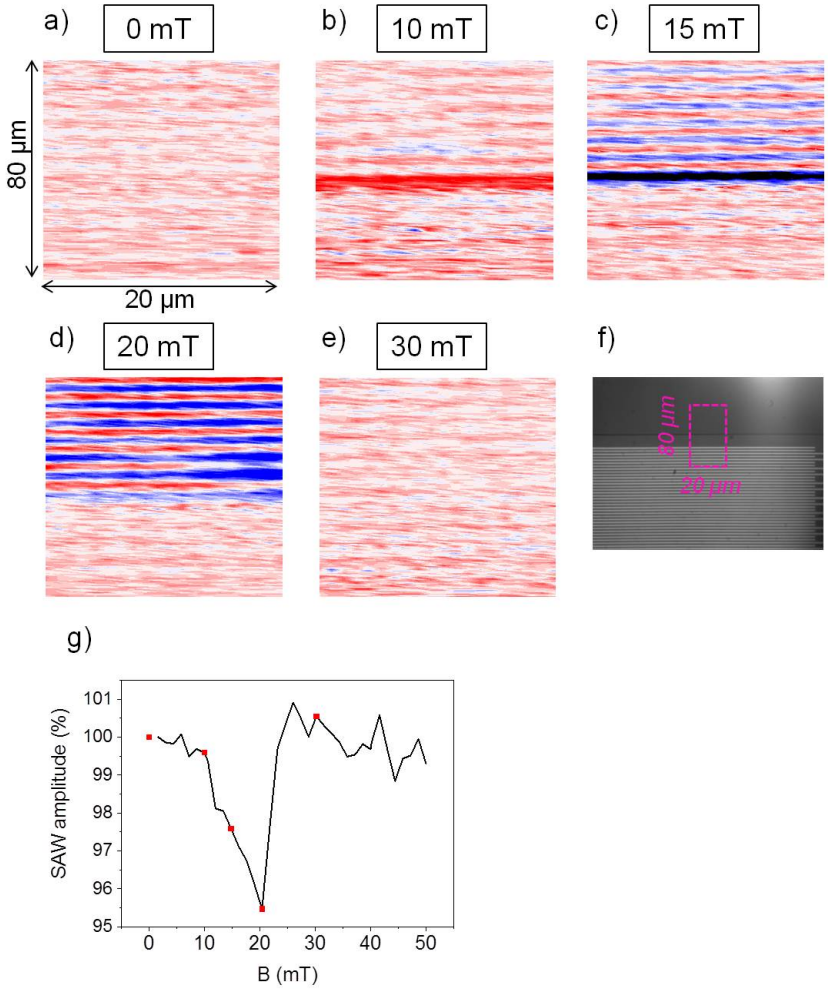

Figure 6.26.: Maps of in-plane and out-of-plane dynamic magnetization components taken at T=60K with beam polarized at β=0°. The magnetic field for which they were taken is indicated above each map. (f) shows the place on the sample were the maps were detected. (g) The SAWFMR curve, red spots indicate the fields for which maps were taken.

The results are presented in figure 6.26. For a zero magnetic field no magnetization precession is detected. Increasing progressively the field, the magnetization precession becomes more visible and at μ_0H=20 mT, where we are close to the resonance field (Fig 6.18 (b) and (g)) the wave is the most intense on the magnetic part of the sample and at 30 mT it disappears again. Furthermore, the wave-like signal was only detected at the GaMnAs part in contradiction to the measurement taken with β=45° where the wave was also detected on the GaAs and underneath IDT. This is another proof of the magnetic origin of the observed signal.

6.4. Perspectives

As perspectives for the developed set-up we would like to point out the studies of nonlinear effects, which were just briefly introduced in Section 6.3.6. However, a big number of data have been measured which showed very interesting features, which have not been understood so far. As a perspective, we also need to mention a time-resolved magnetization switching, which so far was observed only with use of the static MOKE for the excitation with SAWs [16, 180]. The trajectory of the magnetization switching could help us to improve the efficiency of this process. Also in this thesis, we did not show the dispersion maps of the magnetic and acoustic modes which are possible to perform in this set-up. Moreover, an interesting experiment might be to use the focusing IDT, for which by using the mapping system we could image how the magnetization precession changes with the power density of the SAW.

7. Spatial and dynamical control of magnetization with optically excited surface acoustic waves

Table of content

7.1. Introduction

In this chapter we will present results for optically excited SAWs in ferromagnetic metals on transparent substrates. The main challenge of this work was to select a sample with suitable magneto-elastic properties and to distinguish the magnetic signal from the acoustic signal. In contrast to SAWs excited with an IDT, the magnetization precession was so far not studied with SAWs excited with tightly-focused laser beam technique. Previously, only the use of unidirectional SAWs excited with the optical transient grating technique or excited in a patterned samples was reported (Section 4.2.2.2). However, since 2015 several articles reported magnetization precession excitation with BAWs generated in a configuration similar to our (Section 4.2.2.1). For both cases a clear evidence of resonance magneto-elastic coupling was

shown, confirmed by a strong dependence of the measured signal on the magnetic field.

Optical excitation of SAWs has several advantages over the electrical excitation:

- a sample surface being free of any metallic contacts,
- excitation of several wavevectors and frequencies,
- excitation in 360° directions,
- easier synchronization to optical detection,
- no need for a piezoelectric substrate.

Hence, the magnetization excitation can be easily studied at various places on the sample surface since preprocessing of samples is not required, which is attractive *e.g.* for samples with a spatially varying composition of a studied layer. Moreover, with this approach many specimens can be easily examined as it will be shown later in this chapter. In this project, SAWs are excited with a tightly focused beam (§ 2.5.1), thus broadband SAWs propagate in 2π directions. This allows us to study the magnetization precession excited with frequency and wavevector from a wide range, at any angle between the static magnetization and $\vec{\boldsymbol{k}}_{SAW}$ without tuning the excitation. Only the resonance condition has to be varied via magnetic field to reach a resonance and to increase the efficiency. The magnetization precession and strain dynamics are both probed optically. We use polarization rotation measurements as in the Chapter 6 to detect the magnetization dynamics, as well as interferometry measurements to measure the out-of-plane displacement.

The aim of the study was to determine if a clear signature of SAW-driven magnetization precession could be obtained with optically-generated SAWs as was observed for electrically-generated SAWs.

7.2. Set-up and samples

7.2.1. Set-up

The source of the pump and probe beams was a Ti:Sapphire (MAI-TAI Spectra) laser generating 100 fs long laser pulses of 800 nm wavelength, at a 78.8 GHz repetition rate (Fig. 7.1). At the output, the laser beam was splitted into two beams. The frequency of the pump beam was doubled with a BBO crystal. The pump beam was focused with a high numerical aperture (NA=0.9) objective to a spot of around 1 µm in diameter (at $1/e^2$) at one of the interfaces of the sample's layer. The wavelength of the excited SAW was directly proportional to the spot diameter [184]. That is why we have chosen to lower the wavelength of the pump, not of the probe. Additionally, the pump beam was modulated at 0.3 MHz or 1.8 MHz with an acousto-optic modulator (AOM). Before reaching the objective, the probe beam entered a mechanical

6×60 cm (12 ns) delay line. Furthermore, since the probe beam was used not only to detect the magnetization dynamics by the polarization rotation (PR) but also the SAW through interferometric measurements, 50% of the beam was directed to a interferometer reference arm (Michelson interferometer) while the other half was sent to the objective (NA=0.95) and the sample. Then, the reflected beam from the sample was detected by the optical bridge. The displacement - U_z was detected when the light reflected from the reference mirror interfered with the one reflected from the sample. Thus, the length of the two paths had to be equal. The PR signal was detected when the interferometric branch was blocked.

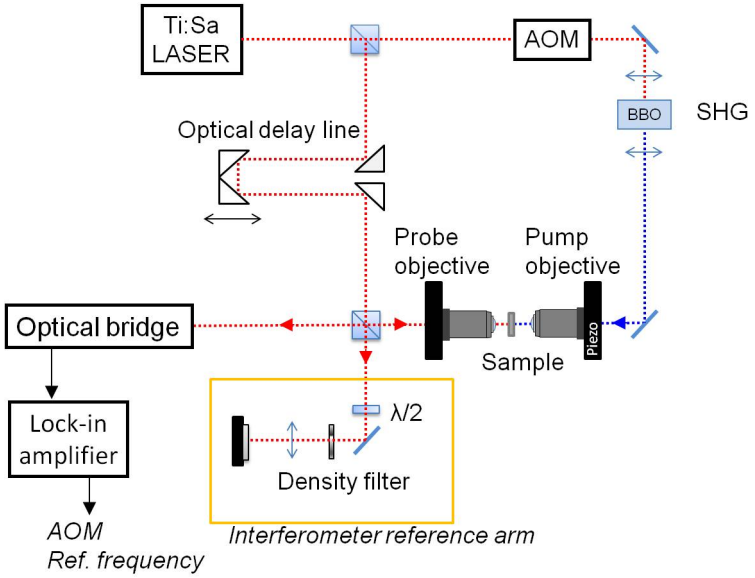

Figure 7.1.: Simplified scheme of the experimental set-up.

The proposed set-up has many advantages:

- As it was mentioned, we can perform both PR and interferometry measurements. We detect both signals in a reflection configuration, which is rare in this type of experiments. Most groups detect the polarization rotation in transmission and acoustic signals diffracted on the SAWs in reflection or all acoustic contribution also in transmission ([185, 186]). Nevertheless, the full reflection set-up was used before by our group to measure the magnetization precession induced by picosecond strain and more recently by Yahagi *et al.* to detect the magnetization precession and SAWs in patterned samples [20, 135].
- The SAW excitation can be either through the substrate or directly on the magnetic layer, which is important as it will be shown later.
- One or both objectives can be mounted on a XYZ piezo stage, which allows to perform 300 µm × 300 µm XY spatial maps or a 1D scan along a chosen line. If we combine that with the 12 ns delay line, we can take a dispersion map of either SAWs or spin waves as will be discussed later.

However, the use of two objectives with NA$\geqslant$0.9 puts certain constraints on the set-up. The working distance was 1.00+0.35 mm, which means that working at low temperature was impossible at least without a specialized cryostat. The limited space around the sample impedes the access to it, for example the magnetic field could not be applied as easily. Moreover, the excitation and the detection were on either side of the sample, therefore the sample's substrate had to be transparent. In conclusion, we worked with ferromagnetic metals on different transparent substrates (Section 5.4.2).

In contrast to the set-up used for the other project, except for the already mentioned temperature limitation, another difference was a broadband frequency spectrum excitation, with a central frequency relying on the focusing. Additionally, with a tightly focused laser beam we excited $\vec{\boldsymbol{k}}_{SAW}$ in 2π directions and so the polarization studies cannot be used to disentangle the magnetic and photo-elastic (strain - S_{rr} component) contributions as straightforwardly as in the previous chapter.

7.2.2. Measurement procedure

The excitation of magnetization precession with broadband SAWs differs significantly from the approach presented in the previous chapter, where a few hundred ns long acoustic bursts, at a single frequency, forced the magnetization to precess at this frequency. Here, the excitation is broadband. We expect that first magnetization precesses at SAW frequencies but after the passage of the SAW pulse, magnetization oscillates at its own resonance frequency, for a time defined by the damping parameter ($\tau_d = \frac{1}{\alpha 2\pi f}$). We expected to observe these features by using different tools offered by the set-up:

- time scans: the probe can be fixed at a given distance from the excitation point and then the optical delay is varied. By performing this measurement in PR and interferometry we expected to observe remarkable differences, such as different average frequencies and different damping of the oscillations.
- line scans: for this measurements delay line position was set but we could scan for example a radial line by moving the probe or pump objective. We expected to see similar results as for the time scans. Moreover, by performing the 1D FFT we obtained the response in the frequency and k space domain for time and line scans respectively.
- maps: instead of scanning only one line we could scan a large number of lines to obtain a 2D image of acoustic waves or magnetic waves. In the interferometric map we expected to see a *slowness curve*, possibly showing the anisotropy of the SAW velocity while in the PR map the symmetry breaking defined by an angle between the$\vec{\boldsymbol{k}}_{SAW}$ and $\vec{\boldsymbol{m}}$ should appear (see next section).
- dispersion curve: to obtain a dispersion curve either of magnetic or acoustic waves, we needed to take line scans at different optical delays (Fig. 7.2) and

process the obtained data with a 2D FFT. From that, we expect to observe a dispersion curve of the SAWs and for data taken in PR, part of the dispersion curve of magnons for places where it crosses the dispersion curve of phonons (Fig. 3.2).

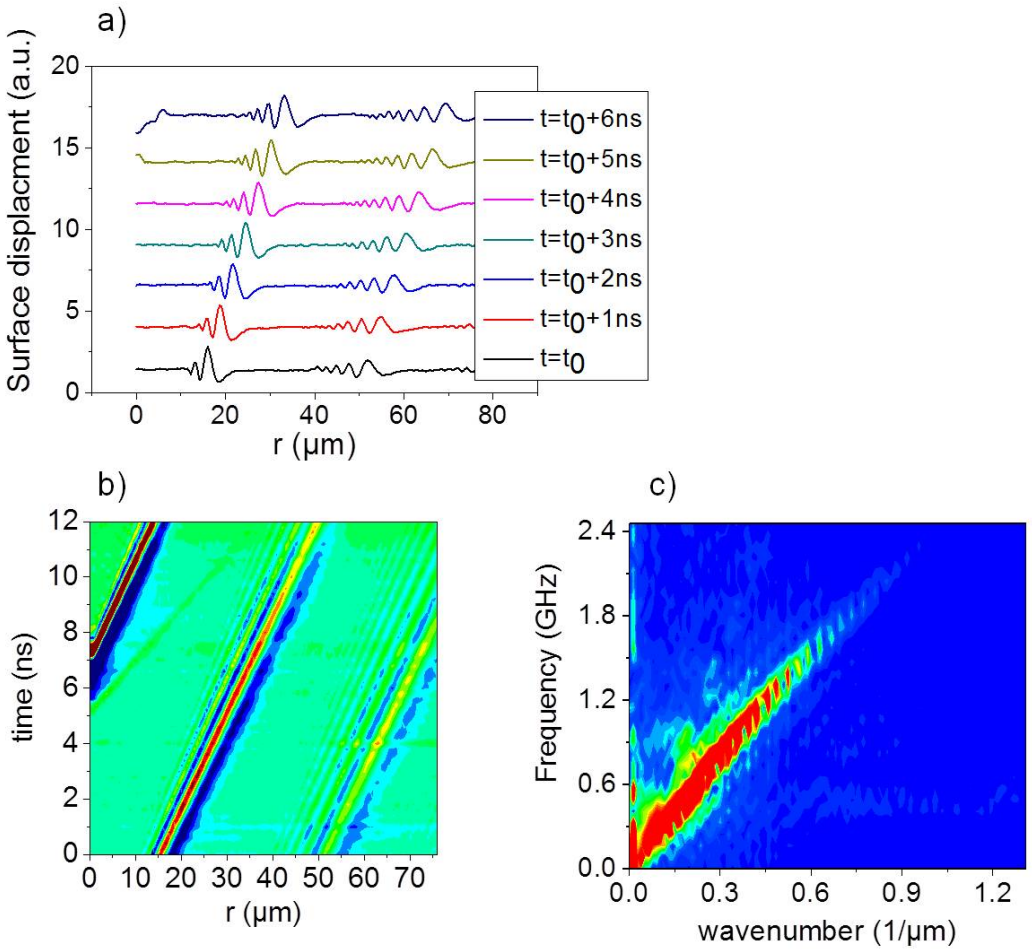

Figure 7.2.: (a) Exemplary line scans measured in the interferometry set-up at different delays between pump and probe (offset for clarity). When enough number of these scans were taken, they can create the time and space map as it is presented in (b). Performing the 2D FFT of (b) the dispersion relation in this case of the SAWs can be obtained (c) .

Since the FFT was a frequently used tool to analyze the data in this project, it is worth mentioning that we used a Hanning window.

7.2.3. Expected polarization rotation map symmetry

We expect that three axes would break the isotopic symmetry: the probing linear polarization plane, $\vec{k}_{SAW}$ and the static magnetization. The detected signal should have magnetic and non-magnetic contributions.

7.2.3.1. Magnetic origin

To calculate the signal originating from the magnetization we will start from LLG equation. After T. L. Linnik [79], we neglected the damping and introduced the LL equation in spherical coordinates (Equation 1.16) in the presence of dynamical strains:

$$\begin{cases} \delta\dot{\varphi} = \frac{\gamma}{\sin\Theta_0}\left[\frac{\partial^2 f}{\partial\Theta^2}\delta\Theta + \frac{\partial^2 f}{\partial\Theta\partial\varphi}\delta\varphi + \frac{\partial^2 f}{\partial\Theta\partial S_{xx}}\delta S_{xx} + \frac{\partial^2 f}{\partial\Theta\partial S_{yy}}\delta S_{yy}\right. \\ \left. + \frac{\partial^2 f}{\partial\Theta\partial S_{zz}}\delta S_{zz} + \frac{\partial^2 f}{\partial\Theta\partial S_{xz}}\delta S_{xz} + \frac{\partial^2 f}{\partial\Theta\partial S_{yz}}\delta S_{yz} + \frac{\partial^2 f}{\partial\Theta\partial S_{xy}}\delta S_{xy}\right] \\ -\delta\dot{\Theta} = \frac{\gamma}{\sin\Theta_0}\left[\frac{\partial^2 f}{\partial\varphi^2}\delta\varphi + \frac{\partial^2 f}{\partial\varphi\partial\Theta}\delta\Theta + \frac{\partial^2 f}{\partial\varphi\partial S_{xx}}\delta S_{xx} + \frac{\partial^2 f}{\partial\varphi\partial S_{yy}}\delta S_{yy}\right. \\ \left. + \frac{\partial^2 f}{\partial\varphi\partial S_{zz}}\delta S_{zz} + \frac{\partial^2 f}{\partial\varphi\partial S_{xz}}\delta S_{xz} + \frac{\partial^2 f}{\partial\varphi\partial S_{yz}}\delta S_{yz} + \frac{\partial^2 f}{\partial\varphi\partial S_{xy}}\delta S_{xy}\right] \end{cases} \tag{7.1}$$

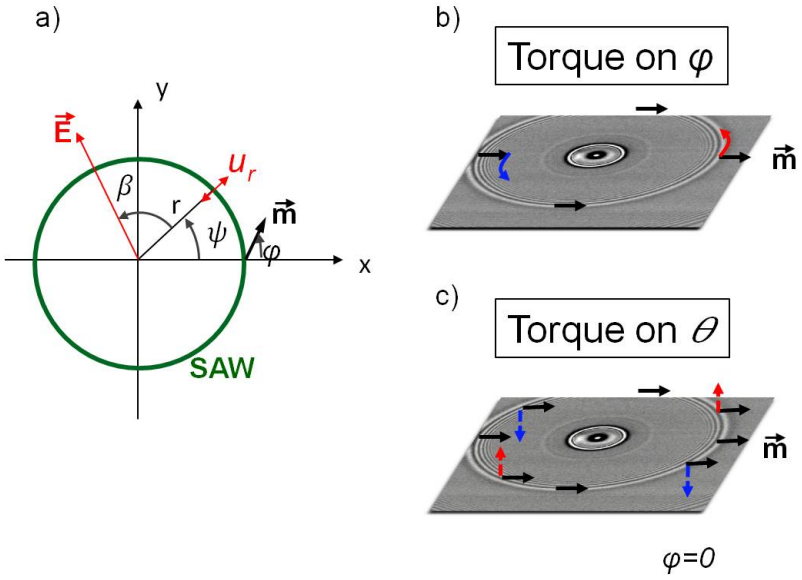

Figure 7.3.: (a) Polar coordinates system with the orientation of U_r SAW displacment and magnetization. Effect of $\delta\dot{\varphi}$ in-plane (b) and $\delta\dot{\Theta}$ out-of plane (c) torques. ψ denotes the orientation of $\vec{k}_{SAW}$ and φ of the magnetization.

where $f = \frac{F}{M_S}$ is the sum of the magnetocrystalline and magneto-elastic contributions to the free energy F for FeGa [29]:

$$f_{FeGa}^{MCA+MEl} = -\mu_0 H[\cos\Theta\cos\Theta_H + \sin\Theta\sin\Theta_H\cos(\varphi-\varphi_H)] + \frac{\mu_0 M_s}{2}\cos^2\theta - K_{2\perp}\cos^2\theta$$

$$+\frac{K_{4\parallel}}{4}\sin^2 2\varphi\sin^4\theta - K_{2\parallel}\sin^2\left(\varphi-\frac{\pi}{4}\right)\sin^2\Theta + B_1\left[\left(\cos^2\varphi S_{xx} + \sin^2\varphi S_{yy}\right)\sin^2\Theta + \cos^2\Theta S_{zz}\right]$$

$$+B_2\left(\sin^2\Theta\sin 2\varphi S_{xy} + \sin 2\Theta\sin\varphi S_{yz} + \sin 2\Theta\cos\varphi S_{xz}\right) \tag{7.2}$$

one can find the following formulas for the strain induced torques, in the case of in-plane magnetized samples ($\Theta_0 = \frac{\pi}{2}$):

$$\begin{cases} \dot{\delta\varphi}(H,\ t) = -\gamma 2B_2\left[\cos\varphi\delta S_{xz} + \sin\varphi\delta S_{yz}\right] + \gamma f_{\Theta\Theta}\delta\Theta \\ -\dot{\delta\Theta}(H,\ t) = \gamma B_1\sin 2\varphi\left(-\delta S_{xx} + \delta S_{yy}\right) + 2B_2\cos 2\varphi\delta S_{xy} + \gamma f_{\varphi\varphi}\delta\varphi \end{cases} \tag{7.3}$$

For convenience the strains might be rewritten in cylindrical coordinates (Fig. 7.3 (a)):

$$\dot{\delta\varphi}(H,\ t) = -\gamma 2B_2\delta S_{rz}(t)\cos\left(\varphi-\psi\right) + \gamma f_{\Theta\Theta}\delta\Theta \tag{7.4}$$

$$-\dot{\delta\Theta}(H,\ t) = \gamma\delta S_{rr}(t)\left(-B_1\sin 2\varphi\cos 2\psi + B_2\cos 2\varphi\sin 2\psi\right) + \gamma f_{\varphi\varphi}\delta\varphi \tag{7.5}$$

Here the observation point is located at $(r,\ \psi)$ in the (x, y) plane (Fig. 7.3 (a)). Equation 7.4 shows that the δS_{rz} strain component acts as an in-plane torque on the magnetization and can give the symmetry presented in Figure 7.3 (b). When the static magnetization is along $\vec{\boldsymbol{k}}_{SAW}$ ($\varphi = \psi$), the cosine is equal to 1 and when it is opposite to it ($\varphi = \psi + \pi$) cosine is equal to -1. This gives an opposite phase across the epicenter. Moreover, for $\varphi - \psi = \frac{\pi}{2}$ or $-\frac{\pi}{2}$, no torque is exerted and we expect not to observe any signal. So we should observe a 2-fold symmetry that rotates with static $\vec{\boldsymbol{m}}$ position (Fig. 7.3 (b)).

Equation 7.5 gives the out-of-plane torque. When $B_1 = B_2$ (isotropic magneto-elastic coupling) this torque has a $\sin 2\left(\varphi-\psi\right)$ dependence. It depends solely on the angle between $\vec{\boldsymbol{m}}$ and $\vec{\boldsymbol{k}}_{SAW}$. It gives a qudrupole-like symmetry for the $\delta\Theta$ and $\delta\varphi$ components (Fig. 7.3 (c)). If $B_1 \neq B_2$ (cubic symmetry), the symmetry is the

same but is rotated with respect to $\vec{\boldsymbol{m}}$. For thin $Fe_{80}Ga_{20}$ samples we have B_1= 5 MJ/m^3 and B_2= 3 MJ/m^3 [29].

In polarization rotation we expect to observe the symmetry, which will be a linear combination of the symmetries introduced by the two torques. For $\varphi = 0$, the out-of-plane component of magnetization dynamics can be written as follows:

$$\delta\Theta \cong -aB_2\delta S_{rz}(t)\cos\psi + bB_2\delta S_{rr}(t)\sin 2\psi \tag{7.6}$$

where a and b are prefactors which depend on material parameters, in particular on ω_0, which includes the magnetization static position, and the anisotropy constants. They put different weights on the two components. We can expect the bigger influence of the second term because the δS_{rz} is very small close to the surface. Since with PMOKE we are mainly sensitive to the out-of-plane magnetization component in metals, the polarization rotation will be $\delta\beta = K\delta\Theta$.

7.2.3.2. Non magnetic contribution

Since we observed a clear PE contribution to the PR signal for SAWs generated electrically (Chapter 6), it is reasonable to consider the same nonmagnetic contribution in this project. Recalling Equation 5.40, the signal will vary like $\sin 2\beta$, where β is the angle between the polarization $\vec{\boldsymbol{E}}$ vector and $\vec{\boldsymbol{k}}_{SAW}$. As a result, we will get the quadrupole symmetry as it is presented in Figure 7.4.

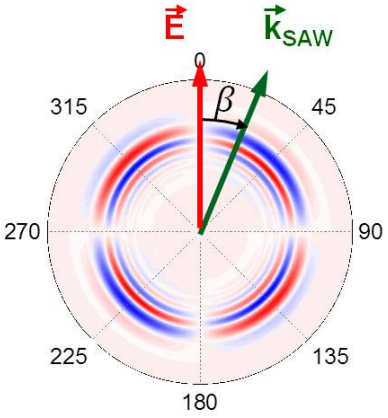

Figure 7.4.: The calculated photo-elastic contribution in PR signal.

This pattern should rotate, when the incoming polarization is rotated.

7.2.4. Samples (guidelines)

In this project we worked with four different samples. The samples differ from each other in magnetic layer and substrate. The studied samples were:

- FeGa (88 nm) on STO (0.5µm),
- Nickel (100 nm) on glass (0.3 µm),
- FeGa (120 nm) on Sapphire (0.5 µm),
- Cobalt (100 nm) on Sapphire (0.5 µm).

The FeGa was chosen because of its good magnetostrictive properties. However, the precession frequency was quite high, at least for the FeGa on STO sample (>3 GHz at μ_0H= 0 mT). It was lower for FeGa on Sapphire (<2 GHz at μ_0H= 0 mT) and even lower for Nickel on glass (<1 GHz at μ_0H= 0 mT). However, the Rayleigh velocity in glass is small, that is why the peak of the SAW frequency spectrum was around 0.8 GHz. The last sample, Cobalt was selected for it is known as a highly magnetostrictive material and the Sapphire has one of the highest SAW velocity which allowed to excite SAWs above 2 GHz.

We also used two nonmagnetic samples to confirm the magnetic origin of the measured signals in PR: Aluminium on glass and Titanium on Sapphire.

We need to underline, that since the described experimental set-up belongs to Laurent Belliard with whom we collaborated on this project, we could work only in short campaigns. In total, during 3 years, we had 4 campaigns each lasting from 2 to 4 weeks. These campaigns did not yield clear proofs of the magneto-elastic coupling therefore the results will be presented in chronological order, to show the difficulties that we have encountered and how we improved our measurements.

7.3. Results

7.3.1. FeGa in zero-field: high precession frequency

During our first campaign, we studied a magnetically isotropic, epitaxial 88 nm thick FeGa sample on STO substrate in zero field (Section 5.4.2.2). The BBFMR measurement shows that the resonance frequency in zero magnetic field was rather high >3GHz (fig. 7.5).

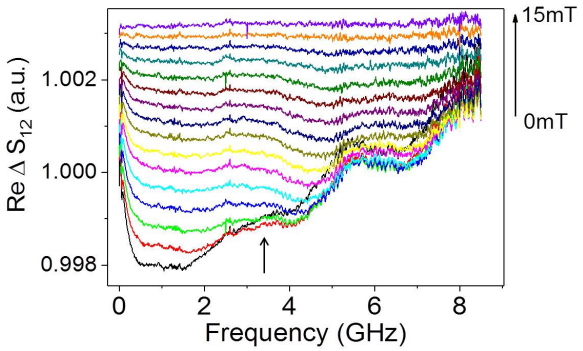

Figure 7.5.: Broadband FMR measurement of FeGa sample on STO. The resonance frequency in zero field is difficult to locate but was above 3 GHz.

However, FeGa is known as a good magnetostrictive material and we expected to see the coupling even if the frequency matching is not optimal [187]. We will start by analyzing the SAWs optically excited on this sample. In Figure 7.6, the interferometric map of the generated SAWs is presented. The bright central spot corresponds to the place where the pump laser pulse arrives to excite acoustic waves.

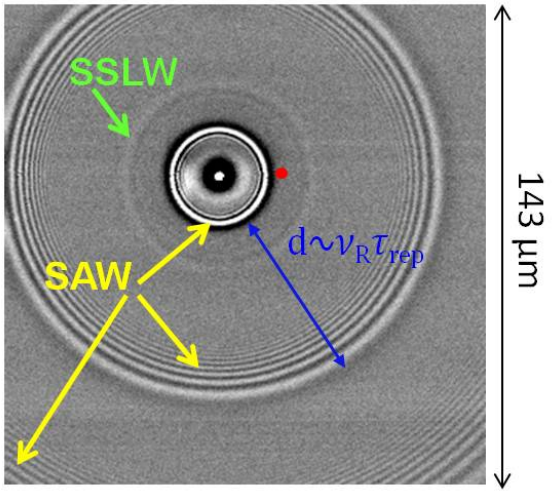

Figure 7.6.: FeGa on STO: Interferometry map of optically excited SAWs. The Rayleigh velocity was around v_R =4.1$\frac{km}{s}$.

The signal is isotropic. The inner and outer rings are the SAWs, they are separated by the distance determined by the laser repetition rate and sound velocity. From the outer ring, we can already say that the propagating SAWs are broadband and dispersive since we see many fringes. Between the two rings, we can see another weaker one, this is the surface skimming longitudinal wave (SSLW). This wave propagates just below the surface with the velocity of the longitudinal sound wave

[188]. Next, we performed a time scan of the SAW. The probe beam was fixed at the point indicated by the red spot in Fig. 7.6. The result is presented in Figure 7.7 (a). First, the acoustic wave with the longer period (lower frequency) arrives, because the velocity for higher frequencies is lower, since they are more sensitive to the FeGa film. In Fig. 7.7 (b) an FFT of the time profile is presented.

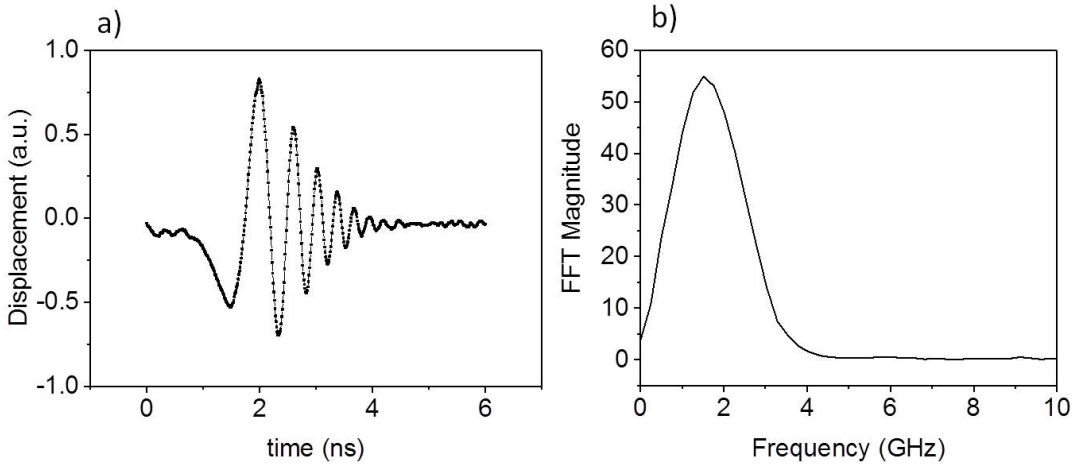

Figure 7.7.: Isotropic FeGa on STO: (a) Time trace of out-of-plane displacement of SAWs. (b) The frequency spectrum from the FFT.

The frequency spectrum was 2 GHz wide at FWHM with the central frequency around 1.5 GHz. This frequency depends strongly on the sound velocity in the substrate and the spot diameter. After the SAW characterization, we performed Kerr studies. The map of the PR measurement is presented in Fig. 7.8 (b). The red and blue color scale was set for better contrast of the wave phase. The picture is conspicuously different from the one taken with the interferometry set-up. This time, the signal is anisotropic in the ring and in the center. The ring was found at the same distance from the epicenter as in the interferometry. In two diametrically opposite parts the ring is clearly weaker than in the other parts. Moreover, by taking a closer look we can see that at the opposite sides of the epicenter, the phase in the ring has changed. The epicenter has a two fold symmetry, with the axis crossing the ring in the *weak* part. The obtained symmetry resembles the one expected from the torque on φ (S_{rz} component).

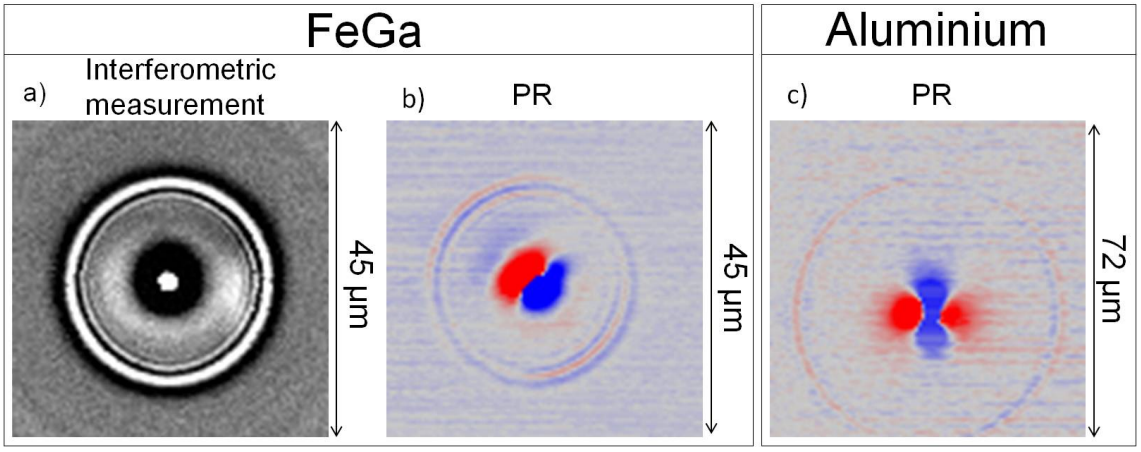

Figure 7.8.: Interferometric (a) and PR (b) map taken on FeGa on STO and PR map for Aluminium sample on glass (c). The probe pulse delay with respect to the pump pulse in the case of maps of FeGa was $\Delta\tau_{p-p} = 3.7$ ns and for Aluminium: $\Delta\tau_{p-p} = 7.5$ ns.

Since at that time a magnetic coil was not implemented we performed the same PR map for a nonmagnetic sample (100 nm on a glass substrate) to test the magnetic origin of the signal (Fig. 7.8 (b)). For Aluminium, the symmetry of the ring was very similar, the signal was slightly lower. Although, the signal in the epicenter was different, it was difficult to analyze it, since the temperature was very high there. Because we observed a similar signal for the Aluminium sample, it was obviously not a good sign and since the FMR frequency was almost out of the excitation frequency range for FeGa sample we concluded that the conditions were not fulfilled to observe magneto-elastic coupling. We decided to choose samples with lower FMR frequency at zero field.

7.3.2. Nickel in zero-field: low precession frequency

From the first campaign, we learned that the frequency coupling might be critical for the magnetization precession excited with SAWs. Therefore, we chose a sample with low FMR frequency in zero magnetic field. This sample was a 100 nm sputtered Nickel film on a glass substrate (we have tested also 20 and 300 nm thick Nickel films but the results will not be shown here) (Section 5.4.2.1). Since the substrate was different from that for FeGa, the frequency spectrum of the generated SAWs was also slightly different (υ_R for glass is lower than for STO). In Figure 7.9 (a) and (b) the time profile of the excited SAWs and its FFT are presented. The SAW peak frequency was clearly lower than before, around 0.8 GHz. To check how it was located on f_{FMR}(H) curve, we plotted the data extracted from the BBFMR measurements (Fig. 5.2 (b) and (c)) in Fig. 7.9 (c).

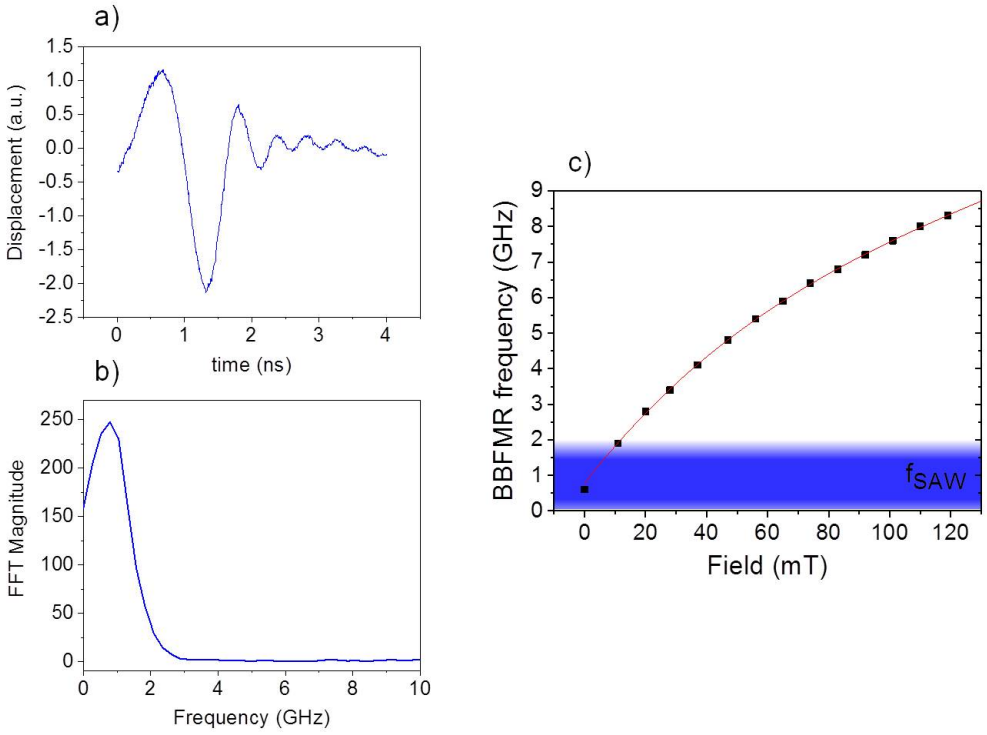

Figure 7.9.: (a) The time profile of the optically excited SAWs for a 100 nm Nickel sample. (b) The frequency content of the SAWs obtained with FFT. (c) f_{FMR} dependence on magnetic field measured with the BBFMR. The blue bar marks the frequency band of the SAW from graph (b).

By overlapping the frequency f_{FMR}(H) with the generated SAWs frequency we can see that for the magnetic field below 20 mT we can expect to see strong magneto-acoustic coupling.

For this sample, we have tested two experimental configurations. We will start by presenting the data for the same configuration as for FeGa on STO where the pump beam excites SAWs through the substrate (Fig. 7.10 (a)).

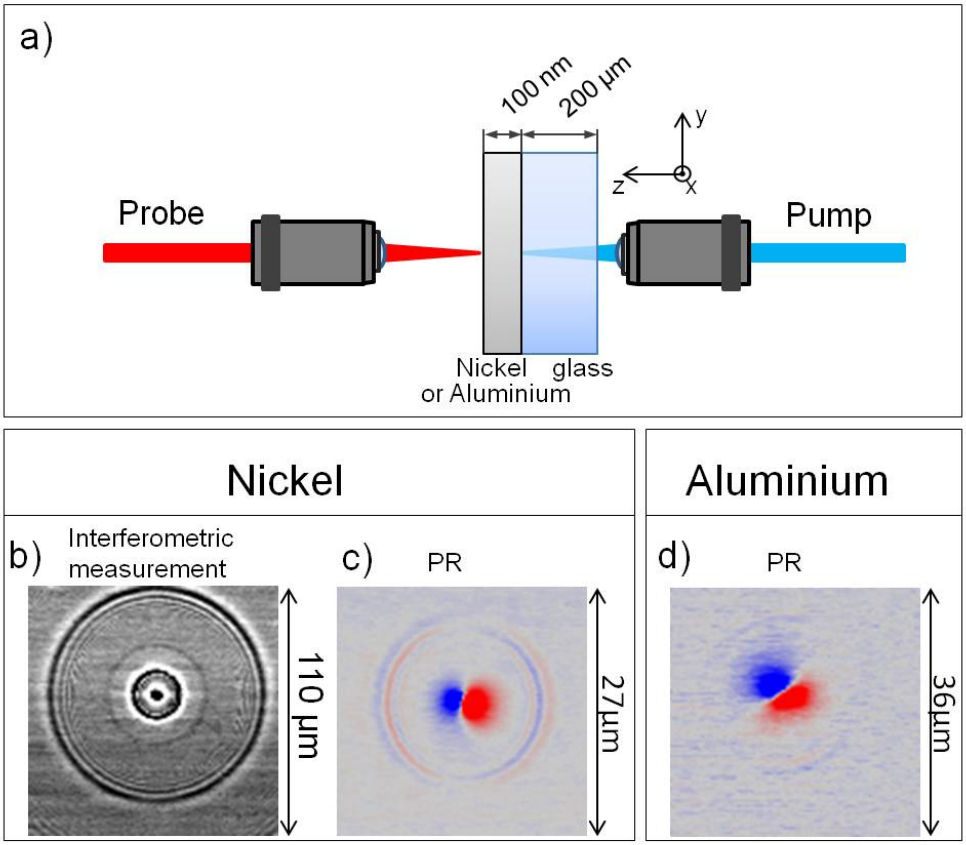

Figure 7.10.: (a) Sample orientation for SAW excitation through the substrate. Interferometry and PR maps of Nickel (b). PR map for Aluminium on the glass substrate (c). Maps were taken for the same probe pulse delay $\Delta\tau_{p-p} = 4.4$ ns.

The results of the interferometric and PR measurements are presented in Fig. 7.10 (b) and (c). They are comparable to those obtained for the FeGa sample. The observed symmetry in PR maps was tested by applying the magnetic field with a strong permanent magnet along various directions and we observed the same behavior. Also, we rotated the orientation of the probe polarization, however it did not influence the symmetry. This rather excludes a purely magnetic origin of the signal. The other possibility of the origin of this dipole like symmetry, can be the deflection of the beam at SAWs as it was proposed in [189]. The probe beam is reflected at a small angle to the normal from the sample surface ridged by the SAWs. If the knife edge is placed in front of the photodetector, some of the k-vectors will be cut and different intensity will be recorded for light deflected form upward and downward slope of the surface displacement. This technique was already successfully applied to detect gigahertz SAWs [190]. However, we are not sure what could play a role of the knife edge in our experimental set-up.

To correlate the signal observed in a ring detected with the interferometry and PR, we performed two dispersion maps. The dispersion curve of SAWs observed inter-

ferometry, showed that the dispersion of SAWs is nearly linear for lower frequencies but the velocity (slope) decreases at higher frequency (Fig. 7.11 (a)). It is caused by a stronger sensitivity of higher frequencies to the Nickel layer, which has a quite different sound velocity than the substrate. Moreover, we can confirm what we already saw with the 1D FFT (Fig. 7.9 (b)) that the frequency peaks around 0.8 GHz. The dispersion curve of the signal observed with PR, showed that the maximum intensity was shifted to around 1.2 GHz. If the PR signal is of magnetic origin, the frequency shift can be understood as the excitation being the most efficient with the higher frequency part of the SAWs.

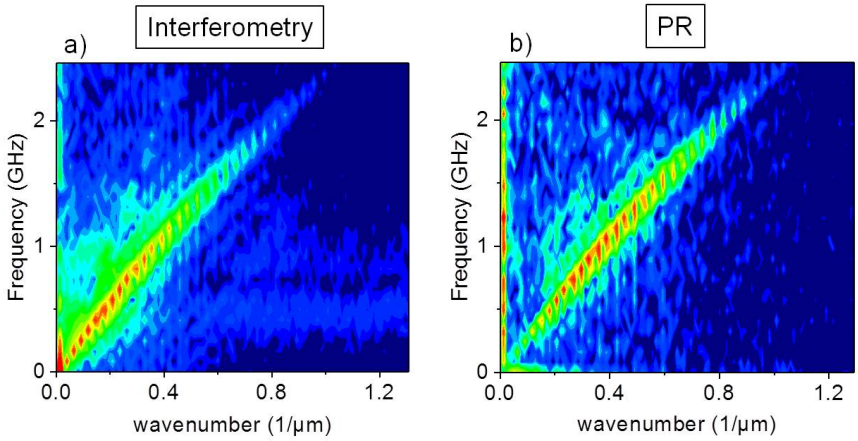

Figure 7.11.: Nickel on glass: Dispersion relations for Interferometry (a) and PMOKE (b) at 0 mT

Figure 7.12 (a) presents the second excitation configuration, where the acoustic waves and magnetic waves are probed through the 200 µm thick glass substrate. The interferometry map now shows some anisotropy (Fig. 7.12 (b)). In the PR map we see a different pattern, closer to four-fold symmetry with a change of phase (Fig. 7.12 (c)). Moreover, it was now easily visible for the Aluminium layer, which gave us a clue that this was not magnetic or not purely magnetic signal (Fig. 7.12 (d)). The symmetry is the same as the one predicted for the PE origin. Similar results were also reported previously in the literature [191].

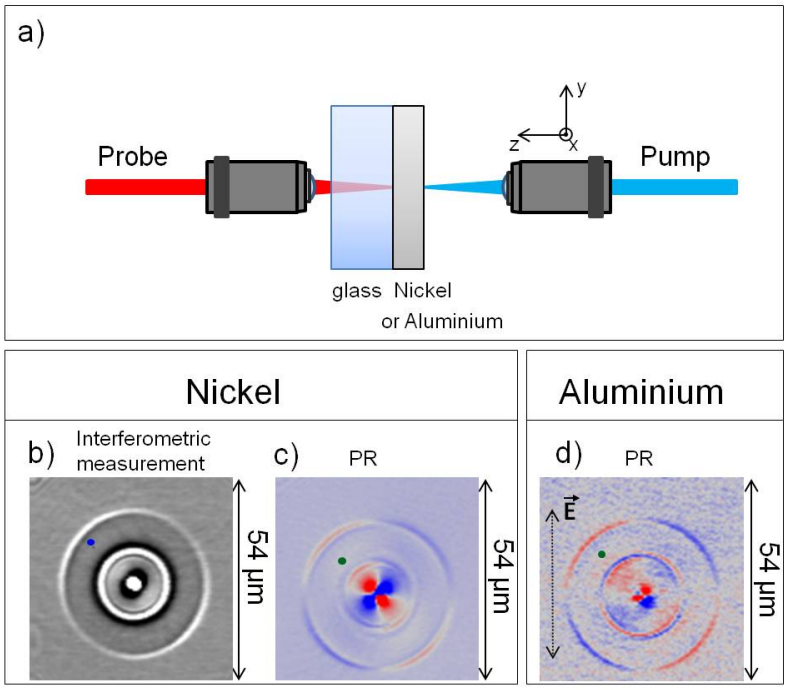

Figure 7.12.: (a) The configuration of the set-up for detection through the transparent substrate. (b) Interferometric and Kerr map for Nickel. The inner ring corresponds to the Rayleigh acoustic waves and outer ring to SSLW. (c) PR picture for Aluminium. The probe pulse delay: $\Delta\tau_{p-p} = 4.4$ ns.

To understand why the PE effect is higher when we probe through the substrate in the Figure 7.13 we plotted the amplitude of the S_{XX} strain component versus the sample depth. The strain is present not only in the Nickel layer but also in the glass substrate.

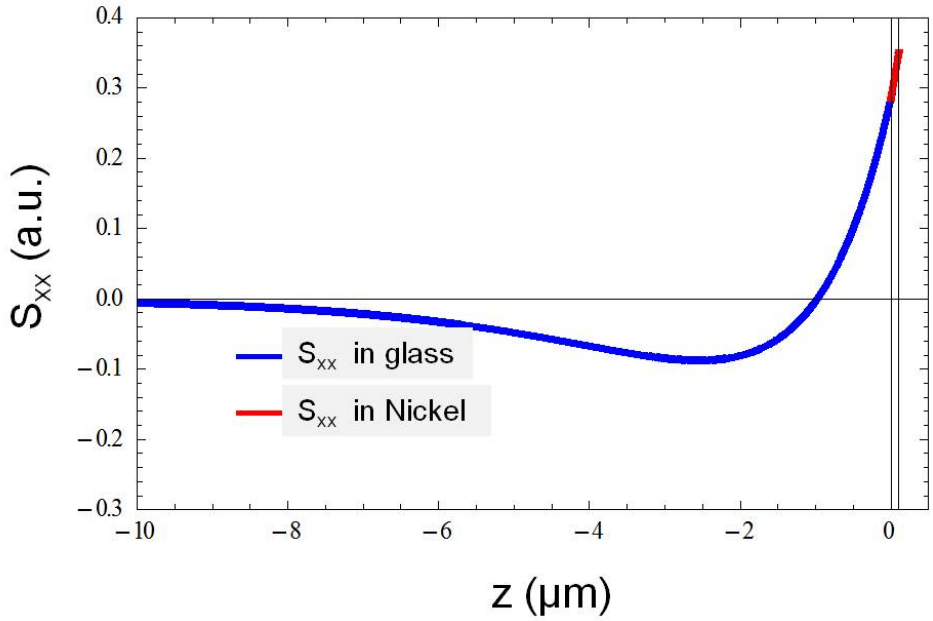

Figure 7.13.: The calculated strain S_{XX} amplitude depth dependence for the case of isotropic Nickel layer on glass (Farnell and Adler's model for Rayleigh waves [61]).

The strain reaches the highest value at the Nickel layer, however the light travels twice through the substrate, whose refraction index is modified and the strain is detected.

The difference between the signal in the ring detected with interferometry and PR, was tested with the time traces and 1D FFT. The results of these measurements for the Nickel sample are presented in Figure 7.14 (a). The two signals are shifted in time but have very similar shape. In the frequency range, the signal measured with PR peaks at 1.15 GHz, 0.35 GHz higher than in the interferometry (7.14 (b)). There is also a very weak second bump at 4.6 GHz.

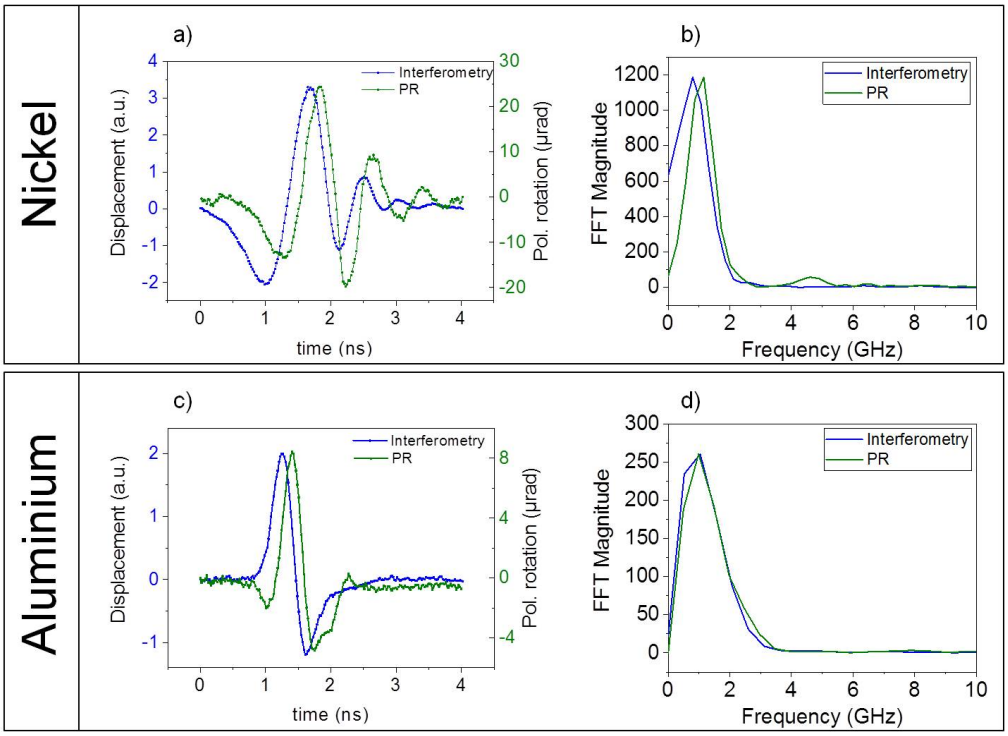

Figure 7.14.: Time profiles of the rings in interferometry and PR measurement probed thorough glass for Nickel (a) and Aluminium (c), together with the FFT of the signals (b) and (d) respectively. Places at which those curves were taken are indicated by the spots in Fig. 7.12 (b) and (c).

On the other hand for the Aluminium sample, the signal was weaker and we saw fewer periods (7.14 (c). However, we can clearly conclude that the signal taken in PR is the derivative of the interferometry signal. This time in the frequency domain we did not observe deviation between the two signals (7.14 (d)).

The difference in frequency content for Nickel for PR and interferometry signals might be the signature of the magnetization precession, especially that it was not observed for the Aluminium sample. However, the symmetry of the PR maps corresponds to PE effect. Therefore, we decided to probe directly on the sample surface, not through the glass for the future campaigns.

7.3.2.1. Sample damage

After the experiments, the sample was inspected with an optical microscope. The images presented in Figure 7.15 shows a grating with a size corresponding to the maps taken with PR and interferometry. The spacing between the fringes agrees as well with the separation distance between the lines in the images.

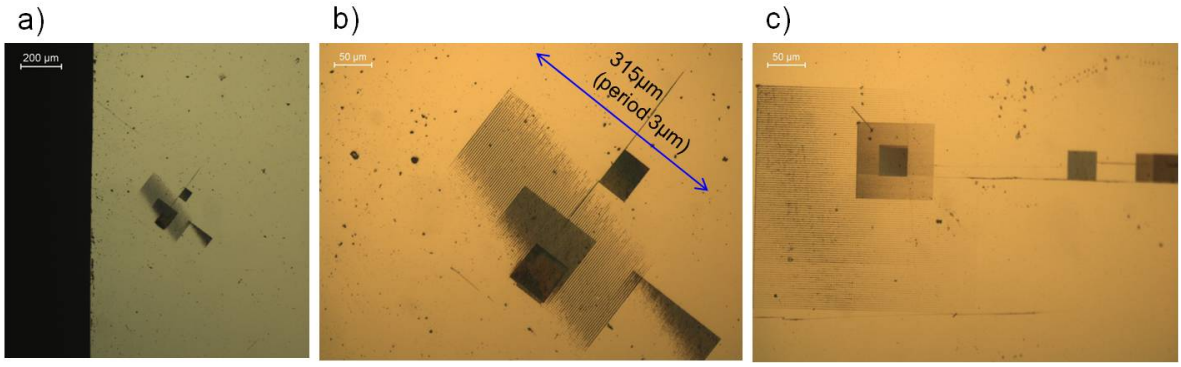

Figure 7.15.: Microscopy images of the Nickel sample taken in reflection for Nickel layer thickness 100 nm (a), (b) and 20 nm (c).

Since the pump objective was mounted on the piezo stage, we concluded that the gratings were formed due to Nickel ablation by the high fluence pump laser (˜3.3 $\frac{mJ}{cm^2}$). Moreover, when the penetration depth ($\delta_{Ni} \cong 15$ nm [192]) is shorter than the sample thickness (100 nm), the efficiency of the ablation can be increased 10 times for laser irradiation of the sample from the substrate side as reported before [193, 194]. Because of the evaporation of the metallic layer at the glass/Nickel interface, the Nickel layer bulges and, when the strain limit is achieved, it lifts-off. These gratings were observed only for 20 nm (Fig. 7.15 (c)) and 100 nm (Fig. 7.15 (a) and (b)) Nickel samples but not for the 300 nm and the Aluminium sample.

The grating produced might have influenced the magnetic properties of the sample: lower the saturation magnetostriction which was already quite low ($\lambda_s \sim 10^{-6}$ [195, 56]). Thus we had to find a substrate with a better heat conductivity.

7.3.3. FeGa under magnetic field

The final attempt for this project was made in summer 2018. As a sample, this time we used a FeGa prepared for us in Spain by Rocio Ranchal at Universidad Complutense de Madrid. Also the following upgrades were made to the experiment:

- A magnetic coil was added to the set-up. To do so, we had to increase the space between the objectives stages (Fig. 7.16 (a)).
- To obtain higher SAW frequencies and to avoid laser ablation, we used Sapphire as a substrate. It was chosen for its high sound velocity (Table 2.1) and good heat conduction. The thermal conductivity for Sapphire at 20°C is 42 $\frac{W}{m \cdot K}$ [196], which is much better than for glass: 1 $\frac{W}{m \cdot K}$ [197].
- The sample was prepared to have high in-plane magnetic anisotropy [172] in order to be able to lower the FMR frequency. For samples with distinguishable hard and easy axes, the magnetic field can lower f_{FMR} when it is applied along the hard axis (Fig. 1.6). The FMR frequencies determined from BBFMR are

plotted in Fig. 7.16 (b). Data for magnetic field below 20 mT could not be reliably obtained.

- On a selected part of the sample, SiO_2 was deposited in order to enhance the PR signal, the thickness of SiO_2 was chosen to provide destructive interference of the $\lambda_{probe} = 800$ nm reflected beam probe [198, 199]. However, the result was unsatisfactory, the contrast of static longitudinal MOKE was enhanced only by 10% and the effect was not visible in PR measurement. Thus we will show mostly data without the SiO_2 layer on the top.

The interferometric map is presented in Fig. 7.16 (c). The ring is slightly anisotropic due to the hexagonal crystallographic structure of Sapphire substrate. Outside of the SAW ring are highly dispersive SSLW waves. They are not as well separated as for the other samples (Fig. 7.6 and 7.10). Similar features were observed with PR (Fig. 7.16 (d)). The symmetry is the same as for the other samples: 2-fold. The difference are oscillations in between the epicenter and the SAW ring. This might be long living magnetization oscillations. However, the PR maps under field do not show significant differences for different field values. In order to check it in a faster way, we performed time traces.

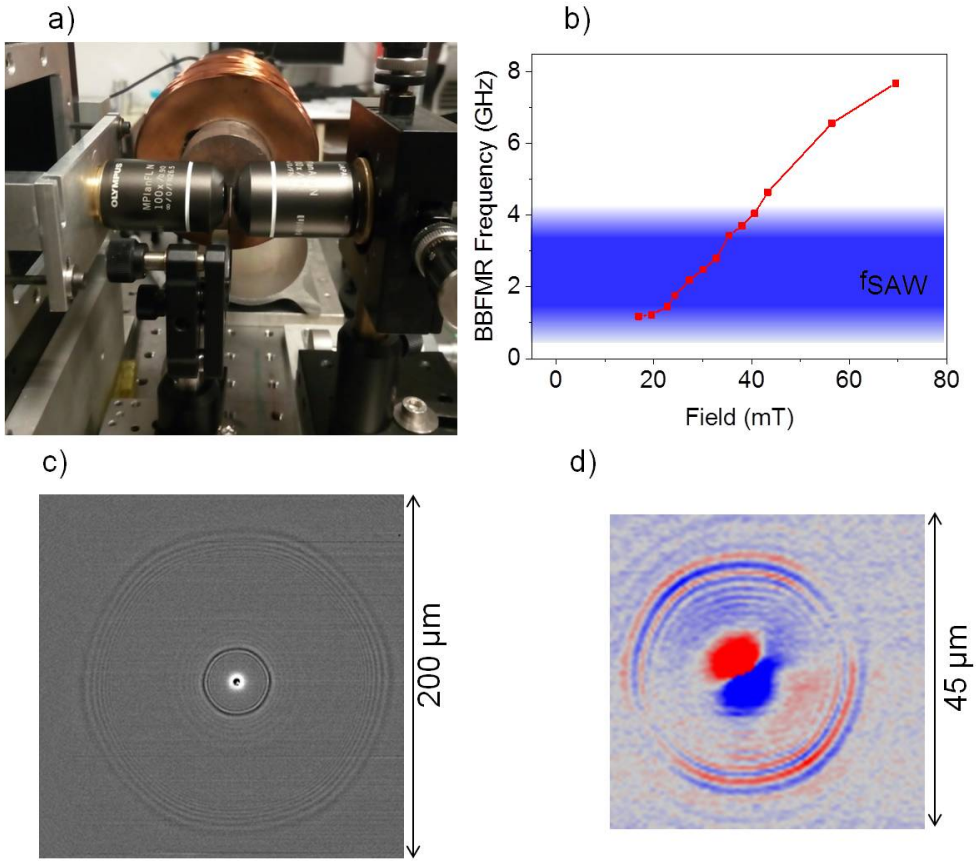

Figure 7.16.: (a) An image of the experimental set-up with pump and probe objectives, the sample located in between the objectives and the magnetic coil behind. (b) Dependence of FMR frequency on the magnetic field obtained in BBFMR. Interferometry (c) and PR (d) maps probing directly on the FeGa side with $\mu_0 H = 0\,mT$. Maps taken for the same delay of a probe laser pulse: $\Delta\tau_{p-p} = 3.1$ ns.

The time profile of generated SAWs is presented in Fig. 7.17 (a). First, with the higher velocity arrives the SSLW (or they might be also a bulk longitudinal wave since it has the same velocity), which we saw also in the interferometry map. The broad frequency content (˜3GHz) of SAWs peaks at 2.4 GHz (Fig. 7.17 (b)). The spectrum covered completely the $f_{FMR}(H)$ curve up to 40 mT (Fig. 7.16 (b)).

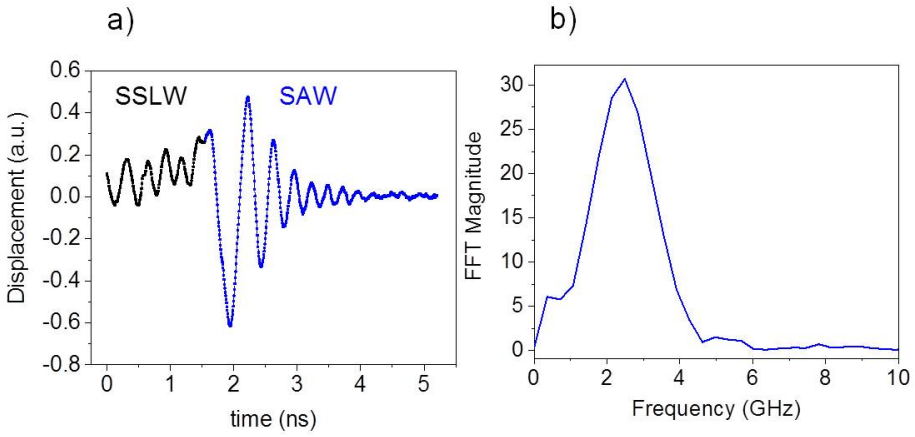

Figure 7.17.: (a) The time profile of SSLW (black part) and SAW (blue) and FFT of the SAW (b). The SAW frequency spectrum is also overlaid on Fig. 7.16 (b) as a blue bar.

To test if these oscillations are due to a magnetic signal we applied the field along the hard axis to tune f_{FMR}. We took a time scan with interferometry and PR measurements for 6 field values. For the signal measured in interferometry we did not expect big changes, however we have noticed that the magnetic field can attract the probe objective and slightly defocus the beam. Nevertheless, this is mostly the case for fields above 40 mT. In Figure 7.18 the time traces for interferometry and PR are plotted together for each field on the same chart. Looking at the PR plot for zero magnetic field (Fig. 7.18 (a)), we can divided the observed signal in four different regions. First, from 0 to 1.5 ns we observed only the signal originated form the SSLW, which was quite similar for interferometry and for PR. The second region is from 1.5 to 2.8 ns. It is clearly dominated by the SAW. The frequency of the oscillations is the same for both measurements. Then, from 2.8 to 4 ns we see that the frequency for PR and interferometry is not the same anymore. The wave has a form of the wave packet, probably due to the interference of different frequencies including the SSLW waves that might have not die out and be still present under the SAWs. The most interesting region for us is after 4 ns, where we do not observe the acoustic waves anymore. Thus, we are more sensitive to the pure magnetic signal. This is also the only place where we observed field dependence. If the signal is quite flat for most of the field values, for $\mu_0 H$= 20 and 25 mT we observed long living oscillations at above 3 GHz which are clearly not as well observed for other field values and interferometry.

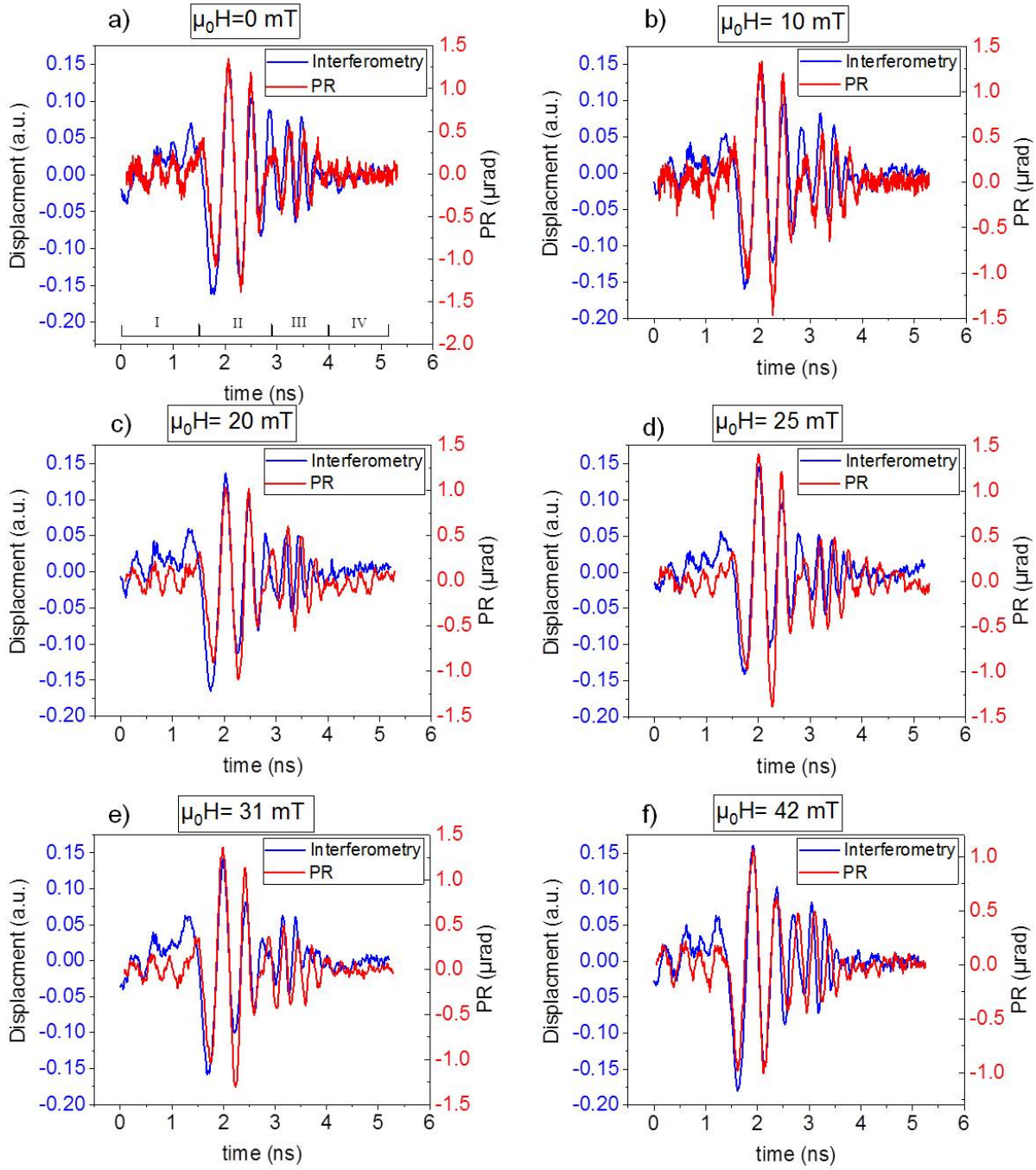

Figure 7.18.: FeGa with SiO_2 on Sapphire: The time traces measured with PR and interferometry for different field values.

By tuning the magnetic field we expected to observe a change of the frequency in the PR signal. We went only up to 42 mT, since for higher field values the focusing is lost and the data becomes difficult to compare. In this field range, we should be still well coupled to different frequencies of the SAWs. However, due to the low

sensitivity of the detected signal on the magnetic field we can certainly confirm the small contribution of the magnetic signal to the PR measurements.

7.3.4. Comparison of dispersion maps for FeGa, Co and Ni

To better resolve the difference between acoustic and magnetic data we recorded dispersion curves for interferometry and PR measurements. Figure 7.19 (a) was taken in the interferometry set-up for FeGa on Sapphire and it showed the dispersion of the two different waves. The line with the higher slope is the dispersion curve of SSLW and one with the lower slope corresponds to the SAW. From the slopes we found the velocities of the two waves: $v_{SSLW} = 10.6\ \frac{km}{s}$ and $v_R = 5.7\ \frac{km}{s}$. The dispersion relation for PR is plotted in Figure 7.19 (b) for 20 mT.

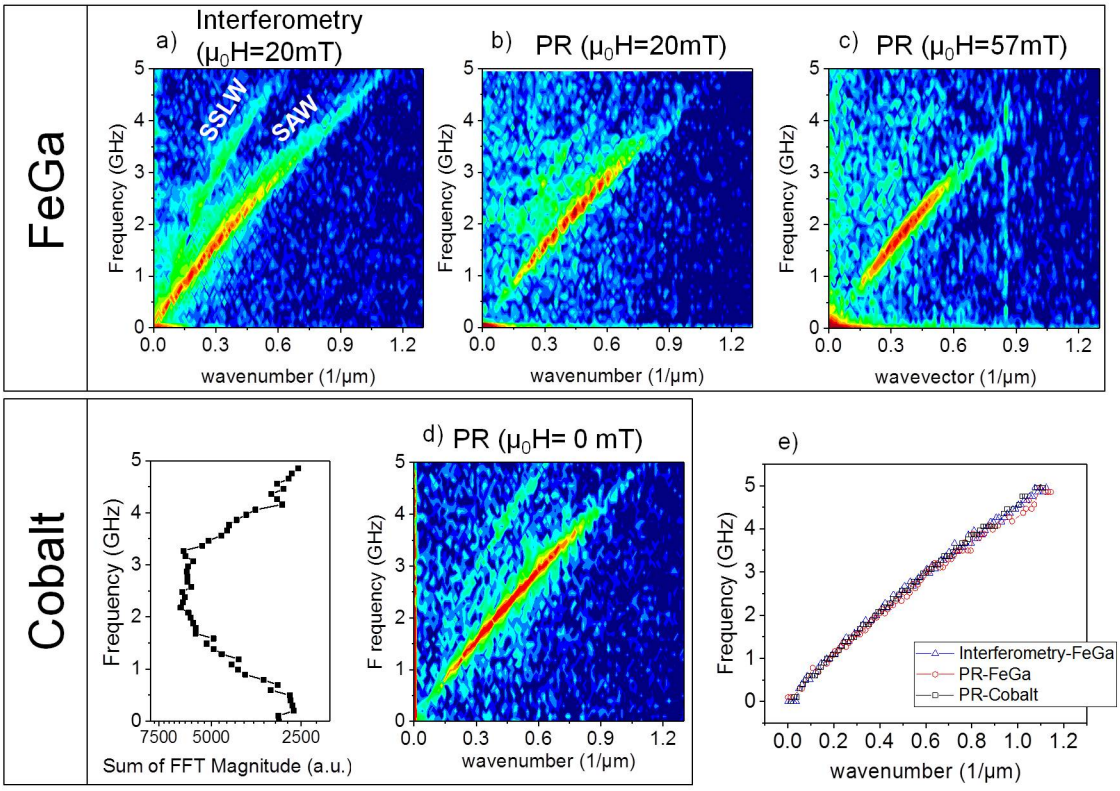

Figure 7.19.: Top panel: Dispersion curves measured with (a) interferometry at 0 mT, (b) PR at 20 mT and (c) PR at 57 mT for FeGa on Sapphire sample. Time for taking the interferometry maps was 40 min, and 3h for the PR. Longer time for PR is caused by lower intensity. The bottom panel shows the dispersion curve measured for Cobalt with PR. On the left the frequency projection is shown which is a sum of the FFT magnitude in each line. (e) is the maximum magnitude extracted from (a), (b) and (c) and plotted on the same graph.

As for intereferometry we observed two curves, but this time the SSLW and SAW curves are not as well separated. Moreover, the highest intensity on the dispersion curve is localized at higher frequencies, which suggested that the frequency content of the signal measured in PR is shifted to higher frequencies. The curve with the lower slope was extracted from dispersion map. It is plotted in Fig. 7.19 (e), together with the dispersion curve measured in intereferometry. The two slopes are identical. This confirms that the signal observed in PR measurement is strongly related to the SAW. Next, to analyze the distribution of intensity in the dispersion curves in interferometry and PR measurements we projected it on the frequency axis, by summing the intensity for each frequency value. This time we can see the difference, the frequency spectrum of the PR dispersion is narrower (Fig. 7.20 (a)). The low frequency part is missing. However, the variation with the magnetic field is rather small, which is presented in Fig. 7.20 (b) where the frequency spectrum taken at 20 mT is overlaid with the one taken at 57 mT. The position of the central peak changes only by 0.2 GHz, while from BBFMR we would expect a much higher shift around 5 GHz. Furthermore, the width of the two spectrum is similar. The small difference is for around 3 GHz where another peak appears for the curve taken at 20 mT. This agrees with the time scans observed for the same field (Fig. 7.18 (c)), where supplementary oscillations are observe at the frequency associated to this bump.

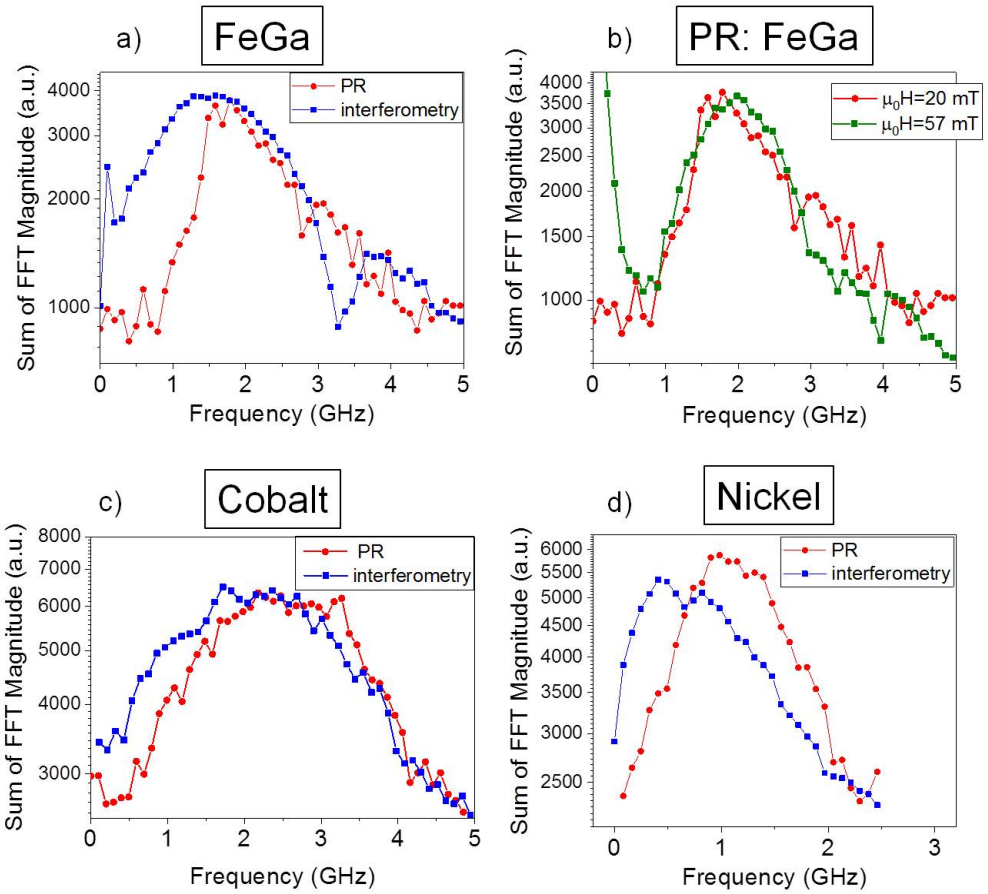

Figure 7.20.: Dispersion relations projected on the frequency axes for: (a) FeGa (interferometry and PR) at 20 mT, (b) FeGa (PR measured at two field values), (c) Cobalt (interferometry and PR) at 0 mT and (d) Nickel (interferometry and PR taken form Fig. 7.11 (a) and (b)) at 0 mT.

To conclude if this effect was due to the magneto-elastic coupling we performed the similar experiment for Cobalt on Sapphire (Section 5.4.2.3) for which results were not shown so far in this thesis. The f_{FMR} for Co is 1 GHz higher than for FeGa, it is above 2 GHz and we expected to observe frequency spectrum of PR centered around higher values. Figure 7.19 (d) shows the dispersion relation measured in PR. The interferometry is not presented because it was very similar to the one obtained for FeGa. The SAW velocity is the same as for FeGa since we used the same substrate (Fig. 7.19 (e)). In figure 7.20 (c) the projection of the frequency content in interferometry and PR measurement is plotted. There is a small frequency shift similar to one observed for the Nickel sample (Fig. 7.20 (d)). Moreover, the PR frequency peaks at 2.4 GHz while for FeGa it was 1.8 GHz, which is consistent with our assumption based on the BBFMR results. However, the frequency of the excited SAWs is also higher.

7.3.5. Confrontation with the non-magnetic sample

We checked a non-magnetic sample, here a 300 nm Titanium on Sapphire, the same substrate as for the previously investigated samples: FeGa and Cobalt. The interferometry map and PR maps looked very similar to what was obtained before (Fig. 7.21 (a) and (b) respectively). The symmetry of the map observed in PR was two fold , with a similar orientation of the symmetry axis. Moreover, the short wavelength fringes are also observed close to the epicenter. To clarify if the differences between interferometry and PR signals detected on FeGa also occur again for this sample, we recorded the time traces (Fig. 7.21 (c)). The frequency of the oscillations detected in the two set-ups was very similar, alike to the other non-magnetic sample, Aluminium on glass (Fig. 7.14 (d)). This is the main indication that the observed higher frequency with PR for magnetic samples originates from magnetization precession.

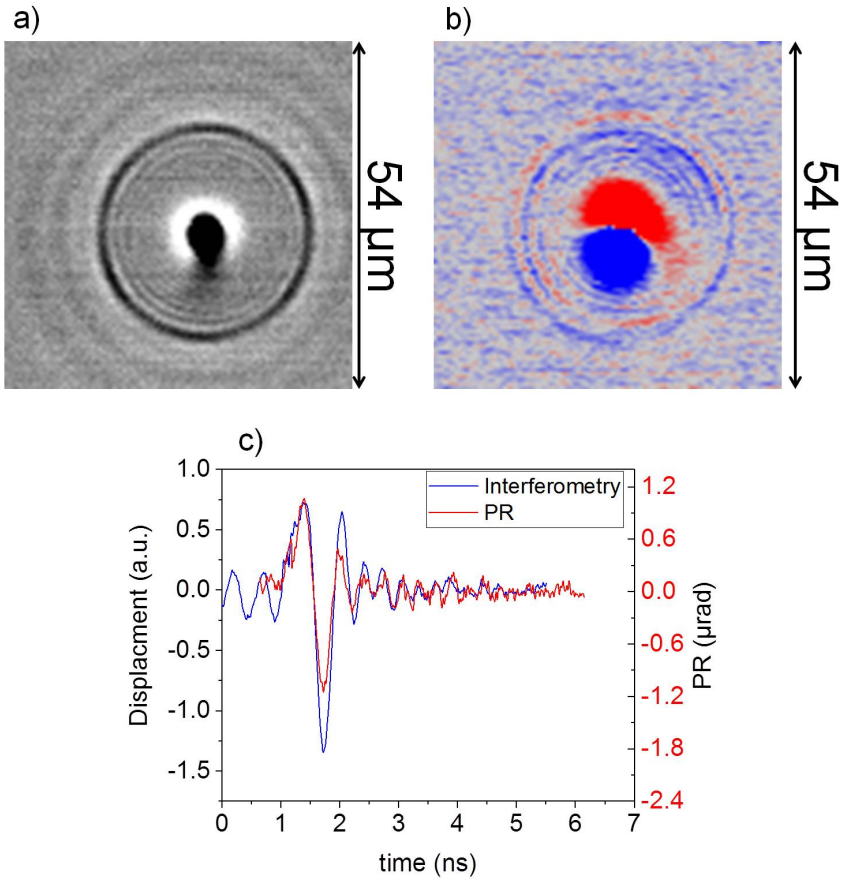

Figure 7.21.: Ti on sapphire: (a) Interferometry and PR map at 0 mT. (c) Time profiles of the oscillations observed in interferometry and PR. Maps taken for the same delay of a probe laser pulse: $\Delta\tau_{p-p} = 3.1$ ns.

Unfortunately, PR signal was too noisy to perform the dispersion relation, which

also would be interesting to see.

7.4. Conclusions and perspectives

In the table below we present the argument pro and cons evidence for magneto-elastic coupling for optically generated SAWs.

Pro	Cons
- higher frequency content in PR signal than interferometry signal for magnetic samples whereas the frequency content of the interferometry and time traces for the non magnetic samples is the same - no dependence on the probe polarization orientation -> not PE effect	- no dependence or non reproducible dependence of the orientation of the two 2-fold symmetry pattern in PR maps on the orientation of the magnetization vector (ruling out S_{rz}) - given the larger amplitude of the S_{rr} component of strain than of the S_{zr} component we would expect to see the 4-fold symmetry in PR maps which we do not see (ruling out S_{rr} torque) - The two fold symmetry observed for non-magnetic samples;

Table 7.1.: Do we observe magneto-elastic coupling?: pro and cons

The difficulty of this project relies on the fact that the SAWs are broadband and highly dispersive, which makes it difficult to distinguish the pure elastic signal from the magnetic signal in PR. This could be solved by defining the $\vec{k}_{SAW}$ and wavelength *e.g.* with the transient grating technique or by patterning the sample. Moreover, we did not observe the strong sign of frequency matching, probably because the expected level of $\delta\Theta$ signal is very small for metals and it was dominated by the non-magnetic signal. For example signal observed for GaMnAs for PR was ten times larger. The contribution of the magnetic signal could be increased by working in Faraday configuration but we could also expected a greater contribution of the PE effect from the substrate. Moreover, we are not totally sure if the samples were magnetostrictive, which could be tested first by depositing IDTs and checking the SAWFMR measurement with our other system, at least for samples with low precession magnetization frequency. IDT could be also use for the optical excitation of the SAWs if irradiated with a pump beam of bigger diameter.

Conclusions and perspectives

In this thesis, we investigated the interaction of surface acoustic waves (SAWs) with magnetization. The surface acoustic waves were excited electrically and optically. In both cases, the magneto-acoustic signal was detected optically.

In the case of SAWs excited electrically with the use of inter digitated transducers (IDTs), it was the first time that the induced magnetization dynamics was detected directly. Before that, the magneto-elastic coupling was detected indirectly as a change of amplitude and phase of the acoustic waves. Here, by locking the phase between SAWs and laser pulses, and by studying the polarization rotation in a GaMnAs sample we detected the in-plane and out-of-plane components of magnetization dynamics and the in-plane strain component through the PE effect. These studies showed that the magnetization precesses at the same frequency as the frequency of the acoustic waves in the case of small SAW amplitude. Moreover, the field studies confirmed that the magnetization amplitude and SAW absorption peak occur at the same field, thus evidencing the resonant magneto-elastic coupling by two independent techniques. The precession efficiency was tested for different SAW excitation powers, temperatures and SAW frequencies (up to 600 MHz). For a high SAW power we observed a nonlinear effect, the precession of magnetization at twice the SAW frequency. By further investigation of the nonlinear effect: only briefly introduced here, we believe that new physics could be discovered, which may be especially useful for signal processing and magnetization switching.

In the second project SAWs were excited optically. This excitation method did not require any contacts at the sample surface, which was very convenient. Furthermore, the experimental set-up was very unique since it offered both TR-Kerr detection and interferometry measurement. A high SAW frequency of around 2.5 GHz for samples on a Sapphire substrate was obtained. However, the SAW frequency spectrum was highly sensitive to the beam focusing, which made the measurements very difficult to reproduce. Moreover, the excited SAWs were highly dispersive due to the Rayleigh velocity mismatch between the ferromagnetic layer and the substrate. This made the magnetic signal very difficult to distinguish from the elastic signal. Many approaches were proposed in this work. The most conclusive one was the comparison of the data obtained for ferromagnetic and nonmagnetic samples. The frequency spectrum of the polarization rotation signal (potentially containing a magnetic contribution) was shifted to higher frequencies with respect to the pure elastic signal for ferromagnetic layers. However, since the excitation of magnetization precession was not very efficient, for future measurements the following solutions should be

considered:

- transmission detection geometry which could increase the contribution of the magnetic signal, since typically the polarization rotation is a few times higher for the Faraday configuration than the Kerr configuration. While in this project, the Kerr effect and the amplitude of the out-of-plane magnetization precession were small comparing to GaMnAs.
- to impose the SAW wavelength with transient grating technique or by patterning the sample. By doing this we could concentrate the SAW power in a single frequency, ensure high reproducibility of the measurements and avoid the issue of SAW dispersion. The alternative solution for the reduction of SAW dispersion could be to find a ferromagnetic metal acoustically matched to a high velocity substrate.

In summary, the two projects showed what a powerful tool for magnetization precession excitation SAWs are. Currently, we were more successful with the electrically excited SAWs because they are more narrow band. However, with the optical method we can reach higher frequencies without lithography patterning. GaMnAs was a good material to start with since the resonant magneto-elastic coupling can be easily obtained and it was already widely studied by our group. We also tested the magneto-elastic coupling with ferromagnetic metals. However, with the chosen optical SAW excitation technique it occurred to be a very demanding task and it will require further work.

As a perspective of the study we would like to mention combining our system with magnonic-phononic crystals, which have been theoretically investigated in the recent years [200]. In these crystals the propagation properties of magnons and phonons can be designed. With the experimental set-ups used in our work, both acoustic and magnetic waves could be imaged in real and reciprocal space which has not yet been demonstrated for magnonic-phononic crystals. For example, we could imagine the realization of a thin 1D periodic structure (for acoustic and magnetic waves) instead of the homogeneous magnetic film. The magnetic-phononic crystals can fold the dispersion curve of magnons and phonons. Thus new crossing points at high frequencies, where the dispersion of the spin waves is not flat, can be obtained. Hence, the generation of propagating magneto-elastic waves at chosen frequency and wave-vector would be possible.

Moreover, with magnonic-phononic crystals we could guide the magnetic and acoustic waves to separate them from each other and possibly recouple them again, which is one of the approaches for the realization of logic gates. Also, the band gap of a magnonic-phononic waveguide could be tuned *e.g.* with the magnetic field or the static strain, which would allow to guide a chosen wavelength of the magneto-elastic waves. Lastly, we would like to mention the usage of the magnonic-phononic crystals as Bragg mirrors for a resonating cavity of a magnon-phonon laser.

A. Expression for the polarization rotation detected with Lock-in

To find the link between the measured electrical signal and the polarization rotation $\delta\beta$, let us consider the laser pulse with the Gaussian profile:

$$I(t) = I_0 \exp(\frac{-t^2}{a^2}) \tag{A.1}$$

where a is the pulse duration. Then the intensity reflected from the sample is expressed by the Dirac delta function: $\delta(t) = \lim_{a\to 0} \frac{1}{\sqrt{\pi}a} \exp(\frac{-t^2}{a^2})$, which can be written as follows:

$$I_R(t) = RI_0\sqrt{\pi}a\delta(t) \tag{A.2}$$

where R is reflection coefficient. The signal was modulated at the pulse selector frequency (f_{ps}= f_L/N=1/τ_{ps}) and it is given as:

$$I_R(t) = RI_0\sqrt{\pi}a\sum_{n=0}^{\infty}\delta(t - n\tau_{ps}) \tag{A.3}$$

The intensities of the two orthogonal components of the polarization projected on the diodes are given as:

$$\begin{cases} I_{Vert} = I_R(t)\sin^2\left(\frac{\pi}{4} + \delta\beta\right) \\ I_{Hor} = I_R(t)\cos^2\left(\frac{\pi}{4} + \delta\beta\right) \end{cases} \tag{A.4}$$

and the difference measured with the bridge:

$$I_{diff}(t) = I_{Vert} - I_{Hor} = I_R(t)\sin 2\delta\beta \tag{A.5}$$

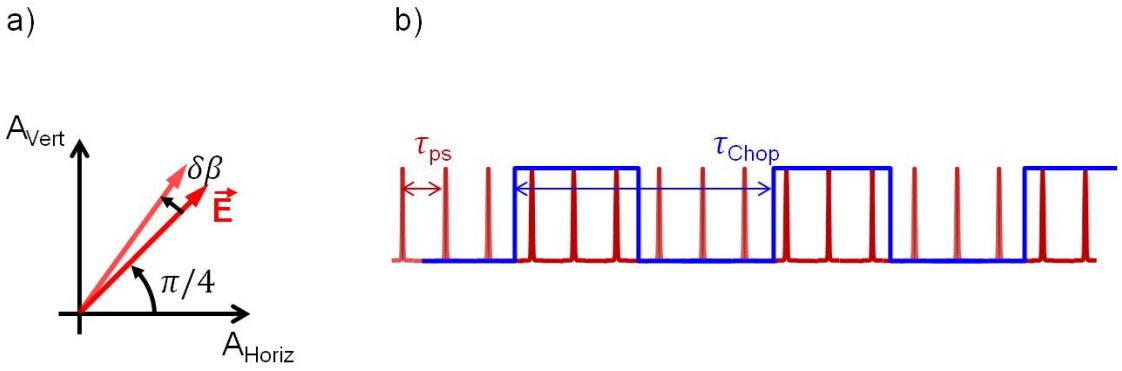

Figure A.1.: (a) Illustration of the polarization rotation and (b) the two modulation frequencies: chopper and pulse picker.

We assume that the polarization rotation angle $\delta\beta$ is small with respect to 1, this will give $\sim 2\delta\beta$ rotation. The bridge's diodes, have their own response described by the function $r(t)$. Hence the signal observed at the output of the diodes is a convolution of the reflected intensity and $r(t)$ function:

$$s = I_R(t) * r(t) \cong 2\int_{-\infty}^{\infty} I_R(u)\delta\beta(u)r\,(t-u)\,\mathrm{du} \tag{A.6}$$

The signal from the bridge was detected with the Lock-in amplifier. A lock-in multiplies the measured signal with the reference signal. As a result, part of the signal containing the reference frequency is filtered as a DC signal with the low pass filters. The *pump* signal, in this case acoustic bursts, needs to be modulated at an additional frequency to provide an effective synchronous detection. In our case the mechanical chopper with blades rotating at 541 Hz was placed just before the slow photodiode (Fig. 6.1). The chopper square modulation signal can be described by the following function:

$$f_{Chop}(t) = \frac{1}{2} + \frac{2}{\pi}\sum_{p=0}^{\infty}\frac{\sin\left[(2p+1)\,\frac{2\pi t}{\tau_{Chop}}\right]}{2p+1} \tag{A.7}$$

In the case of a polarization rotation angle $\delta\beta$ modulated with the function A.7, Equation A.6 can be rewritten as:

$$s_{Chop} = RI_0\sqrt{\pi}a\int_{-\infty}^{\infty}\sum_{n=0}^{\infty}\delta(u-n\tau_{ps})2\delta\beta f_{Chop}(u)r\,(t-u)\,\mathrm{du} \tag{A.8}$$

Therefore, the signal detected by lock-in at the chopper frequency, which additionally converts it to an rms signal is given as follows:

$$s_{Lock-in}^{Chop} = RI_0 2\delta\beta\sqrt{\pi}a\frac{\sqrt{2}}{\tau_{Chop}}$$

$$\times\int_0^{\tau_{Chop}}\sum_{n=0}^{\infty} r\left(t-n\tau_{ps}\right)\left[\frac{1}{2}+\frac{2}{\pi}\sum_{p=0}^{\infty}\frac{\sin\left[(2p+1)\frac{2\pi t}{\tau_{Chop}}\right]}{2p+1}\right]\cos\left(\frac{2\pi}{\tau_{Chop}}t\right)\mathrm{dt} \quad \text{(A.9)}$$

and the signal detected only by one diode at the chopper frequency

$$s_{Lock-in}^{Chop,\,1d}(t) = \frac{R}{2}I_0\sqrt{\pi}a\frac{\sqrt{2}}{\tau_{ps}}\int_0^{\tau_{Chop}}\sum_{n=0}^{\infty} r\left(t-n\tau_{ps}\right)\left[\frac{1}{2}+\frac{2}{\pi}\sum_{p=0}^{\infty}\frac{\sin\left[(2p+1)\frac{2\pi t}{\tau_{Chop}}\right]}{2p+1}\right]\cos\left(\frac{2\pi}{\tau_{Chop}}t\right)\mathrm{dt} \quad \text{(A.10)}$$

We will need it later to find the polarization rotation. In our experimental set-up the chopper was used to modulate SAWs. Therefore we could not use it to normalize the polarization rotation. However, because the chopper was triggered externally by an oscillating function generated by the lock-in, we could still use another modulation reference input to detect the signal at a different frequency. Hence we connected the reference from the pulse generator (f_{ps}), which is the same as reduced laser repetition rate frequency ($f_{ps} = f_L$ /N) .

The signal detected on a one diode at the pulse selector frequency is given as:

$$I_R(t) = RI_0\sqrt{\pi}a\sum_{n=0}^{\infty}\delta(t-n\tau_{ps}) \quad \text{(A.11)}$$

and as before, the signal observed at the output of the diode is a convolution of the reflected intensity and $r(t)$ function:

$$s_{Diode}(t) = \frac{1}{2}I_R(t) * r(t) = \frac{R}{2}I_0\sqrt{\pi}a\sum_{n=0}^{\infty}r(t-n\tau_{ps}) \quad \text{(A.12)}$$

Next, the signal is detected by the lock-in at the pulse selector frequency:

$$s_{Lock-in}^{ps,\,1d}(t) = \frac{R}{2}I_0\sqrt{\pi}a\frac{\sqrt{2}}{\tau_{ps}}\int_0^{\tau_{ps}}\sum_{n=0}^{\infty}r(t-n\tau_{ps})\cos\left(\frac{2\pi}{\tau_{ps}}t\right)\mathrm{dt} \quad \text{(A.13)}$$

To find the polarization rotation, the ratio between the differential signal and the signal measured on one diode at the chopper frequency had to be taken.

$$\frac{s_{Lock-in}^{Chop}}{s_{Lock-in}^{Chop,\,1d}} = \frac{RI_0 2\delta\beta\sqrt{\pi}a}{\frac{R}{2}I_0\sqrt{\pi}a} = 4\delta\beta \tag{A.14}$$

However, because of the reason mentioned above, we used the signal measured at the pulse picker frequency instead of chopper frequency to determine the polarization rotation. Nevertheless, the pulse selector modulation was very different from the chopper modulation (much shorter window) and additional conversion ratio had to be added:

$$\delta\beta = \frac{s_{Lock-in}^{Chop}}{4s_{Lock-in}^{Chop,\,1d}} = \frac{s_{Lock-in}^{Chop}}{4\frac{s_{Lock-in}^{Chop,\,1d}}{s_{Lock-in}^{ps,\,1d}}s_{Lock-in}^{ps,\,1d}} = \frac{s_{Lock-in}^{Chop}}{4\mathbb{R}s_{Lock-in}^{ps,\,1d}} \tag{A.15}$$

where the conversion ratio $\mathbb{R} = \frac{s_{Lock-in}^{ps,\,1d}}{s_{Lock-in}^{Chop,\,1d}}$ was measured with the chopper positioned on the path of the probe beam and it was found to be equal to 1.3 for a bridge gain 10^6.

Bibliography

[1] IBM 350 disk storage unit profile: https://www-03.ibm.com/ibm/history/exhibits/storage/storage_350.html.

[2] RAMAC 350 Restoration Web Site: http://www.ed-thelen.org/RAMAC/.

[3] Stuart Parkin and See Hun Yang. Memory on the racetrack. *Nat. Nanotechnol.*, 10(3):195–198, 2015.

[4] M. Collet, O. Gladii, M. Evelt, V. Bessonov, L. Soumah, P. Bortolotti, S. O. Demokritov, Y. Henry, V. Cros, M. Bailleul, V. E. Demidov, and A. Anane. Spin-wave propagation in ultra-thin YIG based waveguides. *Appl. Phys. Lett.*, 110(9):092408, feb 2017.

[5] A. V. Sadovnikov, C. S. Davies, V. V. Kruglyak, D. V. Romanenko, S. V. Grishin, E. N. Beginin, Y. P. Sharaevskii, and S. A. Nikitov. Spin wave propagation in a uniformly biased curved magnonic waveguide. *Phys. Rev. B*, 96(6):060401, aug 2017.

[6] T. Fischer, M. Kewenig, D. A. Bozhko, A. A. Serga, I. I. Syvorotka, F. Ciubotaru, C. Adelmann, B. Hillebrands, and A. V. Chumak. Experimental prototype of a spin-wave majority gate. *Appl. Phys. Lett.*, 110(15):152401, apr 2017.

[7] Tannous, Charbel and Jacek Gieraltowski. *Magnetic Properties: From Traditional to Spintronic. In: Kasap S., Capper P. (eds) Springer Handbook of Electronic and Photonic Materials. Springer Handbooks.* Number 1. Springer International Publishing, Cham, feb 2017.

[8] A. V. Chumak, V. I. Vasyuchka, A. A. Serga, and B. Hillebrands. Magnon spintronics. *Nat. Phys.*, 11(6):453–461, jun 2015.

[9] György Csaba, Ádám Papp, and Wolfgang Porod. Perspectives of using spin waves for computing and signal processing. *Phys. Lett. Sect. A Gen. At. Solid State Phys.*, 381(17):1471–1476, 2017.

[10] Stephan Breitkreutz-von Gamm, Adam Papp, Eugen Egel, Christian Meier, Cenk Yilmaz, Leonhard Heis, Wolfgang Porod, and Gyorgy Csaba. Design of On-Chip Readout Circuitry for Spin-Wave Devices. *IEEE Magn. Lett.*, 8:3100804, 2017.

[11] Andrii V. Chumak, Alexander A. Serga, and Burkard Hillebrands. Magnon transistor for all-magnon data processing. *Nat. Commun.*, 5(1):4700, dec 2014.

[12] T. Fischer, M. Kewenig, D. A. Bozhko, A. A. Serga, I. I. Syvorotka, F. Ciubotaru, C. Adelmann, B. Hillebrands, and A. V. Chumak. Experimental prototype of a spin-wave majority gate. *Appl. Phys. Lett.*, 110(15):152401, apr 2017.

[13] L. Dreher, M. Weiler, M. Pernpeintner, H. Huebl, R. Gross, M. S. Brandt, and S. T. B. Goennenwein. Surface acoustic wave driven ferromagnetic resonance in nickel thin films: Theory and experiment. *Phys. Rev. B*, 86(13):134415, oct 2012.

[14] L. Thevenard, C. Gourdon, J. Y. Prieur, H. J. von Bardeleben, S. Vincent, L. Becerra, L. Largeau, and J.-Y. Duquesne. Surface-acoustic-wave-driven ferromagnetic resonance in (Ga,Mn)(As,P) epilayers. *Phys. Rev. B*, 90(9):094401, sep 2014.

[15] S. Davis, A. Baruth, and S. Adenwalla. Magnetization dynamics triggered by surface acoustic waves. *Appl. Phys. Lett.*, 97(23), 2010.

[16] L. Thevenard, I. S. Camara, S. Majrab, M. Bernard, P. Rovillain, A. Lemaître, C. Gourdon, and J.-Y. Duquesne. Precessional magnetization switching by a surface acoustic wave. *Phys. Rev. B*, 93(13):134430, apr 2016.

[17] J. Dean, M. T. Bryan, J. D. Cooper, A. Virbule, J. E. Cunningham, and T. J. Hayward. A sound idea: Manipulating domain walls in magnetic nanowires using surface acoustic waves. *Appl. Phys. Lett.*, 107(14):142405, oct 2015.

[18] Westin Edrington, Uday Singh, Maya Abo Dominguez, James Rehwaldt Alexander, Rabindra Nepal, and S. Adenwalla. SAW assisted domain wall motion in Co/Pt multilayers. *Appl. Phys. Lett.*, 112(5):052402, jan 2018.

[19] Kuntal Roy, Supriyo Bandyopadhyay, and Jayasimha Atulasimha. Hybrid spintronics and straintronics: A magnetic technology for ultra low energy computing and signal processing. *Appl. Phys. Lett.*, 99(6):063108, aug 2011.

[20] L. Thevenard, E. Peronne, C. Gourdon, C. Testelin, M. Cubukcu, E. Charron, S. Vincent, A. Lemaître, and B. Perrin. Effect of picosecond strain pulses on thin layers of the ferromagnetic semiconductor (Ga,Mn)(As,P). *Phys. Rev. B*, 82(10):104422, sep 2010.

[21] L. Thevenard, J.-Y. Duquesne, E. Peronne, H. J. von Bardeleben, H. Jaffres, S. Ruttala, J-M. George, A. Lemaître, and C. Gourdon. Irreversible magnetization switching using surface acoustic waves. *Phys. Rev. B*, 87(14):144402, 2013.

[22] E. M. Lifshitz L. D. Landau. On the theory of the dispersion of magnetic permeability in ferromagnetic bodies. *Phys. Zeitsch. der Sow.*, (8):153–169, feb 1935.

[23] E. M. Lifshitz L. D. Landau. *Statistical physics Part 2: Theory of the condensed state (Course of theoretical physics; vol. 9)*. Robert Maxwell, M.C., 1980.

[24] T.L. Gilbert. Classics in Magnetics A Phenomenological Theory of Damping in Ferromagnetic Materials. *IEEE Trans. Magn.*, 40(6):3443–3449, 2004.

[25] P Fulde, M Cardona, and HJ Queisser. *Springer series in solid-state sciences*. 1978.

[26] Stephen Blundell. Magnetism in Condensed Matter. *Oxford master Ser. Condens. matter Phys.*, jan 2001.

[27] Kannan M. Krishnan. Fundamentals and Applications of Magnetic Materials. *Oxford Univ. Press*, 2016.

[28] S. Haghgoo, M. Cubukcu, H. J. von Bardeleben, L. Thevenard, A. Lemaître, and C. Gourdon. Exchange constant and domain wall width in (Ga,Mn)(As,P) films with self-organization of magnetic domains. *Phys. Rev. B*, 82(4):041301, jul 2010.

[29] Mariana Barturen. *Anisotropía magnética y acople magneto-elástico en películas delgadas de Fe1-xGax crecidas epitaxialmente sobre ZnSe/GaAs(001)*. PhD thesis, jun 2014.

[30] Robert C. O'Handley. *Modern Soft Magnetic Materials*, volume 414-415. 2000.

[31] E F Silva, M A Corrêa, R D Della Pace, C C Plá Cid, P R Kern, M. Carara, C. Chesman, O. Alves Santos, R L Rodríguez-Suárez, A. Azevedo, S M Rezende, and F. Bohn. Thickness dependence of the magnetic anisotropy and dynamic magnetic response of ferromagnetic NiFe films. *J. Phys. D. Appl. Phys.*, 50(18):185001, may 2017.

[32] P. Němec, E. Rozkotová, N. TesaÅová, F. Trojánek, E. De Ranieri, K. Olejník, J. Zemen, V. Novák, M. Cukr, P. Malý, and T. Jungwirth. Experimental observation of the optical spin transfer torque. *Nat. Phys.*, 8(5):411–415, 2012.

[33] Michael Farle. Ferromagnetic resonance of ultrathin metallic layers. *Reports Prog. Phys.*, 61:755–826, 1998.

[34] T. Dietl, H. Ohno, and F. Matsukura. Hole-mediated ferromagnetism in tetrahedrally coordinated semiconductors. *Phys. Rev. B - Condens. Matter Mater. Phys.*, 63(19), 2001.

[35] J. Stigloher, M. Decker, H. S. Körner, K. Tanabe, T. Moriyama, T. Taniguchi, H. Hata, M. Madami, G. Gubbiotti, K. Kobayashi, T. Ono, and C. H. Back. Snell's Law for Spin Waves. *Phys. Rev. Lett.*, 117(3):1–5, 2016.

[36] S. Mansfeld, J. Topp, K. Martens, J. N. Toedt, W. Hansen, D. Heitmann, and S. Mendach. Spin wave diffraction and perfect imaging of a grating. *Phys. Rev. Lett.*, 108(4):1–5, 2012.

[37] V. Veerakumar and R. E. Camley. Focusing of spin waves in YIG thin films. *IEEE Trans. Magn.*, 42(10):3318–3320, 2006.

[38] Vladislav E. Demidov, Sergej O. Demokritov, Karsten Rott, Patryk Krzysteczko, and Guenter Reiss. Mode interference and periodic self-focusing of

spin waves in permalloy microstripes. *Phys. Rev. B - Condens. Matter Mater. Phys.*, 77(6):4–9, 2008.

[39] Zhang Zhi-Dong. Spin waves in thin films, superlattices and multilayers. In *Handb. Thin Film.*, chapter Chapter 4, pages 141—-168. Elsevier, 2002.

[40] S O Demokritov, B Hillebrands, and a N Slavin. Brillouin light scattering studies of confined spin waves: linear and nonlinear confinement. *Phys. Rep.*, 348(6):441–489, 2001.

[41] B. Lenk, H. Ulrichs, F. Garbs, and M. Münzenberg. The building blocks of magnonics. *Phys. Rep.*, 507(4-5):107–136, 2011.

[42] K. Yu Guslienko, S. O. Demokritov, B. Hillebrands, and A. N. Slavin. Effective dipolar boundary conditions for dynamic magnetization in thin magnetic stripes. *Phys. Rev. B - Condens. Matter Mater. Phys.*, 66(13):1–4, 2002.

[43] J. Qi, Y. Xu, A. Steigerwald, X. Liu, J. K. Furdyna, I. E. Perakis, and N. H. Tolk. Ultrafast laser-induced coherent spin dynamics in ferromagnetic Ga1-x Mnx As/GaAs structures. *Phys. Rev. B - Condens. Matter Mater. Phys.*, 79(8):1–8, 2009.

[44] Kunihiro Koike, Hironori Asanuma, Satoshi Igarashi, and Shunnsuke Mori. Damping constants of Ni-Fe and Ni-Co alloy thin films. *IEEE Trans. Magn.*, 42(10):2372–2374, 2006.

[45] Christoph Hauser, Tim Richter, Nico Homonnay, Christian Eisenschmidt, Mohammad Qaid, Hakan Deniz, Dietrich Hesse, MacIej Sawicki, Stefan G. Ebbinghaus, and Georg Schmidt. Yttrium Iron Garnet Thin Films with Very Low Damping Obtained by Recrystallization of Amorphous Material. *Sci. Rep.*, 6(February):1–8, 2016.

[46] Kazuto Yamanoi, Satoshi Yakata, Takashi Kimura, and Takashi Manago. Spin Wave Excitation and Propagation Properties in a Permalloy Film. *Jpn. J. Appl. Phys.*, 52(8R):083001, aug 2013.

[47] Sunjae Chung, Anders Eklund, Ezio Iacocca, Seyed Majid Mohseni, Sohrab R. Sani, Lake Bookman, Mark A. Hoefer, Randy K. Dumas, and Johan Åkerman. Magnetic droplet nucleation boundary in orthogonal spin-torque nano-oscillators. *Nat. Commun.*, 7:11209, apr 2016.

[48] S. I. Klselev, J. C. Sankey, I. N. Krivorotov, N. C. Emley, R. J. Schoelkopf, R. A. Buhrman, and D. C. Ralph. Microwave oscillations of a nanomagnet driven by a spin-polarized current. *Nature*, 425(6956):380–383, 2003.

[49] N. Locatelli, V. Cros, and J. Grollier. Spin-torque building blocks. *Nat. Mater.*, 13(1):11–20, 2014.

[50] Adrien F. Vincent, Jerome Larroque, Nicolas Locatelli, Nesrine Ben Romdhane, Olivier Bichler, Christian Gamrat, Wei Sheng Zhao, Jacques-Olivier Klein, Sylvie Galdin-Retailleau, and Damien Querlioz. Spin-Transfer Torque

Magnetic Memory as a Stochastic Memristive Synapse for Neuromorphic Systems. *IEEE Trans. Biomed. Circuits Syst.*, 9(2):166–174, apr 2015.

[51] Daniel Royer and Eugène Dieulesaint. Elastic Waves in Solid I: Free and Guided Propagation, 2000.

[52] S. B.Q. Tran, P. Marmottant, and P. Thibault. Fast acoustic tweezers for the two-dimensional manipulation of individual particles in microfluidic channels. *Appl. Phys. Lett.*, 101(11), 2012.

[53] Alexey M. Lomonosov, Peter V. Grigoriev, and Peter Hess. Sizing of partially closed surface-breaking microcracks with broadband Rayleigh waves. *J. Appl. Phys.*, 105(8), 2009.

[54] Alexander V. Mamishev, Kishore Sundara-Rajan, Fumin Yang, Yanqing Du, and Markus Zahn. Interdigital sensors and transducers. *Proc. IEEE*, 92(5):808–844, 2004.

[55] Y Wang, Z Li, L Qin, M K Chyu, and Q M Wang. Surface acoustic wave flow sensor. *2011 Jt. Conf. IEEE Int. Freq. Control Eur. Freq. Time Forum Proc.*, (c):1–4, 2011.

[56] D Sanders. The correlations between mechanical stress and magnetic anisotropy in ultra thin film. *Reports Prog. Phys.*, 62(5):809–858, 1999.

[57] Zinoviy Nazarchuk, Valentyn Skalskyi, and Oleh Serhiyenko. *Acoustic Emission: Methodology and Application*, volume i. Springer, 2017.

[58] B. A. Auld. Acoustic fields and waves in solids, 1973.

[59] Arthur A. Oliner. *Acoustic surface waves*, volume 24. 1978.

[60] Ludovic Largeau, Ibrahima Camara, Jean Yves Duquesne, Catherine Gourdon, Pauline Rovillain, Laura Thevenard, and Bernard Croset. Laboratory X-ray characterization of a surface acoustic wave on GaAs: The critical role of instrumental convolution. *J. Appl. Crystallogr.*, 49(6):2073–2081, 2016.

[61] G.W. FARNELL and E.L. ADLER. Elastic Wave Propagation in Thin Layers. In *Phys. Acoust. Vol. 9*, pages 35–127. Academic Press, 1972.

[62] J D Aussel, A Lebrun, and J C Baboux. Generating Acoustic-Waves by Laser - Theoretical and Experimental-Study of the Emission Source. *Ultrasonics*, 26(5):245–255, 1988.

[63] Daniel Royer and Eugene Dieulesaint. *Elastic Waves in Solids II. Generation, Acousto-optic Interaction, Application.* Springer-Verlag, 1999.

[64] L. R. F. Rose. Pointâsource representation for laserâgenerated ultrasound. *J. Acoust. Soc. Am.*, 75(3):723–732, 1984.

[65] E. S. Suhubi A. C. Eringen. *Elastodynamics, Volum II, Linear theory.* Academic Press, 1975.

[66] A. M. Aindow, R. J. Dewhurst, and S. B. Palmer. Laser-generation of directional surface acoustic wave pulses in metals. *Opt. Commun.*, 42(2):116–120, 1982.

[67] J. Janušonis, C. L. Chang, P. H.M. Van Loosdrecht, and R. I. Tobey. Frequency tunable surface magneto elastic waves. *Appl. Phys. Lett.*, 106(18), 2015.

[68] D. Royer, E. Dieulesaint, X. Jia, and Y. Shui. Optical generation and detection of surface acoustic waves on a sphere. *Appl. Phys. Lett.*, 52(9):706–708, feb 1988.

[69] Daniel Royer and C Chenu. Experimental and theoretical waveforms of Rayleigh waves generated by a thermoelastic laser line source. *Ultrasonics*, 38(9):891–895, 2000.

[70] M. M. De Lima, F. Alsina, W. Seidel, and P. V. Santos. Focusing of surface-acoustic-wave fields on (100) GaAs surfaces. *J. Appl. Phys.*, 94(12):7848–7855, 2003.

[71] Sarah Benchabane, Roland Salut, Olivier Gaiffe, Valérie Soumann, Mahmoud Addouche, Vincent Laude, and Abdelkrim Khelif. Surface-Wave Coupling to Single Phononic Subwavelength Resonators. *Phys. Rev. Appl.*, 8(3):034016, sep 2017.

[72] Kazushi Yamanaka, Noritaka Nakaso, Dongyoun Sim, and Takeshi Fukiura. Principle and application of ball surface acoustic wave (SAW) sensor. *Acoust. Sci. Technol.*, 30(1):2–6, 2009.

[73] L. Sandlund, M. Fahlander, T. Cedell, A. E. Clark, J. B. Restorff, and M. Wun-Fogle. Magnetostriction, elastic moduli, and coupling factors of composite Terfenol-D. *J. Appl. Phys.*, 75(10):5656–5658, 1994.

[74] N.B. Ekreem, A.G. Olabi, T. Prescott, A. Rafferty, and M.S.J. Hashmi. An overview of magnetostriction, its use and methods to measure these properties. *J. Mater. Process. Technol.*, 191(1-3):96–101, aug 2007.

[75] Soshin Chikazumi. Physics of Ferromagnetism. *Physics (College. Park. Md).*, 1(11):655, 1997.

[76] Charles Kittel. Physical Theory of Ferromagnetic Domains. *Rev. Mod. Phys.*, 21(4), 1949.

[77] F; Wooten M.; Batanouny. *Symmetry and condensed matter physics*. 2008.

[78] Hubert Alex and Rudolf Schäfer. *Magnetic Domains*, volume 40. 1998.

[79] T. L. Linnik, A. V. Scherbakov, D. R. Yakovlev, X. Liu, J. K. Furdyna, and M. Bayer. Theory of magnetization precession induced by a picosecond strain pulse in ferromagnetic semiconductor (Ga,Mn)As. *Phys. Rev. B*, 84(21):214432, dec 2011.

[80] L.D. Landau E.M. Lifshitz. Theory of Elasticity, 1970.

[81] E. W. Lee. Magnetostriction and magnetomechanical effects. *Reports Prog. Phys.*, 18(1):184–229, 1955.

[82] Mingxia Li and Zhihua Feng. Accurate Young's modulus measurement based on Rayleigh wave velocity and empirical Poisson's ratio. *Rev. Sci. Instrum.*, 87(7):075111, jul 2016.

[83] A. K. Ganguly, K. L. Davis, D. C. Webb, and C. Vittoria. Magnetoelastic surface waves in a magnetic film-piezoelectric substrate configuration. *J. Appl. Phys.*, 47(6):2696–2704, 1976.

[84] I. Feng, M. Tachiki, C. Krischer, and M. Levy. Mechanism for the interaction of surface waves with 200âÅ nickel films. *J. Appl. Phys.*, 53(1):177–193, jan 1982.

[85] R. E. Camley. Magnetoelastic waves in a ferromagnetic film on a nonmagnetic substrate. *J. Appl. Phys.*, 50(8):5272, 1979.

[86] R. Q. Scott and D. L. Mills. Propagation of surface magnetoelastic waves on ferromagnetic crystal substrates. *Phys. Rev. B*, 15(7):3545–3557, 1977.

[87] R. M. Bozorth and H. J. Williams. Effect of small stresses on magnetic properties. *Rev. Mod. Phys.*, 17(1):72–80, 1945.

[88] L. W. McKeehan and P. P. Cioffi. Magnetostriction in Permalloy. *Phys. Rev.*, 28(1):146–157, jul 1926.

[89] P. M. Marcus and F. Jona. Strains in epitaxial films: The general case. *Phys. Rev. B*, 51(8):5263–5268, 1995.

[90] H Ohno, A Shen, F Matsukura, A Oiwa, A Endo, S Katsumoto, and Y Iye. (Ga , Mn) As : A new diluted magnetic semiconductor based on GaAs (Ga , Mn) As : A new diluted magnetic semiconductor based on GaAs. *Appl. Phys. Lett.*, 69:363, 1996.

[91] M. Birowska. Influence of the different strains' components on the uniaxial magnetic anisotropy parameters for a (Ga,Mn)As bulk system: A first-principles study. *J. Magn. Magn. Mater.*, 432:396–403, 2017.

[92] J. Wenisch, C. Gould, L. Ebel, J. Storz, K. Pappert, M. J. Schmidt, C. Kumpf, G. Schmidt, K. Brunner, and L. W. Molenkamp. Control of Magnetic Anisotropy in (Ga, Mn)As by Lithography-Induced Strain Relaxation. *Phys. Rev. Lett.*, 99(7):077201, aug 2007.

[93] A. Lemaître, A. Miard, L. Travers, O. Mauguin, L. Largeau, C. Gourdon, V. Jeudy, M. Tran, and J. M. George. Strain control of the magnetic anisotropy in (Ga,Mn) (As,P) ferromagnetic semiconductor layers. *Appl. Phys. Lett.*, 93(2), 2008.

[94] J. Wunderlich, A. C. Irvine, J. Zemen, V. Holý, A. W. Rushforth, E. De Ranieri, U. Rana, K. Výborný, Jairo Sinova, C. T. Foxon, R. P. Campion, D. A. Williams, B. L. Gallagher, and T. Jungwirth. Local control of magnetocrystalline anisotropy in (Ga,Mn)As microdevices: Demonstration in current-induced switching. *Phys. Rev. B - Condens. Matter Mater. Phys.*, 76(5):1–8, 2007.

[95] A. W. Rushforth, E. De Ranieri, J. Zemen, J. Wunderlich, K. W. Edmonds, C. S. King, E. Ahmad, R. P. Campion, C. T. Foxon, B. L. Gallagher, K. Výborný, J. Kučera, and T. Jungwirth. Voltage control of magnetocrystalline anisotropy in ferromagnetic- semiconductor-piezoelectric hybrid structures. *Phys. Rev. B - Condens. Matter Mater. Phys.*, 78(8):1–5, 2008.

[96] E. De Ranieri, A. W. Rushforth, K. Výborný, U. Rana, E. Ahmad, R. P. Campion, C. T. Foxon, B. L. Gallagher, A. C. Irvine, J. Wunderlich, and T. Jungwirth. Lithographically and electrically controlled strain effects on anisotropic magnetoresistance in (Ga,Mn)As. *New J. Phys.*, 10, 2008.

[97] N. A. Pertsev, H. Kohlstedt, and R. Knöchel. Ferromagnetic resonance in epitaxial films: Effects of lattice strains and voltage control via ferroelectric substrate. *Phys. Rev. B - Condens. Matter Mater. Phys.*, 84(1):1–7, 2011.

[98] L. Thevenard, I. S. Camara, J.-Y. Prieur, P. Rovillain, A. Lemaître, C. Gourdon, and J.-Y. Duquesne. Strong reduction of the coercivity by a surface acoustic wave in an out-of-plane magnetized epilayer. *Phys. Rev. B*, 93(14):140405, apr 2016.

[99] Weiyang Li, Benjamin Buford, Albrecht Jander, and Pallavi Dhagat. Magnetic recording with acoustic waves. *Phys. B Condens. Matter*, 448:151–154, 2014.

[100] Vimal Sampath, Noel D'Souza, Dhritiman Bhattacharya, Gary M. Atkinson, Supriyo Bandyopadhyay, and Jayasimha Atulasimha. Acoustic-Wave-Induced Magnetization Switching of Magnetostrictive Nanomagnets from Single-Domain to Nonvolatile Vortex States. *Nano Lett.*, 16(9):5681–5687, 2016.

[101] H. Bömmel and K. Dransfeld. Excitation of hypersonic waves by ferromagnetic resonance. *Phys. Rev. Lett.*, 3(2):83–84, 1959.

[102] P. M. Rowell. Microwave ultrasonics. *Br. J. Appl. Phys.*, 14(2):60–68, 1963.

[103] M. Pomerantz. Excitation of Spin-Wave Resonance by Microwave Phonons. *Phys. Rev. Lett.*, 7(8):312–313, oct 1961.

[104] J. P. Parekh and H. L. Bertoni. Magnetoelastic rayleigh-type surface wave on a tangentially magnetized YIG substrate. *Appl. Phys. Lett.*, 20(9):362–364, 1972.

[105] J. P. Parekh and H. L. Bertoni. Magnetoelastic Rayleigh waves on a YIG substrate magnetized normal to its surface. *J. Appl. Phys.*, 45(4):1860–1868, 1974.

[106] J. P. Parekh and H. L. Bertoni. Magnetoelastic Rayleigh waves propagating along a tangential bias field on a YIG substrate. *J. Appl. Phys.*, 45(1):434–445, 1974.

[107] R.Q. Scott and D.L. Mills. The interaction of Rayleigh waves with ferromagnetic spins; Propagation parallel to the magnetization. *Solid State Commun.*, 18(7):849–852, jan 1976.

[108] R. E. Camley and R. Q. Scott. Surface magnetoelastic waves in the presence of of exchange interactions and pinning of surface spins. *Phys. Rev. B*, 17(11), 1978.

[109] I. Feng, M. Tachiki, C. Krischer, and M. Levy. Mechanism for the interaction of surface waves with 200âÅ nickel films. *J. Appl. Phys.*, 53(1):177–193, jan 1982.

[110] D. Webb, D. Forester, A. Ganguly, and C. Vittoria. Applications of amorphous magnetic-layers in surface-acoustic-wave devices. *IEEE Trans. Magn.*, 15(6):1410–1415, nov 1979.

[111] Charles Krischer, Ian Feng, Jeffrey B. Block, and Moises Levy. Magnetic-field-dependent attenuation of surface waves by nickel thin films. *Appl. Phys. Lett.*, 29(2):76–77, 1976.

[112] Moises Levy and Hajime Yoshida. Giant attenuation of surface acoustic waves by ferromagnetic films. *J. Magn. Magn. Mater.*, 35(1-3):139–145, mar 1983.

[113] Piotr Kuszewski, Ibrahima S. Camara, Nicolas Biarrotte, Loic Becerra, Jürgen von Bardeleben, A. Lemaître, Catherine Gourdon, Jean-Yves Duquesne, and Laura Thevenard. Resonant magneto-acoustic switching: influence of Rayleigh wave frequency and wavevector. (001):1–10, 2018.

[114] P. G. Gowtham, T. Moriyama, D. C. Ralph, and R. A. Buhrman. Traveling surface spin-wave resonance spectroscopy using surface acoustic waves. *J. Appl. Phys.*, 118(23):233910, dec 2015.

[115] V. Polewczyk, K. Dumesnil, D. Lacour, M. Moutaouekkil, H. Mjahed, N. Tiercelin, S. Petit Watelot, H. Mishra, Y. Dusch, S. Hage-Ali, O. Elmazria, F. Montaigne, A. Talbi, O. Bou Matar, and M. Hehn. Unipolar and Bipolar High-Magnetic-Field Sensors Based on Surface Acoustic Wave Resonators. *Phys. Rev. Appl.*, 8(2):024001, aug 2017.

[116] N. I. Polzikova, a. O. Raevskii, and a. S. Goremykina. Calculation of the spectral characteristics of an acoustic resonator containing layered multiferroic structure. *J. Commun. Technol. Electron.*, 58(1):87–94, 2013.

[117] N I Polzikova, I I Pyataikin, S G Alekseev, I M Kotelyanskii, V A Luzanov, and A O Raevskiy. Magnetoelectric bulk acoustic wave resonator for acoustic spin pumping. *2016 IEEE Int. Freq. Control Symp.*, (May):372–373, 2016.

[118] N. I. Polzikova, S. G. Alekseev, I. I. Pyataikin, I. M. Kotelyanskii, V. A. Luzanov, and A. P. Orlov. Acoustic spin pumping in magnetoelectric bulk acoustic wave resonator. *AIP Adv.*, 6(5):056306, may 2016.

[119] C. Thomsen, H. T. Grahn, H. J. Maris, and J. Tauc. Surface generation and detection of phonons by picosecond light pulses. *Phys. Rev. B*, 34(6):4129–4138, 1986.

[120] O B Wright, T Hyoguchi, and K Kawashima. Laser picosecond acoustic in thin films: effect of elastic boundary conditions on pulse generation. *Jpn. J. Appl. Phys.*, 30(1B):L 131 – L 133, 1991.

[121] A. V. Scherbakov, A. S. Salasyuk, A. V. Akimov, X. Liu, M. Bombeck, C. Brüggemann, D. R. Yakovlev, V. F. Sapega, J. K. Furdyna, and M. Bayer. Coherent magnetization precession in ferromagnetic (Ga,Mn)As induced by picosecond acoustic pulses. *Phys. Rev. Lett.*, 105(11):1–4, 2010.

[122] L. Thevenard, E. Peronne, C. Gourdon, C. Testelin, M. Cubukcu, E. Charron, S. Vincent, A. Lemaître, and B. Perrin. Effect of picosecond strain pulses on thin layers of the ferromagnetic semiconductor (Ga,Mn)(As,P). *Phys. Rev. B - Condens. Matter Mater. Phys.*, 82(10):1–6, 2010.

[123] M. Bombeck, A. S. Salasyuk, B. A. Glavin, A. V. Scherbakov, C. Brüggemann, D. R. Yakovlev, V. F. Sapega, X. Liu, J. K. Furdyna, A. V. Akimov, and M. Bayer. Excitation of spin waves in ferromagnetic (Ga,Mn)As layers by picosecond strain pulses. *Phys. Rev. B*, 85(19):195324, may 2012.

[124] M. Bombeck, J. V. Jäger, A. V. Scherbakov, T. Linnik, D. R. Yakovlev, X. Liu, J. K. Furdyna, A. V. Akimov, and M. Bayer. Magnetization precession induced by quasitransverse picosecond strain pulses in (311) ferromagnetic (Ga,Mn)As. *Phys. Rev. B - Condens. Matter Mater. Phys.*, 87(6):1–5, 2013.

[125] Ji Wan Kim, Mircea Vomir, and Jean Yves Bigot. Ultrafast magnetoacoustics in nickel. *Phys. Rev. Lett.*, 109(October), 2012.

[126] J. V. Jäger, A. V. Scherbakov, T. L. Linnik, D. R. Yakovlev, M. Wang, P. Wadley, V. Holy, S. A. Cavill, A. V. Akimov, A. W. Rushforth, and M. Bayer. Picosecond inverse magnetostriction in galfenol thin films. *Appl. Phys. Lett.*, 103(3), 2013.

[127] T. L. Linnik, A. V. Scherbakov, D. R. Yakovlev, X. Liu, J. K. Furdyna, and M. Bayer. Theory of magnetization precession induced by a picosecond strain pulse in ferromagnetic semiconductor (Ga,Mn)As. *Phys. Rev. B - Condens. Matter Mater. Phys.*, 84(21):1–11, 2011.

[128] Oleksandr Kovalenko, Thomas Pezeril, and Vasily V. Temnov. New concept for magnetization switching by ultrafast acoustic pulses. *Phys. Rev. Lett.*, 110(26):1–5, 2013.

[129] Ji Wan Kim and Jean Yves Bigot. Magnetization precession induced by picosecond acoustic pulses in a freestanding film acting as an acoustic cavity. *Phys. Rev. B*, 95(14):1–6, 2017.

[130] T. Parpiiev, M. Servol, M. Lorenc, I. Chaban, R. Lefort, E. Collet, H. Cailleau, P. Ruello, N. Daro, G. Chastanet, and T. Pezeril. Ultrafast non-thermal laser excitation of gigahertz longitudinal and shear acoustic waves in spin-crossover molecular crystals [Fe (PM â AzA) 2 (NCS) 2]. *Appl. Phys. Lett.*, 111(15):151901, oct 2017.

[131] Naoki Ogawa, Wataru Koshibae, Aron Jonathan Beekman, Naoto Nagaosa, Masashi Kubota, Masashi Kawasaki, and Yoshinori Tokura. Photodrive of magnetic bubbles via magnetoelastic waves. *Proc. Natl. Acad. Sci.*, 112(29):8977–8981, 2015.

[132] Ka Shen and Gerrit E.W. Bauer. Laser-Induced Spatiotemporal Dynamics of Magnetic Films. *Phys. Rev. Lett.*, 115(19):1–5, 2015.

[133] Ka Shen and Gerrit E. W. Bauer. Theory of spin and lattice wave dynamics excited by focused laser pulses. 2:1–7, feb 2018.

[134] Yusuke Hashimoto, Davide Bossini, Tom H. Johansen, Eiji Saitoh, Andrei Kirilyuk, and Theo Rasing. Frequency and wavenumber selective excitation of spin waves through coherent energy transfer from elastic waves. *Phys. Rev. B*, 97(140404):1–5, 2018.

[135] Y. Yahagi, B. Harteneck, S. Cabrini, and H. Schmidt. Controlling nanomagnet magnetization dynamics via magnetoelastic coupling. *Phys. Rev. B - Condens. Matter Mater. Phys.*, 90(14):1–5, 2014.

[136] Yong Xin Yan, Edward B. Gamble, and Keith A. Nelson. Impulsive stimulated scattering: General importance in femtosecond laser pulse interactions with matter, and spectroscopic applications. *J. Chem. Phys.*, 83(11):5391–5399, 1985.

[137] Yusuke Hashimoto, Shunsuke Daimon, Ryo Iguchi, Yasuyuki Oikawa, Ka Shen, Koji Sato, Davide Bossini, Yutaka Tabuchi, Takuya Satoh, Burkard Hillebrands, Gerrit E.W. Bauer, Tom H. Johansen, Andrei Kirilyuk, Theo Rasing, and Eiji Saitoh. All-optical observation and reconstruction of spin wave dispersion. *Nat. Commun.*, 8(May):1–6, 2017.

[138] C. L. Chang, A. M. Lomonosov, J. Janusonis, V. S. Vlasov, V. V. Temnov, and R. I. Tobey. Parametric frequency mixing in a magnetoelastically driven linear ferromagnetic-resonance oscillator. *Phys. Rev. B*, 95(6):1–5, 2017.

[139] K. Hillebrands, B., Ounadjela. *Spin Dynamics in Confined Magnetic Structures I*, volume 83 of *Topics in Applied Physics*. Springer Berlin Heidelberg, Berlin, Heidelberg, 2002.

[140] Z. Celinski, K.B. Urquhart, and B. Heinrich. Using ferromagnetic resonance

to measure the magnetic moments of ultrathin films. *J. Magn. Magn. Mater.*, 166(1-2):6–26, 1997.

[141] Cheng P. Wen. Coplanar Waveguide: A Surface Strip Transmission Line Suitable for Nonreciprocal Gyromagnetic Device Applications. *IEEE Trans. Microw. Theory Tech.*, 17(12):1087–1090, 1969.

[142] G. Counil, Joo Von Kim, T. Devolder, C. Chappert, K. Shigeto, and Y. Otani. Spin wave contributions to the high-frequency magnetic response of thin films obtained with inductive methods. *J. Appl. Phys.*, 95(10):5646–5652, 2004.

[143] Sangita S. Kalarickal, Pavol Krivosik, Mingzhong Wu, Carl E. Patton, Michael L. Schneider, Pavel Kabos, T. J. Silva, and John P. Nibarger. Ferromagnetic resonance linewidth in metallic thin films: Comparison of measurement methods. *J. Appl. Phys.*, 99(9), 2006.

[144] F. Giesen. Magnetization Dynamics of Nanostructured Ferromagnetic Rings and Rectangular Elements Dissertation. *PhD thesis, Univ. Hamburg, Fachbereich Phys.*, 2005.

[145] C. Bilzer, T. Devolder, P. Crozat, C. Chappert, S. Cardoso, and P. P. Freitas. Vector network analyzer ferromagnetic resonance of thin films on coplanar waveguides: Comparison of different evaluation methods. *J. Appl. Phys.*, 101(7), 2007.

[146] Simon Foner. Versatile and sensitive vibrating-sample magnetometer. *Rev. Sci. Instrum.*, 30(7):548–557, 1959.

[147] M Faraday. On the magnetization of light and the illumination of magnetic lines of force. *Philos. Trans. R. Soc. London*, 136:1–20, 1846.

[148] E. Hecht. Optics, 2002.

[149] Marvin J. Freiser. A Survey of Magnetooptic Effects. *IEEE Trans. Magn.*, MAG-4(2):152–161, 1968.

[150] Wolfgang Kuch, Rudolf Schäfer, Peter Fischer, and Franz Ulrich Hillebrecht. *Magnetic Microscopy of Layered Structures*, volume 57 of *Springer Series in Surface Sciences*. Springer Berlin Heidelberg, Berlin, Heidelberg, 2015.

[151] J. M. D. Coey. *Magnetism and Magnetic Materials*. Cambridge University Press, Cambridge, 2010.

[152] T. Kuroiwa, T. Yasuda, F. Matsukura, A. Shen, Y. Ohno, Y. Segawa, and H. Ohno. Faraday rotation of ferromagnetic (Ga, Mn)As. *Electron. Lett.*, 34(2):190, 1998.

[153] A K Zvezdin and V A Kotov. *Modern Magnetooptics and Magnetooptical Materials*. IOP Publishing Ltd, 1997.

[154] K.H.J. Buschow, P.G. van Engen, and R. Jongebreur. Magneto-optical properties of metallic ferromagnetic materials. *J. Magn. Magn. Mater.*, 38(1):1–22, aug 1983.

[155] N. TesaÅová, T. Ostatnický, V. Novák, K. Olejník, J. Šubrt, H. Reichlová, C. T. Ellis, A. Mukherjee, J. Lee, G. M. Sipahi, J. Sinova, J. Hamrle, T. Jungwirth, P. Němec, J. Černe, and K. Výborný. Systematic study of magnetic linear dichroism and birefringence in (Ga,Mn)As. *Phys. Rev. B*, 89(8):085203, feb 2014.

[156] P. Němec, E. Rozkotová, N. TesaÅová, F. Trojánek, E. De Ranieri, K. Olejník, J. Zemen, V. Novák, M. Cukr, P. Malý, and T. Jungwirth. Experimental observation of the optical spin transfer torque. *Nat. Phys.*, 8(5):411–415, 2012.

[157] C. C. Robinson. Longitudinal Kerr Magneto-Optic Effect in Thin Films of Iron, Nickel, and Permalloy*. *J. Opt. Soc. Am.*, 53(6):681, jun 1963.

[158] S Demokritov. Brillouin light scattering studies of confined spin waves: linear and nonlinear confinement. *Phys. Rep.*, 348(6):441–489, jul 2001.

[159] Burkard Hillebrands and Jaroslav Hamrle. Investigation of Spin Waves and Spin Dynamics by Optical Techniques. *Handb. Magn. Adv. Magn. Mater.*, (December):1–23, 2007.

[160] H. Schultheiss, C. W. Sandweg, B. Obry, S. Hermsdörfer, S. Schäfer, B. Leven, and B. Hillebrands. Dissipation characteristics of quantized spin waves in nano-scaled magnetic ring structures. *J. Phys. D. Appl. Phys.*, 41(16):164017, aug 2008.

[161] Moonseok Kim, Sebastien Besner, Antoine Ramier, Sheldon J. J. Kwok, Jeesoo An, Giuliano Scarcelli, and Seok Hyun Yun. Shear Brillouin light scattering microscope. *Opt. Express*, 24(1):319, 2016.

[162] Jean-Charles Beugnot, Sylvie Lebrun, Gilles Pauliat, Hervé Maillotte, Vincent Laude, and Thibaut Sylvestre. Brillouin light scattering from surface acoustic waves in a subwavelength-diameter optical fibre. *Nat. Commun.*, 5(1):5242, dec 2014.

[163] Sadao Adachi. *Properties of Semiconductor Alloys*. John Wiley & Sons, Ltd, Chichester, UK, mar 2009.

[164] H. Ohno, A. Shen, F. Matsukura, A. Oiwa, A. Endo, S. Katsumoto, and Y. Iye. (Ga,Mn)As: A new diluted magnetic semiconductor based on GaAs. *Appl. Phys. Lett.*, 69(3):363–365, 1996.

[165] J. Sadowski. GaMnAs: Layers, Wires and Dots. *Acta Phys. Pol. A*, 114(5):1001–1012, nov 2008.

[166] M. Dobrowolska, K. Tivakornsasithorn, X. Liu, J. K. Furdyna, M. Berciu, K. M. Yu, and W. Walukiewicz. Controlling the Curie temperature in (Ga,Mn)As through location of the Fermi level within the impurity band. *Nat. Mater.*, 11(5):444–449, 2012.

[167] L. Chen, S. Yan, P. F. Xu, J. Lu, W. Z. Wang, J. J. Deng, X. Qian, Y. Ji, and J. H. Zhao. Low-temperature magnetotransport behaviors of heavily Mn-

doped (Ga,Mn)As films with high ferromagnetic transition temperature. *Appl. Phys. Lett.*, 95(18):2007–2010, 2009.

[168] Kh. Khazen, H. J. von Bardeleben, J. L. Cantin, A. Mauger, L. Chen, and J. H. Zhao. Intrinsically limited critical temperatures of highly doped Ga1âxMnxAs thin films. *Phys. Rev. B*, 81(23):235201, jun 2010.

[169] A. E. Clark, K. B. Hathaway, M. Wun-Fogle, J. B. Restorff, T. A. Lograsso, V. M. Keppens, G. Petculescu, and R. A. Taylor. Extraordinary magnetoelasticity and lattice softening in bcc Fe-Ga alloys. *J. Appl. Phys.*, 93(10 3):8621–8623, 2003.

[170] N. Menni M. Hemmous, A. Layadi, A. Guittoum, N. Souami, M. Mebarki. Structure, surface morphology and electrical properties of evaporated Ni thin films: Effect of substrates, thickness and Cu underlayer. *Thin Solid Films*, 562:229–238, 2014.

[171] M. Hemmous, A. Layadi, L. Kerkache, N. Tiercelin, V. Preobrazhensky, and P. Pernod. Magnetic Properties of Evaporated Ni Thin Films: Effect of Substrates, Thickness, and Cu Underlayer. *Metall. Mater. Trans. A Phys. Metall. Mater. Sci.*, 46(9):4143–4149, 2015.

[172] A. Muñoz-Noval, S. Fin, E. Salas-Colera, D. Bisero, and R. Ranchal. The role of surface to bulk ratio on the development of magnetic anisotropy in high Ga content Fe 100-x Ga x thin films. *J. Alloys Compd.*, 745:413–420, may 2018.

[173] Rasmus B. Holländer, Cai Müller, Mathis Lohmann, Babak Mozooni, and Jeffrey McCord. Component selection in time-resolved magneto-optical wide-field imaging for the investigation of magnetic microstructures. *J. Magn. Magn. Mater.*, 432:283–290, 2017.

[174] I. S. Camara, B. Croset, L. Largeau, P. Rovillain, L. Thevenard, and J.-Y. Duquesne. Vector network analyzer measurement of the amplitude of an electrically excited surface acoustic wave and validation by X-ray diffraction. *J. Appl. Phys.*, 121(4):044503, jan 2017.

[175] Wolfgang Maichen. *Digital timing measurements: from scopes and probes to timing and jitter*. Springer Science & Business Media, 2006.

[176] SITime. Clock Jitter Definitions and Measurement Methods 1. *Appl Note*, (January):9–10, 2014.

[177] Colin Campbell. *Surface Acoustic Wave Devices and Their Signal Processing Applications*. Academic Press, Inc., 1989.

[178] Florian J.R. Schülein, Eugenio Zallo, Paola Atkinson, Oliver G. Schmidt, Rinaldo Trotta, Armando Rastelli, Achim Wixforth, and Hubert J. Krenner. Fourier synthesis of radiofrequency nanomechanical pulses with different shapes. *Nat. Nanotechnol.*, 10(6):512–516, 2015.

[179] Matthias Weiß, Andreas L. Hörner, Eugenio Zallo, Paola Atkinson, Armando Rastelli, Oliver G. Schmidt, Achim Wixforth, and Hubert J. Krenner. Multiharmonic Frequency-Chirped Transducers for Surface-Acoustic-Wave Optomechanics. *Phys. Rev. Appl.*, 9(1):014004, 2018.

[180] Piotr Kuszewski, Ibrahima S. Camara, Nicolas Biarrotte, Loic Becerra, Jürgen von Bardeleben, W Savero Torres, A. Lemaître, Catherine Gourdon, J-Y Duquesne, and Laura Thevenard. Resonant magneto-acoustic switching: influence of Rayleigh wave frequency and wavevector. *J. Phys. Condens. Matter*, 30(24):244003, 2018.

[181] M. Weiler, L. Dreher, C. Heeg, H. Huebl, R. Gross, M. S. Brandt, and S. T. B. Goennenwein. Elastically Driven Ferromagnetic Resonance in Nickel Thin Films. *Phys. Rev. Lett.*, 106(11):117601, mar 2011.

[182] J. Janušonis, C. L. Chang, P. H. M. van Loosdrecht, and R. I. Tobey. Frequency tunable surface magneto elastic waves. *Appl. Phys. Lett.*, 106(18):181601, may 2015.

[183] A. V. Azovtsev and N. A. Pertsev. Magnetization dynamics and spin pumping induced by standing elastic waves. *Phys. Rev. B*, 94(18):184401, nov 2016.

[184] Zhong-hua Shen, Shu-yi Zhang, and Jian-chun Cheng. Theoretical Study on Surface Acoustic Wave Generated by a Laser Pulse in Solids. In *Anal. Sci. Proc. 11th Int. Conf. Photoacoust. Photothermal Phenom.*, volume 17, pages 204–207, 2001.

[185] J. Janušonis, T. Jansma, C. L. Chang, Q. Liu, A. Gatilova, A. M. Lomonosov, V. Shalagatskyi, T. Pezeril, V. V. Temnov, and R. I. Tobey. Transient Grating Spectroscopy in Magnetic Thin Films: Simultaneous Detection of Elastic and Magnetic Dynamics. *Sci. Rep.*, 6(1):29143, sep 2016.

[186] Y. Hashimoto, A. R. Khorsand, M. Savoini, B. Koene, D. Bossini, A. Tsukamoto, A. Itoh, Y. Ohtsuka, K. Aoshima, A. V. Kimel, A. Kirilyuk, and Th Rasing. Ultrafast time-resolved magneto-optical imaging of all-optical switching in GdFeCo with femtosecond time-resolution and a μm spatial-resolution. *Rev. Sci. Instrum.*, 85(6):063702, jun 2014.

[187] Carolyna Hepburn. *Dynamic Interplay between the Magnetization and Surface Acoustic Waves in Magnetostrictive Fe1-xGax thin films.* PhD thesis, INSP, Sorbonne Université, 2017.

[188] A. Abbas, Y. Guillet, J.-M. Rampnoux, P. Rigail, E. Mottay, B. Audoin, and S. Dilhaire. Picosecond time resolved opto-acoustic imaging with 48 MHz frequency resolution. *Opt. Express*, 22(7):7831, 2014.

[189] Hiroto Yamazaki, Osamu Matsuda, and Oliver B. Wright. Surface phonon imaging through the photoelastic effect. *Phys. Status Solidi C Conf.*, 1(11):2991–2994, 2004.

[190] Julien Higuet, Tony Valier-Brasier, Thomas Dehoux, and Bertrand Audoin. Beam distortion detection and deflectometry measurements of gigahertz surface acoustic waves. *Rev. Sci. Instrum.*, 82(11):114905, nov 2011.

[191] Taiki Saito, Osamu Matsuda, Motonobu Tomoda, and Oliver B. Wright. Imaging gigahertz surface acoustic waves through the photoelastic effect. *J. Opt. Soc. Am. B*, 27(12):2632, 2010.

[192] L. Hadley G. Hass. Optical properties of metals. In D. E. Gray, editor, *Am. Inst. Phys. Handbook,*, chapter 6. McGraw-Hill Book Company, New York, third edition, 1972.

[193] Matthias Domke, Luigi Nobile, Stephan Rapp, Sasia Eiselen, Jürgen Sotrop, Heinz P. Huber, and Michael Schmidt. Understanding thin film laser ablation: The role of the effective penetration depth and the film thickness. *Phys. Procedia*, 56(C):1007–1014, 2014.

[194] Gerhard Heise, Matthias Domke, Jan Konrad, Sebastian Sarrach, Jürgen Sotrop, and Heinz P. Huber. Laser lift-off initiated by direct induced ablation of different metal thin films with ultra-short laser pulses. *J. Phys. D. Appl. Phys.*, 45(31):315303, aug 2012.

[195] E. Klokholm and J. Aboaf. The saturation magnetostriction of thin polycrystalline films of iron, cobalt, and nickel. *J. Appl. Phys.*, 53(3):2661–2663, 1982.

[196] https://global.kyocera.com/prdct/fc/list/material/.

[197] PE Liley RW Powell, CY Ho. *Thermal conductivity of selected materials.* National Standard Reference Data Series - National Bureau of Standards, Washington, D. C, 8 edition, 1966.

[198] N. Qureshi, H. Schmidt, and Aaron Hawkins. Cavity-enhanced Kerr effect for magneto-optic spectroscopy of nanostructures. In *Third IEEE Conf. Nanotechnology. IEEE-NANO 2003.*, volume 2, pages 175–178. IEEE, 2003.

[199] H. Riahi, L. Thevenard, M.A. Maaref, B. Gallas, A. Lemaître, and C. Gourdon. Optimizing magneto-optical effects in the ferromagnetic semiconductor GaMnAs. *J. Magn. Magn. Mater.*, 395:340–344, dec 2015.

[200] Piotr Graczyk, Jarosław Kłos, and Maciej Krawczyk. Broadband magnetoelastic coupling in magnonic-phononic crystals for high-frequency nanoscale spin-wave generation. *Phys. Rev. B*, 95(10):1–6, 2017.